The synthesis and characterisation of Sn(IV) porphyrin derivatives and their potential application in anti-cancer and antimicrobial photodynamic therapy

A thesis submitted in fulfilment of the requirements for the degree of

MASTER OF SCIENCE

IN CHEMISTRY

Rhodes University, South Africa

Department of Chemistry

Faculty of Science

By

Somila Dingiswayo

RHODES UNIVERSITY

Where leaders learn

February 2021

"One glance at a book and you hear the voice of another person, perhaps someone dead for 1,000 years. To read is to voyage through time."

Carl Sagan

"It is good to love many things, for therein lies the true strength, and whosoever loves much performs much, and can accomplish much, and what is done in love is well done."

Vincent Willem van Gogh

Acknowledgements

This work is a product of the guidance and companionship of the S22 research group. With that being said, I am immeasurably grateful to my research advisor Prof Mack - your work ethic is something to admire. Thank you, Prof. I also express my deep gratitude to the leader of the group, Prof Nyokong - the skills you have instilled in us will surely come in handy. It is worth mentioning the significant impact that Dr Britton and Gail Cobus had on this work. Thank you for running a well-oiled machine.

I wish to acknowledge the contribution of Dr Babu, who has moved up the ranks as my mentor, advisor, and most importantly, my friend. Your kindness, compassion and grace are something that everyone should strive for. Rodah and Donovan, I also extend this to you. I wish you guys the best in the future. During my years as a postgraduate student, I have shared a home with great individuals who I now consider my family. To you guys, I offer my appreciation.

I also need to thank my family for their love, support and understanding. To my late mother, the fond memories of your graduation put me on this path. Thank you, Maphiko. Finally, I am deeply thankful to my closest friend Nelly Malapela for her emotional support, love and endless conversations. Above all, I hold your boundless love for God in high regard and may He continue to bless you and your family.

Abstract

In photodynamic therapy (PDT), the activation of light-sensitive drugs in tumour cells produces reactive singlet oxygen species, which cause tumour destruction through a cascade of biochemical reactions. Over the years, the wavelength of activation has been shown to be a critical factor in the penetration of light. Hence the properties of photosensitiser dyes in this context shape their ability to treat deep-seated tumours.

In this study, the synthesis, structural characterisation and photophysicochemical properties of a series of Sn(IV) porphyrins with *meso*-methylthiophenyl rings that have been prepared to study their PDT and photodynamic antimicrobial chemotherapy (PACT) activity properties are reported. The series of Sn(IV) complexes is comprised of a porphyrin (**1-Sn**), a corrole (**2-Sn**), a chlorin (**3-Sn**) and an N-confused porphyrin (**4-Sn**).

Herein, the low symmetry Sn(IV) porphyrin derivatives are shown to have excellent singlet oxygen generation capabilities, and lifetimes of the triplet excited states were in the microsecond range. For example, **4-Sn** had a singlet oxygen quantum yield (Φ_Δ) and an excited triplet state lifetime (τ_T) of 0.88 and 27 μs, respectively. The complexes were studied using UV-visible and magnetic circular dichroism (MCD) spectroscopies. Interestingly, the positive-to-negative sign sequences of the Faraday B_0 terms of **2-Sn** and **3-Sn** reveal that the structural modifications involved break the degeneracy of the MOs derived from the $1e_g^*$ LUMO of the porphyrin **1-Sn**. In contrast, a conventional negative-to-positive sign sequence is observed for **4-Sn**, since the confusion of a pyrrole moiety also results in a large separation of the $1a_{1u}$ and $1a_{2u}$ MOs of the porphyrin **1-Sn** that are derived from the HOMO of a $C_{16}H_{16}^{2-}$

parent hydrocarbon perimeter. The trends in the electronic structures of the Sn(IV) complexes were further investigated through a series of time-dependent density functional theory calculations, so that the suitability of the different types of complex for use in singlet oxygen applications could be further explored.

During *in vitro* photodynamic antimicrobial chemotherapy (PACT) studies, chlorin derivative **3-Sn** had the highest activity towards *S. aureus* and *E. coli* with $\log_{10}$ reductions of 10.5 and 8.74, respectively. The unusually high activity of **3-Sn** against *E. coli* suggests that the interaction of neutral photosensitisers with gram-negative bacteria is more complex than previously understood.

Anti-cancer PDT studies demonstrated that the photosensitisers had negligible dark cytotoxicity. Upon photoirradiation, the Sn(IV) complexes consistently exhibited IC_{50} values lower than 15 μM against MCF-7 adenocarcinoma cells. An IC_{50} value of 1.4 μM for **4-Sn** after activation at the deep-red region of the spectrum demonstrates that complexes of this type merit further in-depth investigation.

The results provide evidence that the low-symmetry Sn(IV) chlorins and N-confused porphyrins merit further in-depth study for use in singlet oxygen applications.

Table of Contents

Acknowledgements iii

Abstract iv

Table of Contents vi

List of Tables x

List of Figures xi

List of Schemes xiv

List of Abbreviations xvi

List of Symbols xvix

1. Introduction 1

1.1 Problem statement 1

1.2 Porphyrins and their derivatives: an outline 1

1.3 Porphyrin nomenclature 4

1.4 Synthesis of porphyrins 5

1.4.1 Rothemund method 5

1.4.2 Adler-Longo method 6

1.4.3 Lindsey's method 7

1.4.4 Transformation of dipyrromethanes into porphyrins 8

1.5 Synthesis of porphyrin synthetic analogues 10

1.5.1 Corroles 10

1.5.2 Chlorins 13

1.5.3 N-confused porphyrin 17

1.6 Electronic properties of porphyrins and their derivatives 21

1.7.1 Fundamental aspects 25

1.7.2 Fluorescence quantum yields and lifetimes 26

1.7.3 Singlet oxygen quantum yields 28

1.7.4 Triplet Lifetimes (τ_T) 29

1.8 Photodynamic therapy (PDT) and antimicrobial PDT (PACT) 30
1.8.1 Porphyrinoid based photosensitisers in PDT 31
1.8.2 Photodynamic antimicrobial chemotherapy (PACT) 33
1.9 Thesis outline 33
Chapter 2 35
Experimental 35
2.1 Materials 36
2.2 Equipment 36
2.3 Synthesis 39
2.3.1 5,10,15,20-*tetrakis*(4-(methylthio)phenyl)porphyrin (**1**) 39
2.3.2 5,10,15,20-*tetrakis*(4-methylthiophenyl)porphyrinato-tin(IV) (**1-Sn**) 40
2.3.3 5,10,15-*tris*(4-methylthiophenyl)corrole (**2**) 39
2.3.4 5,10,15-*tris*(4-methylthiophenyl)corrolato-tin(IV)-chloride (**2-Sn**) 41
2.3.5 5,10,15,20-*tetrakis*(4-methylthiophenyl)chlorin (**3**) 41
2.3.6 Dichloro-[5,10,15,20-*tetrakis*(4-methylthiophenyl)chlorinato-tin(IV)] (**3-Sn**) 42
2.3.7 5,10,15,20-*tetrakis*(4-methylthiophenyl)-2-aza-21-carbaporphyrin (**4**) 42
2.3.8 Dichloro-[5,10,15,20-*tetrakis*(4-methylthiophenyl)-2-aza-21-carbaporphyrinato-tin(IV)] (**4-Sn**) 43
2.4 Photostability experiments 43
2.5 Time-dependent cellular uptake 44
2.6 Cell culture and *in vitro* studies on MCF-7 cancer cells 44
2.6.1 *In vitro* dark toxicity 44
2.6.2 *In vitro* PDT 46
2.7 Bacterial inactivation studies 46
Chapter 3 48
Synthesis and structural characterisation 48
3.1 Syntheses and characterisation of the porphyrinoids 49
3.1.1 Synthesis 49

3.1.2 Characterisation....51
3.2 Summary of the chapter....56
Chapter 4....57
Optical spectroscopy....57
4.1 Groundstate absorption spectroscopy....58
4.2 Fluorescence spectroscopy....60
4.3 Magnetic circular dichroism (MCD)....62
4.4 Summary of chapter....63
Chapter 5....64
Photophysical and photochemical properties....64
5.1 Fluorescence quantum yields and lifetimes....65
5.2 Transient absorption and triplet lifetimes....66
5.3 Photostability and singlet oxygen quantum yields....67
5.4 Summary of Chapter....69
Chapter 6....71
Antimicrobial photodynamic therapy....71
6.1 PACT studies on *S. aureus* and *E. coli*....72
6.2 Summary of chapter....77
Chapter 7....78
Photodynamic therapy....78
7.1 PDT activity of Sn(IV) complexes 1-Sn and 2-Sn against MCF-7 cells....79
7.2 PDT activity of the Sn(IV) complexes 3-Sn and 4-Sn against MCF-7 cells....81
7.3 Summary of chapter....84
Chapter 8....84
Theoretical calculations....84
8.1 Geometry structures and TD-DFT....85
8.2 Summary of the chapter....90
Chapter 9....91

Conclusions and future outlook 91
9.1 Conclusions 92
9.2 Future outlook 94
References 96

List of Tables

Table 1.1 Selected tetrapyrrolic-based photosensitisers approved for clinical use……...31

Table 4.1 The optical absorption and emission data for all the compounds in DMF. 59

Table 5.1 Fluorescence quantum yields and lifetimes of the Sn(IV) complexes and their free base precursors in DMF. 65

Table 5.2 The singlet oxygen quantum yields, triplet lifetimes and photostability of the compounds in DMF. 67

Table 6.1 Log reduction values upon irradiation of *S. aureus* and *E. coli* with a 660 nm LED (280 $mW.cm^{-2}$) for 75 min. Photosensitiser concentrations of 2.5 and 10 μM were used for *S. aureus* and *E. coli*, respectively. 75

Table 7.1 The IC_{50} values of all the photosensitisers studied in this thesis against MCF-7 adenocarcinoma cells. 82

Table 8.1 The TD-DFT spectra of B3LYP/SDD optimised structures of **SnTPP**, **1-Sn**, **2-Sn**, **3-Sn** and **4-Sn** calculated at the CAM-B3LYP/SDD level of theory……89

List of Figures

Figure 1.1 Examples of porphyrins that are ubiquitous in Nature. 2

Figure 1.2 General structures of the porphyrin derivatives and isomers described in this thesis. 3

Figure 1.3 Fischer's numbering system for porphine. 4

Figure 1.4 Numbering scheme for porphine according to the IUPAC recommendations. 5

Figure 1.5 (a) The four frontier molecular orbitals model of porphyrins by Gouterman and the (b) energy level diagram of porphyrinoids and electronic transitions associated with porphyrins and chlorins. 22

Figure 1.6 The typical groundstate absorption spectra of a porphyrin, corrole, chlorin and N-confused porphyrin. 24

Figure 3.1 MALDI-TOF mass spectra of (a) **1** and (2) **1-Sn**. 51

Figure 3.2 ^{1}H NMR spectra of (a) **1** and (b) **1-Sn** 52

Figure 3.3 MALDI-TOF mass spectrum of (a) **2** and (b) **2-Sn**. 53

Figure 3.4 ^{1}H NMR spectra of **2-Sn**. 53

Figure 3.5 MALDI-TOF mass spectrum of (a) **3** and (b) **3-Sn**. 54

Figure 3.6 ^{1}H NMR of (a) **3** and (b) **3-Sn**. 54

Figure 3.7 MALDI-TOF mass spectrum of (a) **4** and (b) **4-Sn**. 55

Figure 3.8 ^{1}H NMR of (a) **4** and (b) **4-Sn.** 55

Figure 4.1 The groundstate absorption (top left) and MCD spectra (bottom left) of (a) **1-Sn** and the groundstate absorption (top right) and MCD spectra (bottom right) of (b) **2-Sn**. 58

Figure 4.2 The groundstate absorption (top left) and MCD spectra (bottom left) of (a) **3-Sn** and the groundstate absorption (top right) and MCD spectra (bottom right) of (b) **4-Sn**. 59

Figure 4.3 The fluorescence emission spectra of (a) **1** and **1-Sn** and (b) **2** and **2-Sn**.61

Figure 4.4 The fluorescence emission spectra of (a) **3** and **3-Sn** and (b) **4** and **4-Sn**.61

Figure 5.1 The fluorescence decay of (blue), reduced X^2 fitting (black), residuals (below, blue) and IRF (red) for **3** in DMF.....65

Figure 5.2 The transient absorption spectrum of **3-Sn** in DMF upon irradiation at Soret band maxima. Inset shows the transient decay curve at the same Soret band maxima.....67

Figure 5.3 The degradation of DPBF in the presence of complex **4-Sn** and photoirradiation at 20 s intervals. 68

Figure 6.1 The effect of Sn(IV) complexes **3-Sn** and **4-Sn** in 1% DMSO/PBS on (a) *S. aureus* and (b) *E. coli* after 75 min of photoirradiation.....73

Figure 6.2 The bacterial viability after treatment of the cells with photosensitiser and being kept in the dark for 60 min. (i) and (iii) represents *S. aureus* after treatment with **4-Sn** and **3-Sn**, respectively. (iii) and (iv) represents *E. coli* cells after treatment with **4-Sn** and **3-Sn,** respectively. 74

Figure 6.3 The effect of **3**, **3-Sn**, **4** and **4-Sn** on the growth of (a) *S. aureus* and (b) *E. coli* where the concentrations of the compounds were 2.5 and 10 μM, respectively.....75

Figure 7.1 The time-dependent cellular uptake of **1-Sn** and **2-Sn** into MCF-7 cells as measured by fluorescence intensity counts using excitation and emission wavelengths of 430 and 630 nm, respectively….....79

Figure 7.2 Cytotoxicity of **1-Sn** and **2-Sn** in MCF-7 cells after 24 h incubation in the dark (black bars), followed by photoirradiation with a Thorlabs 625 nm LED for 30 min (240 $mW.cm^{-2}$) (red and blue bars). (b) Morphological changes observed through phase-contrast microscopy of MCF-7 cells: (i) cells control, (ii) **2-Sn** (10 μM) treated cells in the dark, (iii) **2-Sn** (10 μM) treated cells after photoirradiation with a 625 nm LED for 30 min.....80

Figure 7.3 Cytotoxicity of **3** and **3-Sn** in MCF-7 cells after 24 h incubation in the dark (black bars), followed by photoirradiation with a Thorlabs 660 nm LED for 30 min (280 mW.cm^{-2}) (red bars).....82

Figure 7.4 Cytotoxicity of **4** and **4-Sn** in MCF-7 cells after 24 h incubation in the dark (black bars), followed by photoirradiation with a Thorlabs 660 nm LED for 30 min (280 mW.cm^{-2}) (red bars).....83

Figure 8.1 Groundstate optimised structure of Sn(IV) porphyrin derivatives at the B3LYP/SDD level of theory. 86

Figure 8.2 The TD-DFT groundstate absorption spectra (*in vacuo*) of the compounds at the CAM-B3LYP/SDD level. 87

Figure 8.3 The relative energies of the four frontier molecular orbitals for the Sn(IV) complexes **1-Sn**, **2-Sn**, **3-Sn** and **4-Sn** together with the model tetraphenylporphyrin (TPP) complex with Sn(IV) at the core.....88

List of Schemes

Scheme 1.1. The Rothemund method. 6

Scheme 1.2. The Adler-Longo method. 6

Scheme 1.3. Synthesis of unsymmetrical *meso*-aryl substituted porphyrins *via* mixed aldehyde condensation. 7

Scheme 1.4. Lindsey's one flask, two-step synthesis of porphyrins. 8

Scheme 1.5. The preparation of mesoporphyrin IX dimethyl ester by MacDonald and co-workers. 9

Scheme 1.6. First reported synthesis of a corrole macrocycle by Johnson and Kay. . 10

Scheme 1.7. First direct synthesis of *meso*-substituted corroles by A) Gross *et al.* and B) Paolesse *et al.* in 1999. 11

Scheme 1.8. Reaction scheme for the preparation of *meso*-arylcorroles according to Gryko and Koszarna. 12

Scheme 1.9. Improved one-flask synthesis of *meso*-tetraphenylchlorin reported by Dorough and Huennekens. 13

Scheme 1.10. Preparation of *m*-THPC, the active pharmaceutical ingredient of Foscan®. 15

Scheme 1.11. Microwave-assisted synthesis of a chlorin by Nascimento and co-workers. 16

Scheme 1.12. The first independent accounts of the synthesis of N-confused porphyrins as reported by (a) Latos-Grażyński and co-workers and (b) Furuta and co-workers in 1994. 18

Scheme 1.13. Lindsey's procedure for the improved synthesis of H2NCTPP. 19

Scheme 1.14. Furuta and co-workers' stepwise synthesis of perfluorophenyl bearing N-confused porphyrin (C_6F_5-NCP). 20

Scheme 1.15. Synthesis of doubly N-confused porphyrin (N_2CP) as described by Furuta and co-workers. 21

Scheme 3.1. The synthetic routes for the free base compounds (**1** and **2**) and the corresponding tin(IV) complexes (**1-Sn** and **2-Sn**). 48

Scheme 3.2. Synthesis of the chlorin (**3**) and its tin(IV) complex (**3-Sn**).....49

Scheme 3.3. Synthesis of the N-confused porphyrin (**4**) and its tin(IV) complex (**4-Sn**) 50

List of Abbreviations

^{1}H NMR	Proton nuclear magnetic resonance
API	Active pharmaceutical ingredient
ALA	5-Aminolevulinic acid
AlPc	Aluminium-phthalocyanine chloride
PACT	Photodynamic antimicrobial chemotherapy
BuOH	*n*-Butanol
B3LYP	Becke, 3-parameter, Lee-Yang-Parr
CAM	Coulomb-attenuating method functional
$CDCl_3$	Deuterated chloroform
CSIR	Council for Scientific and Industrial Research
CHPC	Centre for High Performance Computing
CFU	Colony-forming unit
Ce6	Chlorin e6
ΔHOMO	Separation of MOs derived from the HOMO of a parent perimeter
ΔLUMO	Separation of MOs derived from the HOMO of a parent perimeter
DMF	*N*,*N*-Dimethylformamide
DPBF	1,3-Diphenylbenzofuran
DMSO	Dimethyl sulfoxide
DDQ	2,3-Dichloro-5,6-dicyano-1,4-benzoquinone
DMA	9,10-Dimethylanthracene
DMSO-d_6	Deuterated dimethyl sulfoxide
DPBS	Dulbecco's phosphate-buffered saline
DMEM	Dulbecco's modified eagle medium
DCM	Dichloromethane
EU	European Union
FDA	United States Food and Drug Administration
FCS	Fetal calf serum

HOMO	Highest occupied molecular orbital
H_2TPC	Free base Tetraphenylchlorin
H_2NCTPP	Free base N-confused tetraphenylporphyrin
HpD	Hematoporphyrin derivative
IC_{50}	Half maximal inhibitory concentration
IRF	Instrument response function
IUPAC	International Union of Pure and Applied Chemistry
IC	Internal conversion
INI	Institute for Nanotechnology Innovation
ISC	Intersystem crossing
LED	Light-emitting diode
LUMO	Lowest unoccupied molecular orbital
LPS	Lipopolysaccharides
MCF-7	Michigan Cancer Foundation-7
MO	Molecular orbital
MCD	Magnetic circular dichroism
MALDI	Matrix-assisted laser desorption ionisation
MS	Mass spectroscopy
MSA	Methanesulfonic acid
MCP	Microchannel plate
MeOH	Methanol
NCP	N-confused porphyrin
NIR	Near-infrared
OD	Optical density
OPO	Optical parametric oscillator
PDT	Photodynamic therapy
PBS	Phosphate buffered saline
PC6	Proprotein convertase 6

PS	Photosensitiser
PMT	Photomultiplier tube
ROS	Reactive oxygen species
RT	Room temperature
TCSPC	Time-correlated single photon counting
TLC	Thin layer chromatography
TOF	Time of flight
UV-vis	Ultraviolet-visible spectroscopy
VR	Vibrational relaxation
ZnTPP	Zn tetraphenylporphyrin

List of Symbols

*S	Singlet excited state
Abs	Absorbance/absorption
Φ_{Δ}	Singlet oxygen quantum yield
Φ_{F}	Fluorescence quantum yield
S_0	Singlet ground state
t	Time
T_n	Triplet excited state
α	Non-peripheral (or alpha) position
β	Peripheral (or beta) position
ε	Molar extinction coefficient
m/z	Mass-to-charge ratio
λ	Wavelength
τ_F	Fluorescence lifetime
τ_T	Triplet lifetime
e^-	Electron
$Ps^{-\cdot}$	Free radical of photosensitiser

1. Introduction

1.1 Problem statement

Photodynamic therapy (PDT) is a non-invasive type of cancer treatment that utilises a nontoxic drug activated by light of appropriate wavelength to produce reactive oxygen species that elicit a therapeutic response. Today, the widely used photosensitisers are porphyrin-based macrocycles with weak absorption at low energies, the so-called Q bands. As a result, without the aid of interstitial lasers, PDT is mostly used for superficial tumours. This has impeded the wide clinical application of PDT [1,2]. Recent studies have shown that excitation at long wavelengths (e.g. NIR light) can improve the penetration depth and consequently enhance the effect of PDT on deep-seated tumours [3–5].

Herein, a report into the photophysical and PDT properties of porphyrins is given. In the same context, porphyrin isomers and derivatives with lowered symmetries are explored to obtain photosensitisers that absorb in the red to far-red region of the spectrum. The following subsections provide a detailed review of porphyrins followed by their low symmetry counterparts. It also elaborates on the syntheses and application as anti-cancer agents.

1.2 Porphyrins and their derivatives: an outline

Porphyrins and their derivatives are undoubtedly the most studied among the tetrapyrrolic family, with applications ranging from biomedicine to solar cells. They are ubiquitous in Nature, playing a vital role in cellular processes such as oxygen

transport in mammals (heme and Hematoporphyrin) and light-harvesting in photosynthetic plants (chlorophyll).

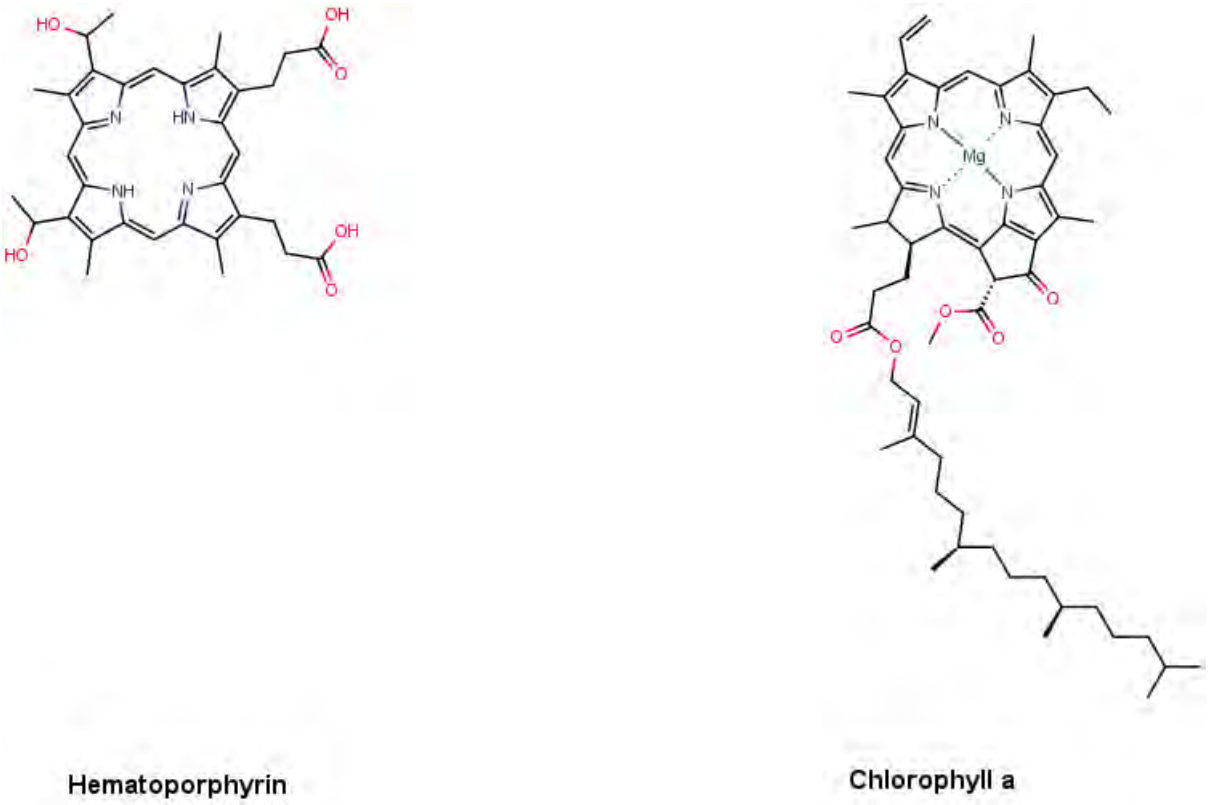

Figure 1.1. Examples of porphyrins that are ubiquitous in Nature.

Owing to their interesting optical properties, which can be modified for different applications through rational structural design, these pigments have been extensively studied for use as catalysts and photosensitisers in biomedical and optoelectronics. Since the description of the fluorescence spectrum of Hematoporphyrin from blood in 1867, significant efforts in porphyrin chemistry have been made. To name a few, ring-contracted porphyrins, hydroporphyrins and structural isomers of porphyrins (**Figure 1.2)** have also found extensive application in diverse fields such as chemical sensing, catalysis and dye-sensitised solar cells [6–15].

Figure 1.2. General structures of the porphyrin derivatives and isomers described in this thesis.

Corroles are tetrapyrrolic macrocycles that, unlike their parent macrocycle (porphyrins), have a direct pyrrole-pyrrole linkage that confers a lower symmetry and a relatively smaller binding cavity. With that being said, the electron-rich π-system is still maintained. This structure is analogous to the corrin ring system found in vitamin B_{12}.

Another class of porphyrin derivative are dihydroporphyrins (or chlorins), with the photosynthetic pigment chlorophyll being the classic example. In comparison to porphyrins, they possess a single reduced peripheral bond, which lowers the symmetry resulting in superior optical properties such as enhanced red region absorption.

Perhaps out of all the tetrapyrrolic macrocycles described in this thesis, N-confused porphyrins can be regarded as true isomers of porphyrins. As can be observed in **Figure 1.2**, N-confused porphyrins only differ in the sense that at least one of the nitrogen atoms in the cavity faces outward, while the CH unit is found in the central cavity of the macrocycle. The coordination chemistry of this ligand has thus been widely studied due to its ability to stabilise metals in unusual oxidation states.

1.3 Porphyrin nomenclature

From a medicinal chemistry standpoint, the advent of porphyrins came with the chemical treatment of haemoglobin with sulfuric acid to obtain iron-free hematin. Subsequently, purification of this compound was achieved by Thudichum in 1867. German physiologist Hoppe-Seyler coined the term "Hematoporphyrin" after describing its spectrum in 1871 [16,17]. The parent form of tetrapyrrolic molecules is a porphine; derivatives of this molecule can have substituents attached to them at various positions. Classically, the nomenclature for porphyrinoids was based on assigning trivial names to new porphyrin entities and a numbering system introduced by Hans Fischer [18,19]. According to this system, the bridging methine carbons (α, β, γ and δ) were assigned as *meso*-positions while the outer pyrrolic carbons were designated as β positions (**Figure 1.3)**.

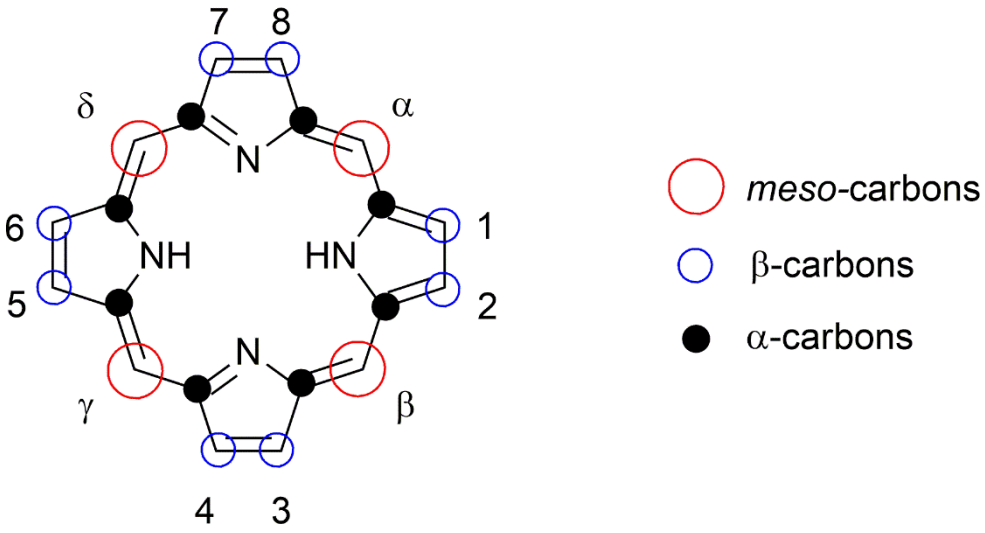

Figure 1.3. Fischer's numbering system for porphine.

In 1979, a systematic IUPAC convention was introduced where every atom in the ring system was numbered (including the inner nitrogen atoms). This approach to naming porphyrins and related macrocycles proved helpful to interdisciplinary communication [20].

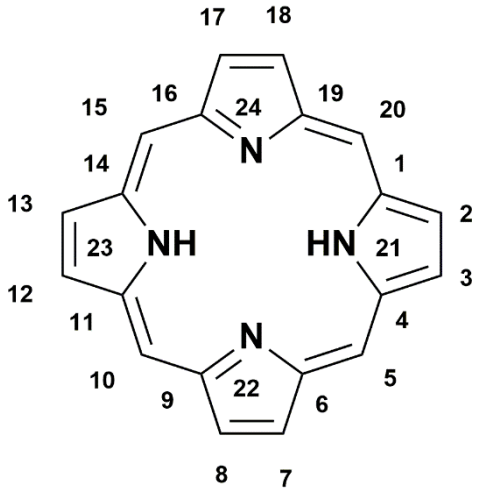

Figure 1.4. The numbering scheme for porphine according to the IUPAC recommendations.

1.4 Synthesis of porphyrins

It is worth noting that Nature provides a vast amount of porphyrinoids that can be used as they are or be chemically treated to yield new porphyrin derivatives. Due to the nature of this dissertation, the focus of this section will be on the major synthetic pathways to porphyrins that exist to date. Additionally, the synthesis of corroles, chlorins and N-confused porphyrins will also be explored.

1.4.1 Rothemund method

In 1935, Paul Rothemund reported the first total synthesis of porphyrins from the condensation of pyrrole and aldehydes in methanol using a sealed reaction tube (90-95 °C) to yield *ca.* 4% of the target product [21]. In 1939, under the same anaerobic conditions (140-150 °C), Rothemund obtained various *meso*-substituted porphyrins, including tetraphenylporphyrin (TPP), in low yields. An improved yield (*ca.* 10%) of TPP was later reported by heating the sealed tubes in the presence of pyridine at 220 °C for 48 h, as illustrated in **Scheme 1.1** [22,23].

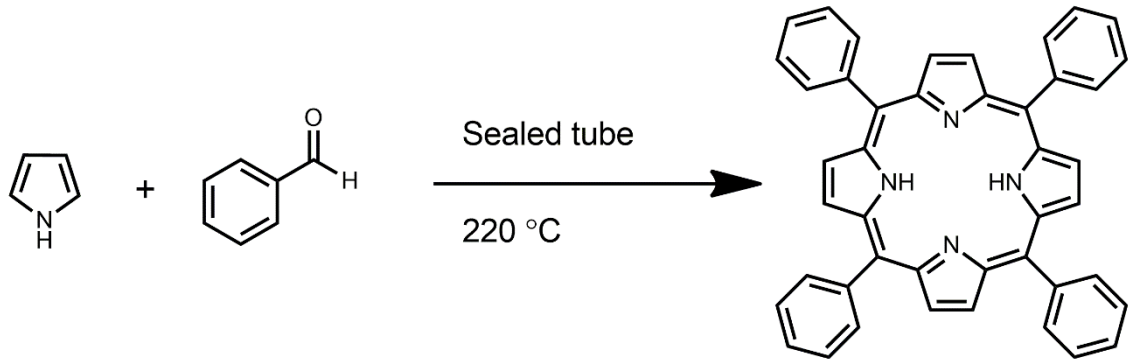

Scheme 1.1. The Rothemund method.

1.4.2 Adler-Longo method

Adler, Longo, and co-workers developed a refined method to synthesise *meso*-substituted symmetrical porphyrins [24]. The method required the refluxing of equimolar amounts of pyrrole and benzaldehyde in propionic acid for 30 min under an open atmosphere. After 30 min, the red-brown solution was allowed to cool to room temperature and then filtered. Washing with methanol followed by hot water affords purple crystals of TPP (**Scheme 1.2**). Under these conditions, moderate yields (20%) meant that large scale preparation of tetraphenylporphyrins was possible. The major limitations of this method are that some aldehydes are sensitive to harsh reaction conditions. Sometimes, precipitation from the propionic acid could prove to be problematic.

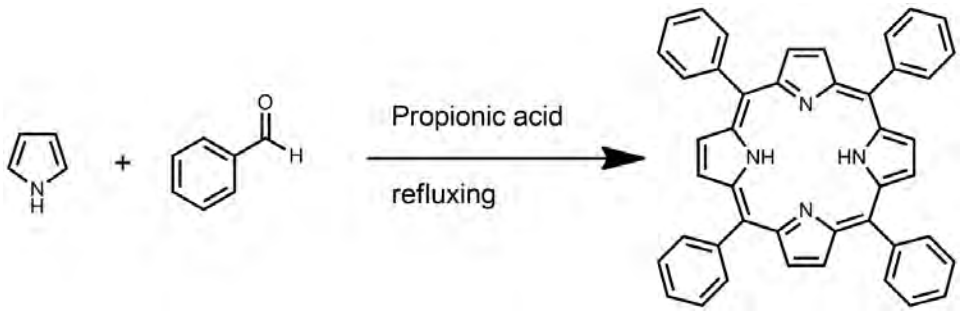

Scheme 1.2. The Adler-Longo method.

The Adler-Longo method was adapted to synthesise unsymmetrical *meso*-aryl-substituted porphyrins *via* mixed aldehyde condensation in fairly good yields [24,25]. The number of different products obtained depends on the proportion of the aldehydes used in the reaction mixture; hence this method is sometimes called statistical condensation. In a typical synthesis of the common A_3B decorated porphyrin (shown in **Scheme 1.3**), a 3:1 proportion of the aldehydes with 4 equiv. of pyrrole is used. Due to the statistical complexity of this route and the nature of the substituents, product isolation requires chromatographic separation, which is sometimes tedious and impractical for large scale applications [26–28].

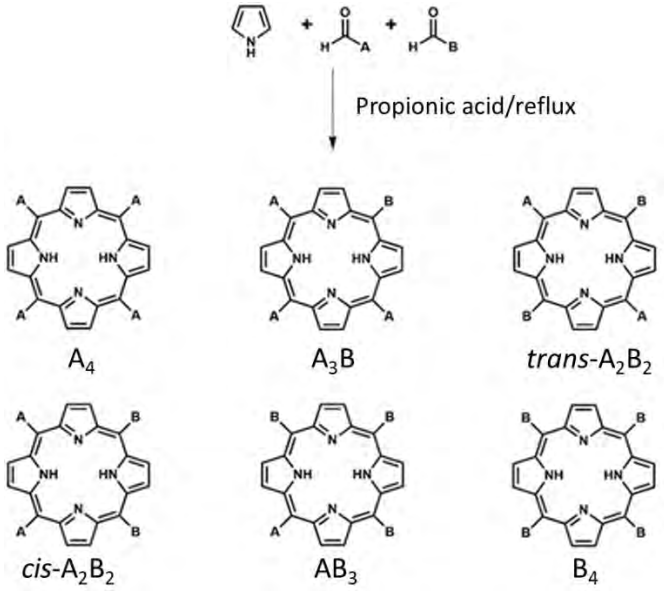

Scheme 1.3. Synthesis of unsymmetrical *meso*-aryl substituted porphyrins *via* mixed aldehyde condensation.

1.4.3 Lindsey's method

With the understanding that biosynthesis of porphyrins proceeds in sequential steps, Jonathan Lindsey and co-workers [29] developed a room temperature two-step, one flask synthesis in the 1980s. The procedure involves a TFA, or $BF_3{\cdot}OEt_2$ catalysed condensation of an aldehyde and pyrrole to form the intermediate molecule, porphyrinogen. As shown in the second step of **Scheme 1.4**, the porphyrinogen is

then subsequently oxidised with quinines (commonly DDQ or *p*-chloranil) to the porphyrin in yields of up to 50% depending on the aldehyde used.

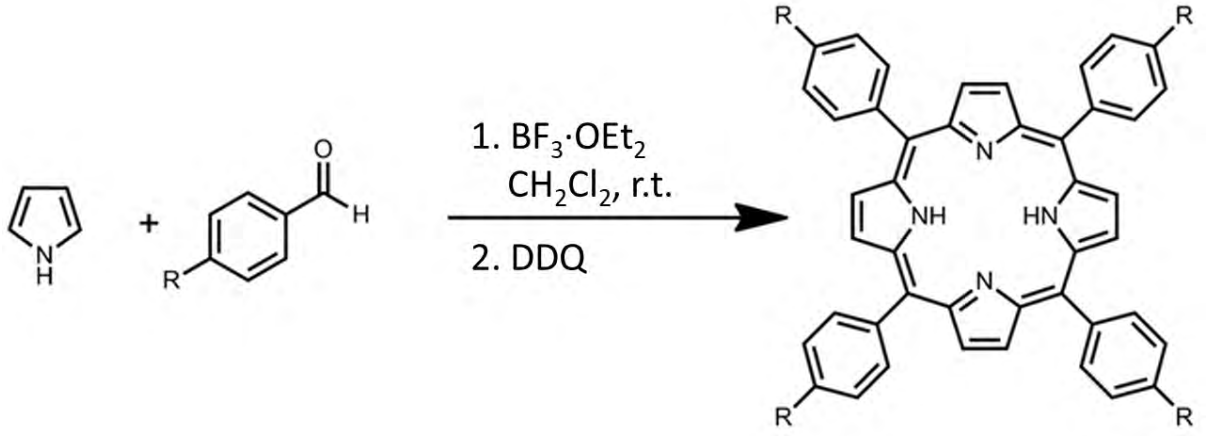

Scheme 1.4. Lindsey's one flask, two-step synthesis of porphyrins.

Lindsey's method is advantageous over Adler-Longo's in the sense that it provides much milder reaction conditions. This is especially important for aldehydes with acid-sensitive groups. In his study, Lindsey demonstrated that his method is sensitive to concentration and hence starting material concentrations of up to 0.01 M are recommended for maximum yield. Another limitation of this method is that copious amounts of chlorinated solvents (typically CH_2Cl_2 or $CHCl_3$) are required. Overall, Lindsey's method has a much broader scope as it can afford many versatile *meso*-arylporphyrins [3,30,31].

1.4.4 Transformation of dipyrromethanes into porphyrins

The linkage of two pyrrole units by a methylene bridge leads to the formation of an important porphyrin intermediate- dipyrromethanes. Although Fischer had already reported on the transformation of dipyrromethane hydrobromides into corresponding porphyrins, the methodology was plagued with many disadvantages

[18,32]. As a result, before MacDonald and co-workers' research, dipyrromethanes (dipyrrylmethanes) were considered to be unstable under acidic conditions such that they could not serve as intermediates for porphyrin synthesis [33–35]. This is due to the rearrangement of the substituents (scrambling) in acidic conditions to form the target compound together with an array of isomeric porphyrin contaminants. Concomitantly, low yields of the compound of interest are obtained.

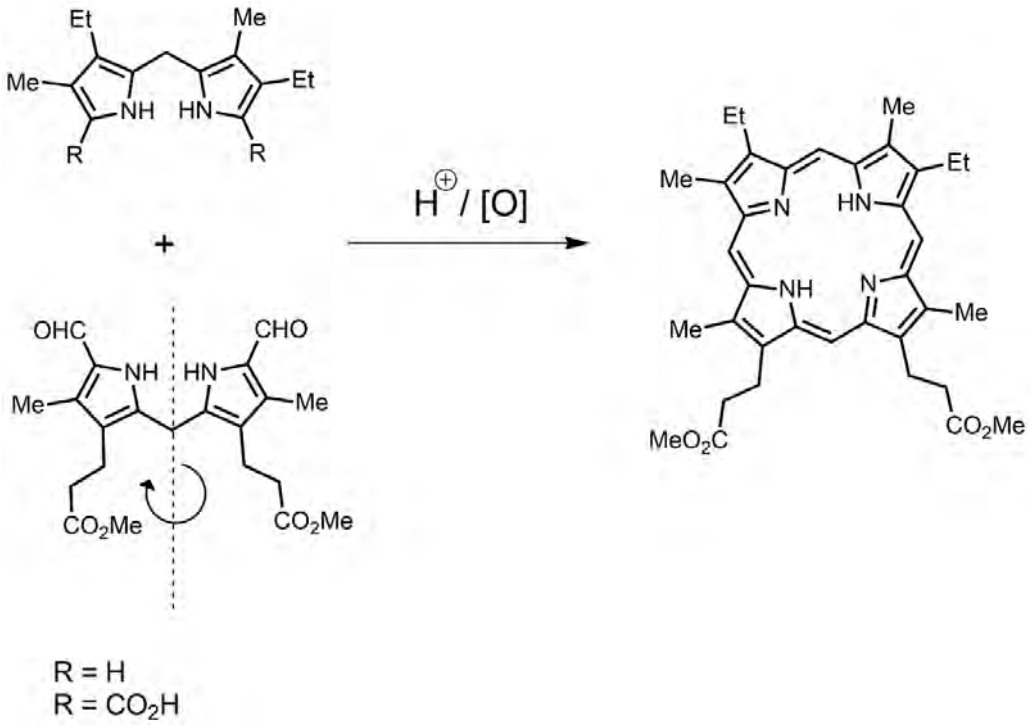

Scheme 1.5. The preparation of mesoporphyrin IX dimethyl ester by MacDonald and co-workers.

To avoid this, MacDonald and co-workers devised a synthetic methodology that resulted in the exclusive formation of uroporphyrin III in high yields [35,36]. This was achieved by ensuring that at least one of the two dipyrromethanes; in this case, 1,9-diformyldipyrromethane is symmetrical about the 5-carbon, as shown in **Scheme 1.5**.

1.5 Synthesis of porphyrin synthetic analogues

1.5.1 Corroles

Corroles were first discovered in the 1960s [37], but the lack of scalable preparative methods largely hindered research in this context. Since the first facile synthesis of triarylcorroles by Gross and co-workers [38], they have garnered the attention of researchers in fields such as photomedicine [39,40] and catalysis [41,42]. From a synthesis standpoint, a lot of progress in the refinement of the reaction conditions for the preparation of *meso*-triarylcorroles has been made. In addition, significant progress in the coordination chemistry of corroles and preparation of sophisticated low symmetry derivatives has also been achieved [43,44].

In the following subsections, a review of the extensive efforts made to improve the synthetic strategies of *meso*-arylcorroles and their corresponding metal complexes is provided.

1.5.1.1 The first synthesis: Johnson and Kay

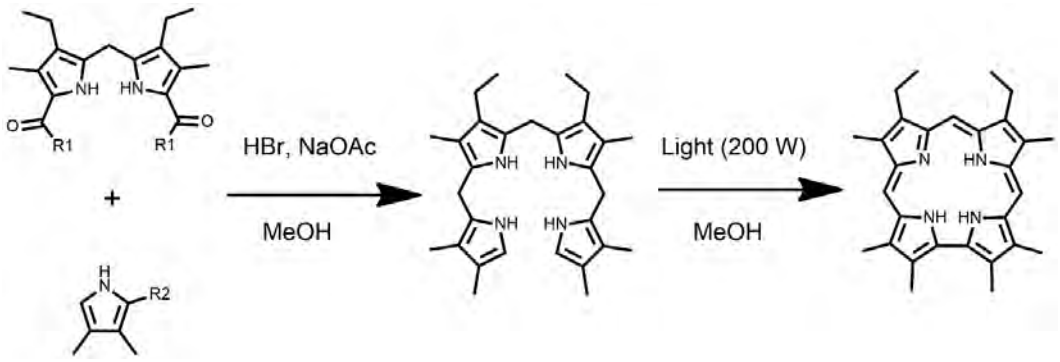

Scheme 1.6. First reported synthesis of a corrole macrocycle by Johnson and Kay.

The first synthesis of corroles was described by Johnson and Kay between 1964 and 1965 [37]. The method involved the suspension of 1,19-dideoxybiladiene-ac

hydrobromides (historically known as 1′,8′-dideoxybiladiene-ac hydrobromides) in methanol. Upon treatment with aqueous sodium acetate, the solution was irradiated with a 200 W bulb, and the cyclisation was complete within 10 min (**Scheme 1.6**).

This synthetic approach was nothing short of ingenuity by the principal researchers. However, with that being said, the method suffered from low yields, and the scope of peripheral substitution patterns was very limited to β-alkylated derivatives [41,42,44].

1.5.1.2 Direct syntheses

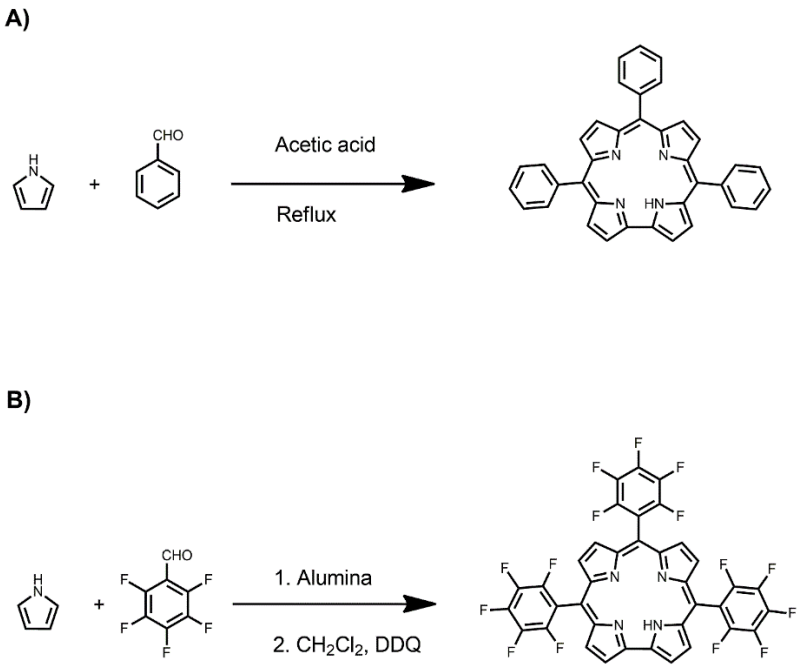

Scheme 1.7. First direct synthesis of *meso*-substituted corroles by A) Gross *et al.* and B) Paolesse *et al.* in 1999.

In 1999, the two independent groups led by Paolesse and Gross reported on the facile synthesis of *meso*-substituted corroles through the condensation of pyrrole and a specific aldehyde [38,45]. Although the yields obtained by Paolesse and Gross were

6 and 11%, respectively, it served as a stepping stone for the optimisation of corrole synthesis.

In the years leading up to 2006, Gryko and Koszarna reported an efficient acid-catalysed synthesis of *meso*-substituted corroles [46–48]. In the acid-mediated formation of corroles, there are essentially two mechanistic steps (**Scheme 1.8**). One is the formation of a mixture of oligomeric condensates of pyrrole and aldehyde, including the precursor to tetrapyrrolic macrocycles-bilane (tetrapyrrane). The second step involves ring closure into a corrole. With regards to the first step, the researchers theorised that to provide a maximal yield of corrole, it is critical that the formation of bilane is maximised while the formation of dipyrromethanes and higher oligomers is kept to a minimum. Hence, this will translate into increased yields of corrole. With inspiration from Kral and co-workers, who mentioned that the addition of methanol enhanced the solubility of the reactants and products [49], Gryko and co-workers found through careful optimisation that a 1:1 mixture of HCl/H_2O kept bilane in solution, while heavy molecular weight condensates precipitate out of solution.

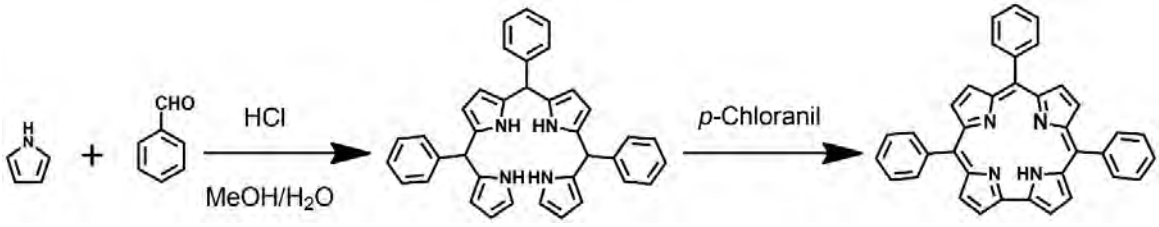

Scheme 1.8. Reaction scheme for the preparation of *meso*-arylcorroles according to Gryko and Koszarna.

To date, the Gryko and Koszarna protocol has remained one of the most efficient procedures for the preparation of symmetrical and asymmetrical corroles decorated with different electron-donating or withdrawing groups.

1.5.2 Chlorins

Chlorins belong to the class of tetrapyrrolic macrocycles and are of great significance in Nature. They share the same carbon-framework with porphyrins. However, the saturation of the β,β′-pyrrolic double bond gives rise to a chlorin (dihydroporphyrins). Further saturation of the distal and proximal β,β′-pyrrolic double bond leads to bacteriochlorin and isobacteriochlorin, respectively. Interestingly, the reduction of these double bonds in dihydroporphyrins and tetrahydrophyrins does not alter the 18π-electron system [50].

Chlorin chemistry is a vast area of research that encompasses studies on the isolation of naturally occurring chlorophylls, the derivatisation of biosynthetic tetrapyrrolic compounds, and the reduction of porphyrins to chlorins and the total synthesis from precursors [50–52]. Therefore, owing to the limited scope of this dissertation, only synthetic and semi-synthetic research will be explored.

1.5.2.1 One Flask Syntheses from Porphyrin reactions

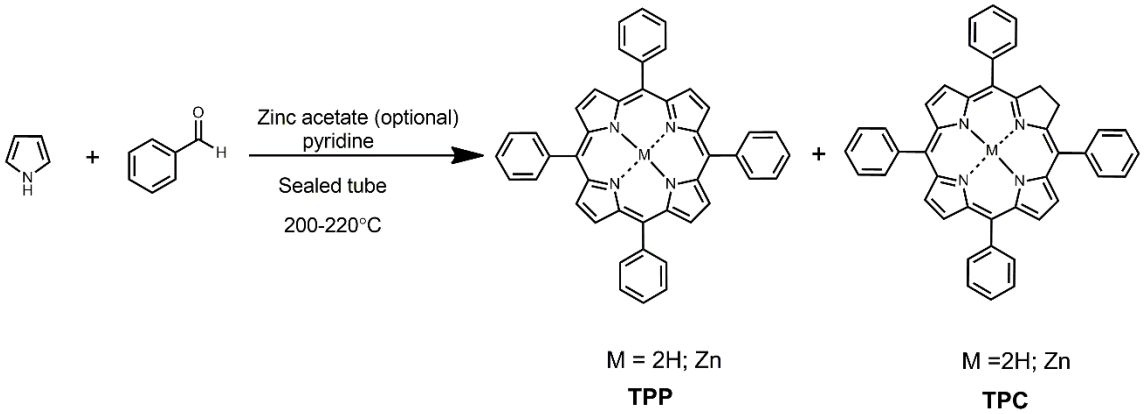

Scheme 1.9. Improved one-flask synthesis of *meso*-tetraphenylchlorin reported by Dorough and Huennekens.

Following an in-depth investigation of the synthesis of *meso*-substituted porphyrins reported by Rothemund, Calvin and co-workers isolated *meso*-tetraphenylchlorin

(H_2TPC) under modified reaction conditions, such as the introduction of zinc acetate to the vessel [53,54]. Subsequent work on improving the isolation of H_2TPC was done by Dorough and Huennekens [55], where they also reported on the preparation and characterisation of nine metal chelates (**Scheme 1.9**).

Provided that zinc acetate was used, after column chromatography to remove the zinc chelates of **TPP** and **TPC**, it is necessary to treat the free base **TPC** with hydrochloric acid to convert any zinc chlorin to the corresponding free base. The main disadvantage of this method is the tedious chromatographic process to isolate the chlorin from the porphyrin mixture. It was the method of choice for the synthesis of chlorins before the emergence of Whitlock's diimide reduction reaction of porphyrins.

1.5.2.2 Hydrogenation of Porphyrins

Due to the nature of the peripheral double bonds in porphyrins, they are notably 'cryptoolefinic' because they can undergo olefinic reactions, which is quite unusual for highly aromatic systems. Such reactions include the diimide reduction and the OsO_4-mediated dihydroxylation of *meso*-arylporphyrins into corresponding chlorins.

Notably, Whitlock's method [56] is one of the widely applicable methods in the generation of diimide for the reduction of porphyrins into chlorins. The reaction proceeds *via* the *in situ* generation of diimide from the thermal decomposition of *p*-toluenesulfonyl hydrazide. Typically, the reaction is carried out in the presence of pyridine, picoline and sodium carbonate as solvents/bases.

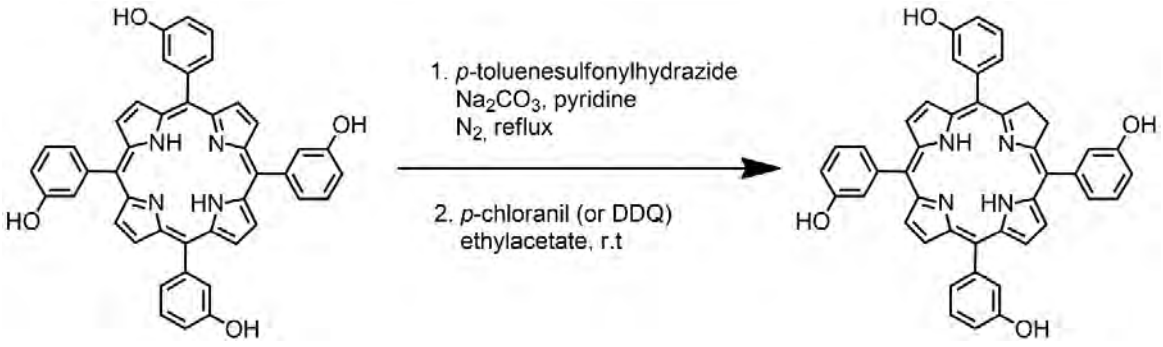

Scheme 1.10. Preparation of *m*-THPC, the active pharmaceutical ingredient of Foscan®.

As shown in **Scheme 1.10**, the second step requires that the mixture be treated carefully with oxidants such as *p*-chloranil or DDQ. This is necessary to convert the tetrahydroporphyrins (bacteriochlorin and isobacteriochlorin) to chlorin. In the mid-1980s, Bonnet and co-workers [57] reported that the *p*- and *m*-phenyl isomers of *meso*-tetrahydroxyphenylporphyrin have considerable activity against PC6 plasma cell tumours. This work led to European Union (EU) approval of the *m*-THPC under the trade name Foscan®.

Over the years, Whitlock's method has been simplified mainly by using alternative sources for generating diimide and solvents/bases to achieve milder reaction conditions. Secondly, the notably tedious separation of the complex mixture of porphyrins, chlorins and bacteriochlorins is now relatively facile [58–60]. In terms of milder reaction conditions, Pereira and co-workers [61] reported on the preparation of chlorins and bacteriochlorins *via* the diimide reduction of porphyrins in the complete absence of solvents and bases. Typically, this hydroporphyrin synthetic methodology relied on mixing the porphyrin with *p*-TsNHNH$_2$ in a ratio of 1:30 in an evacuated Schlenk tube heated to 140°C. These conditions afforded bacteriochlorins in good yields of *ca.* 84%. A ratio of 1:8 gave a complex mixture of unreacted porphyrin and corresponding chlorin and bacteriochlorin. Through

careful optimisation, the researchers found that a 1:15 ratio gave satisfactory yields of the chlorin contaminated with 10–20% bacteriochlorin. Additionally, Pereira and co-workers explored the use of Fenton's reagent (H_2O_2 and catalytic $FeCl_3$) for the selective dehydrogenation of bacteriochlorin to the corresponding chlorin.

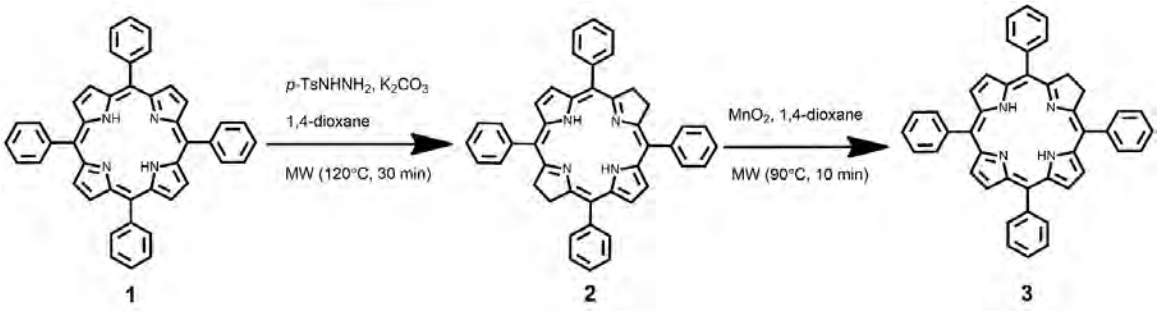

Scheme 1.11. Microwave-assisted synthesis of a chlorin by Nascimento and co-workers.

Nascimento and co-workers (**Scheme 1.11**) provided a much-improved hydrogenation method for converting porphyrin into dihydroporphyrin [62]. The procedure involves a two-step microwave synthesis; firstly, the starting porphyrin is treated with *p*-$TsNHNH_2$ according to Whitlock's reaction conditions. This step leads to the formation of a mixture comprising mostly bacteriochlorin, chlorin and very rarely porphyrin. The second step employs manganese (IV) oxide to carefully oxidise bacteriochlorin to chlorin in appreciable yields (with minor contamination with porphyrin). Although it might be stated that this method differs from the classic Whitlock method only by being a microwave-assisted reaction, this is not the case since the method also makes use of MnO_2 as an alternative oxidant to quinones such as chloranil and DDQ. Due to the heterogeneous nature of MnO_2, purification and isolation of the target chlorin (in high yields) is much more efficient and eco-friendly than is the case with Whitlock's method [62].

Notwithstanding the favourable optoelectronic properties of hydroporphyrins, they are inherently unstable and prone to oxidation at the expense of their

photophysical properties [63]. As a result, structural modulation of hydroporphyrins to afford photostable compounds with desirable photophysical properties is an area of extensive research. Many synthetic methods can be used to counter such oxidative degradation, some of which were reviewed by Galezowski and Gryko [64].

1.5.2.3 Other Miscellaneous Methods

Besides the reduction of the peripheral double bond *via* hydrogenation, there is an oxidative procedure to convert porphyrins to the corresponding chlorins. The reaction of OsO_4 with porphyrin proceeds to form vicinal dihydroxychlorins at the peripheral β,β′-bond, interestingly the reaction is stereospecific, leading to the formation of the *cis*-configuration of the diol. The history of chlorin chemistry shows that the vicinal dihydroxylation of porphyrins served as an important step for the modification of the β,β′-bond of porphyrins. This is exemplified in the synthetic pathway for gem-dialkyl oxochlorins upon and lactochlorins [52,65–67]. In 1985, Chang and Sotiriou were first to report that dihydroxychlorins resisted oxidation upon treatment with quinones. Additionally, upon treatment with sulfuric acid or perchloric acid under pinacol-pinacolone reaction conditions, the *vic*-dihydroxychlorins are transformed into oxochlorins [51,68].

1.5.3 N-confused porphyrin

Herein, a detailed description of the synthetic efforts made in N-confused porphyrin chemistry is provided. This includes the serendipitous discovery by two independent groups led by Latos-Grażyński and Furuta and the subsequent optimisation of the reaction conditions by Lindsey and co-workers for maximal yield. Thereafter, a brief account of the synthesis of doubly N-confused porphyrins is also provided.

1.5.3.1 First synthesis of N-confused porphyrin

Unlike the other macrocycles previously discussed, N-confused porphyrins are considered isomers of porphyrins in every sense of the word. N-confused porphyrins (NCP) were accidentally discovered as a side product in the acid-catalysed condensation of pyrrole and benzaldehyde. Independent reports on their synthesis were provided by the Furuta and Latos-Grażyński groups in 1994 [69,70]. Latos-Grażyński prepared the 5,10,15,20-tetra(*p*-tolyl)-2-aza-21-carbaporphyrin (H_2NCTTP) by the mixing of an excess of pyrrole with 4-methylbenzaldehyde in dichloromethane under the catalytic action of BF_3-etherate. The reaction is stirred in an inert atmosphere for one hour, followed by oxidation with *p*-chloranil. Subsequent chromatographic separation of the crude mixture afforded 4% of H_2NCTTP.

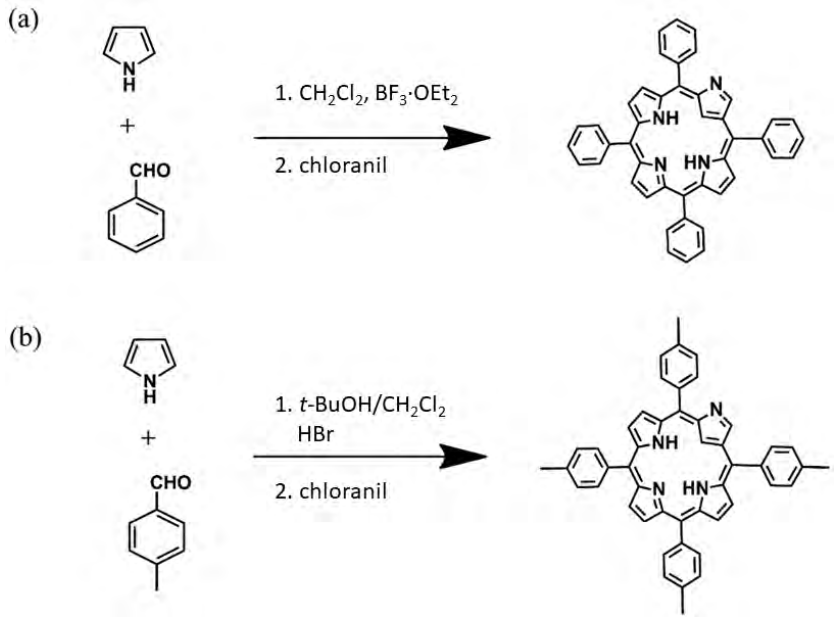

Scheme 1.12. The first independent accounts of the synthesis of N-confused porphyrins as reported by (a) Latos-Grażyński and co-workers and (b) Furuta and co-workers in 1994.

In parallel, Furuta and co-workers synthesised the N-confused porphyrin by replacing the conventional propionic acid with *tert*-BuOH/CH_2Cl_2 and concentrated

HBr. In detail, a mixture of pyrrole and benzaldehyde was stirred in the dark at room temperature for two days and subsequently oxidised with chloranil. Thereafter, workup of the reaction mixture and chromatography gave H_2NCTPP in 5–7% yields.

Both of these synthetic procedures are plagued by contamination of the target compound with normal porphyrin. In their first report on the isomer, Furuta *et al.* mentioned that in their methodology, the major product was still TPP rather than H_2NCTPP. As a result, studies on N-confused porphyrin chemistry were limited.

1.5.3.2 Improved synthetic route

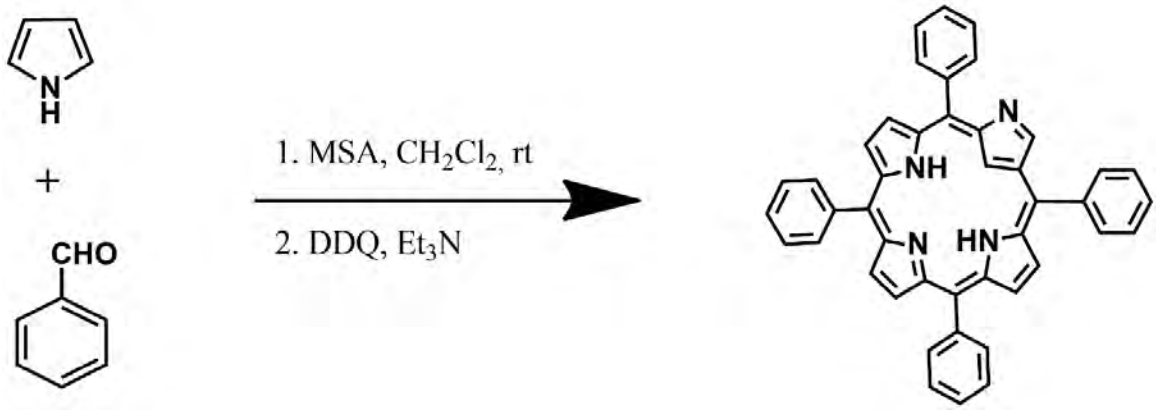

Scheme 1.13. Lindsey's procedure for the improved synthesis of H_2NCTPP.

Lindsey and co-workers offered a facile and improved one-pot synthetic route for N-confused porphyrins with reported yields of up to *ca.* 40% [71]. H_2NCTPP is obtained through the addition of methanesulfonic acid (MSA) to a well-stirred dichloromethane solution containing equimolar amounts of pyrrole and benzaldehyde. After 30 min, the reaction is oxidised by the addition of DDQ followed by the subsequent (after ~1 min) quenching of the acid by adding triethylamine (TEA) to the reaction mixture. Column chromatography on alumina

affords H_2NCTPP in highly appreciable yields that can be scaled-up to gram quantities.

Owing to the interest of porphyrin macrocycles with highly electron-withdrawing groups in the development of anion sensors [72,73], Furuta and co-workers took an interest in the synthesis (**Scheme 1.14**) of a *meso*-perfluorophenyl NCP (C_6F_5-NCP) [74]. In this regard, they developed a stepwise synthetic methodology since the one-pot synthetic route proposed by Lindsey resulted in a preferential formation of expanded porphyrins rather than the C_6F_5-NCP.

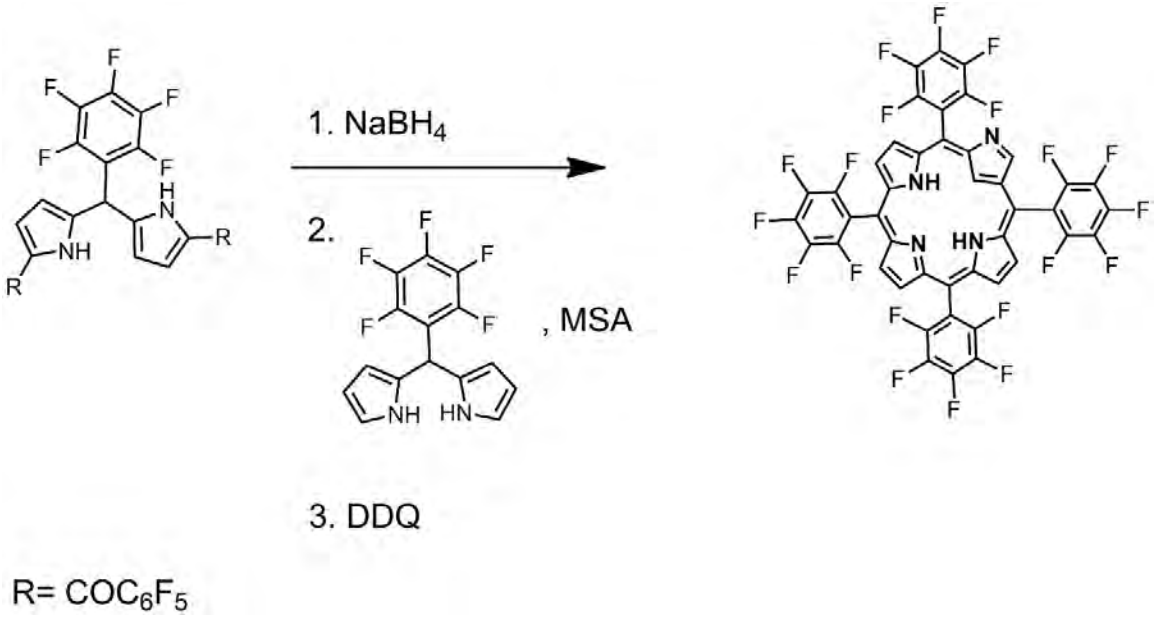

Scheme 1.14. Furuta and co-workers' stepwise synthesis of perfluorophenyl bearing N-confused porphyrin (C_6F_5-NCP).

The starting material, an N-confused dipyrromethane, was synthesised by the Friedel-Crafts reaction of perfluorophenyl substituted N-confused dipyrromethane. This was followed by the acid-catalysed condensation with normal dipyrromethane, and subsequent oxidation by DDQ afforded C_6F_5-NCP in *ca.* 21% yields.

Over the years, major synthetic efforts in N-confused porphyrin chemistry have been made. This is true in the sense that there has been an evolution from just a single carbon atom being in the cavity of the macrocycle to all of them being inside the coordination core [75]. This results in interesting properties such as the stabilisation of higher oxidation states. For example the doubly N-confused porphyrin 2-ethoxy-5,10,15,20-tetrapentafluorophenyl-3,7-diaza-21,22-dicarbaporphyrin (**N_2CP**) with its corresponding Ag(III) and Cu(III) complexes was synthesised by Furuta and co-workers [75,76]. This involved the acid-catalysed condensation of a pentafluoro-substituted N-confused dipyrromethane with pentafluorobenzaldehyde in $CHCl_3$; this was followed by oxidation with DDQ. Subsequent purification led to the free base doubly N-confused porphyrin (N_2CP) in 1-2% yields as shown in **Scheme 1.15**.

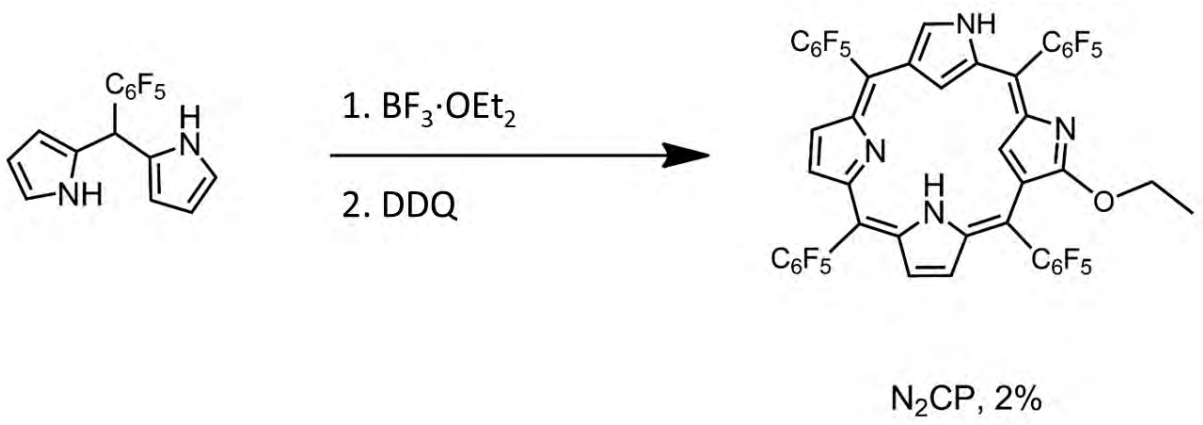

Scheme 1.15. Synthesis of doubly N-confused porphyrin (N_2CP) as described by Furuta and co-workers.

1.6 Electronic properties of porphyrins and their derivatives

In 1961, Martin Gouterman provided a seminal interpretation of the spectra of porphyrins through a comparison with a D_{16h} symmetry 16 atom 18 π-electron $C_{16}H_{16}^{2-}$ model species. The model came to be known as the four-orbital model. It can be readily used to explain the spectra of other tetrapyrrolic macrocycles, such as

reduced porphyrins and phthalocyanines [77,78]. Fundamentally, it states that the main porphyrin absorption bands result from transitions between the two highest occupied molecular orbitals (HOMOs) derived from the HOMO of the $C_{16}H_{16}^{2-}$ species with M_L = ±4 nodal patterns, and the two lowest unoccupied molecular orbitals (LUMOs) derived from the LUMO with M_L = ±5 nodal patterns. The intense B (or Soret) band in the blue region of the spectrum originates from allowed ΔM_L = ±1 transitions, and the weak Q bands in the red region arise from the forbidden ΔM_L = ±9 transitions. In the context of the D_{4h} symmetry of metal porphyrins, the a_{1u} and a_{2u} HOMOs are accidentally degenerate (**Figure 1.5**), while the LUMO is a doubly degenerate e_g orbital [79].

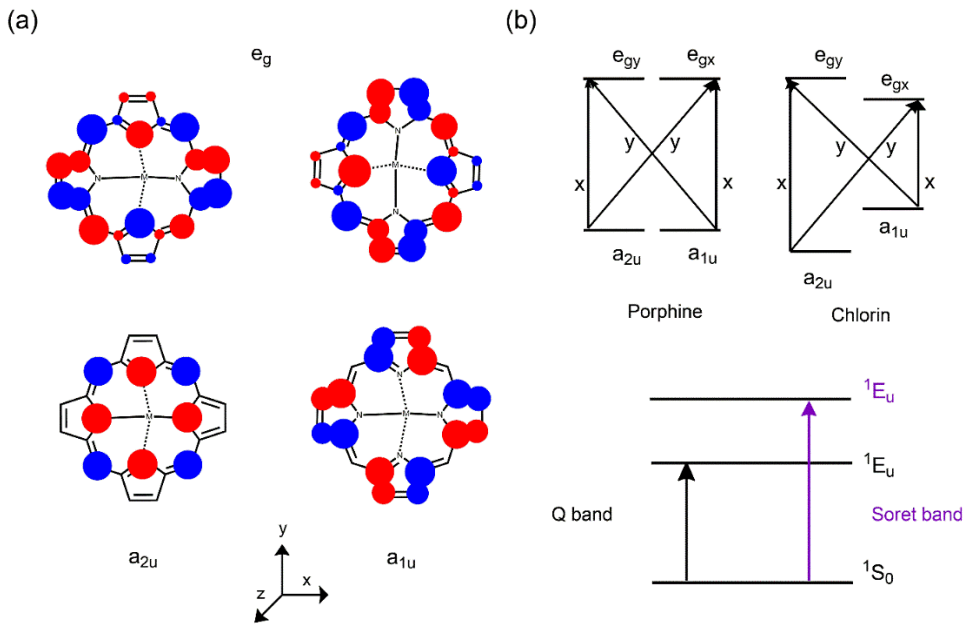

Figure 1.5. (a) The four frontier molecular orbitals model of porphyrins by Gouterman and the (b) energy level diagram of porphyrinoids and electronic transitions associated with porphyrins and chlorins.

In the context of free base porphyrins and the metal complexes of the low symmetry porphyrin derivatives in this study (**Figure 1.2**), the degeneracy of the LUMO is lifted for symmetry reasons. In this context, the energy separations of the MOs derived from the HOMO and LUMO of the $C_{16}H_{16}^{2-}$ species are referred to as the

ΔHOMO and ΔLUMO values, respectively. Gouterman demonstrated that when ΔHOMO and/or ΔLUMO are non-zero, there is a mixing of the allowed and forbidden properties of the B and Q bands so that the Q band can gain significant intensity. If this is accompanied by a narrowing of the HOMO–LUMO, this can also result in a significant red shift of the Q and B bands. The perturbations in the relative energies of the four orbitals due to peripheral modifications or symmetry changes can therefore be used to rationally modify the optoelectronic properties of porphyrins, chlorins, N-confused porphyrins (**Figure 1.6**), corroles and other porphyrin analogues in a manner that enhances their suitability for use in PDT. To better understand the effect of the structural modifications, a theoretical calculations section will be presented in Chapter 8.

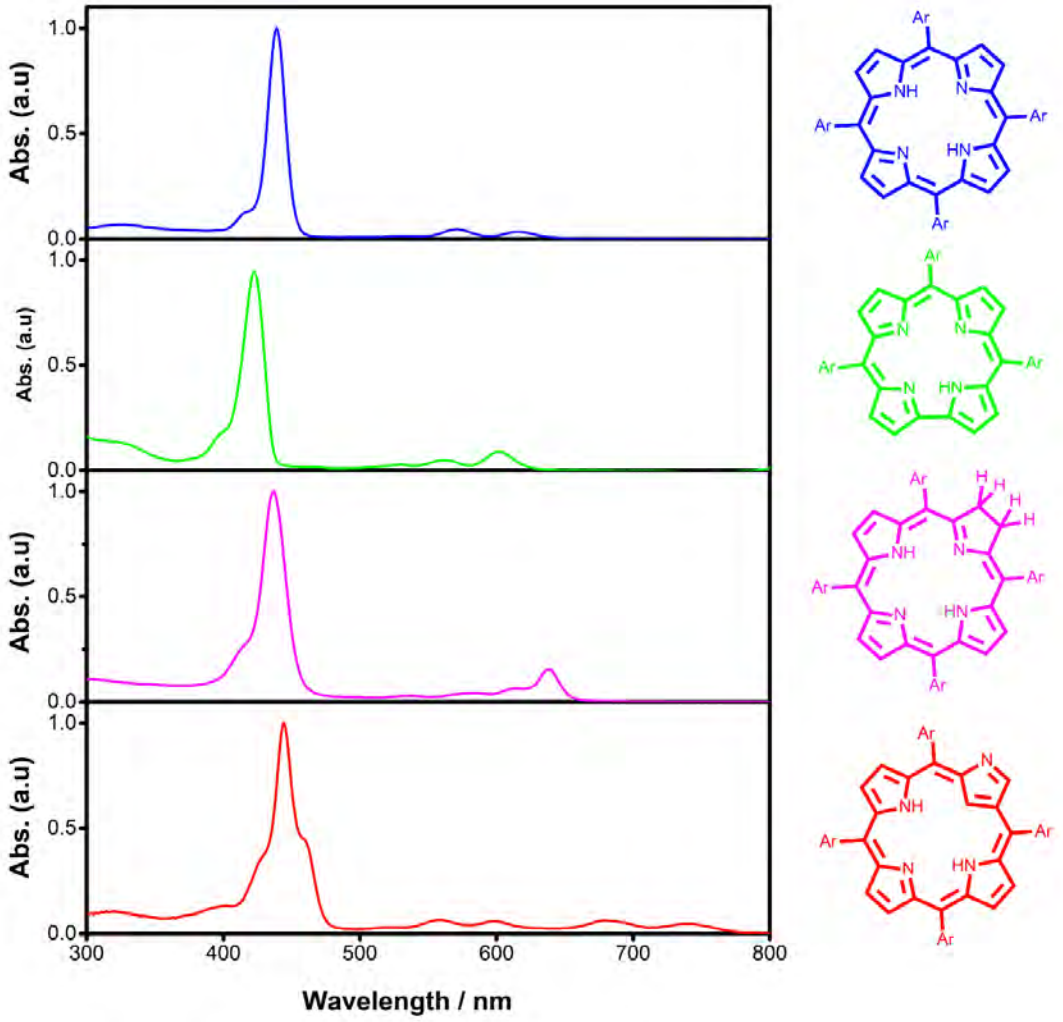

Figure 1.6. The typical groundstate absorption spectra of a porphyrin, corrole, chlorin and N-confused porphyrin. Ar= phenyl.

1.7 Photophysical properties

In this section, the main photochemical processes and photophysical properties relevant to photodynamic therapy are explored. The main focus will be on the photophysical behaviour of porphyrins and their low symmetry counterparts. The parameters under investigation are the singlet oxygen and fluorescence quantum yields and the fluorescence and triplet state lifetimes.

1.7.1 Fundamental aspects

Following the absorption of a photon by a particular molecule, energy is transferred from that photon to the particular electron. The electron transitions usually from the groundstate to a different eigenstate, say S_1, which corresponds to the amount of energy transferred. At this excited state (S_1), several decay mechanisms leading back to the groundstate can be followed. The first is a radiationless process either through vibrational relaxation (VR) or internal conversion (IC, assuming there is significant overlap between the vibrational and electronic energy states). In an alternative pathway, the molecule can dissipate the energy through the direct emission of a photon. This is called fluorescence (F). Interestingly, the molecule can also lose energy through a process called intersystem crossing (ISC). According to the spin selection rules, this qualifies as a forbidden transition which involves a change in the electron spin multiplicity from a singlet excited state to the triplet state. At this state, radiative decay from the triplet excited state to the groundstate can occur through a phenomenon known as phosphorescence (P). All these processes described above can be easily visualised using the Jablonski diagram in **Figure 1.7**.

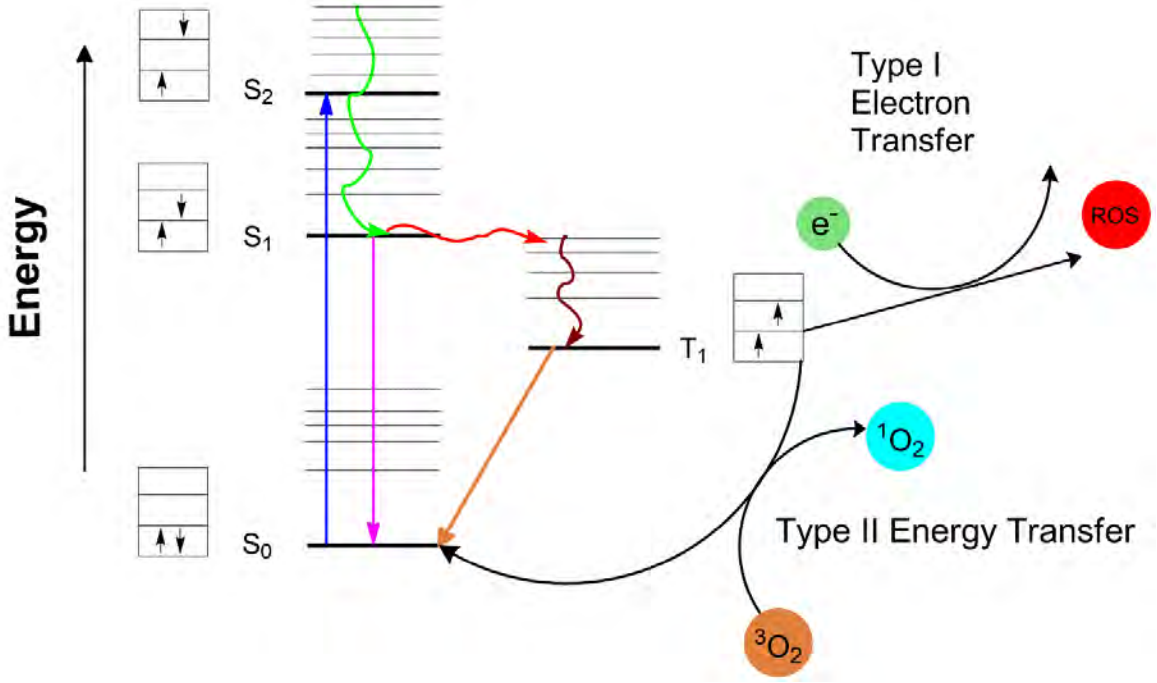

Figure 1.7. Jablonski diagram showing possible decay processes with absorption (A), vibrational relaxation (VR), fluorescence (F), intersystem crossing (ISC), internal conversion (IC) and phosphorescence (P).

1.7.2 Fluorescence quantum yields and lifetimes

Fluorescence is the emission of photons with a particular wavelength by a chemical compound (fluorophore) immediately after being excited with light of a certain wavelength [80]. This event occurs at a certain timescale after being excited, and it usually the order of *ca.* 10^{-6} to 10^{-8} seconds. With a few exceptions [81,82], fluorescence follows Kasha's rule, which states that emission occurs at the lowest vibrational level of the electronic state, S_1 [83]. Therefore, the processes that take place in the excited states are independent of the excitation wavelength.

One of the most useful methods to determine the efficiency of photosensitisers for different applications is to quantify the fluorescence quantum yield (Φ_F). In simple terms, it is the efficiency of a fluorophore to convert absorbed photons into emitted

light. Owing to their extensive conjugation and rigidity, porphyrins and related macrocycles have characteristic $S_1 \rightarrow S_0$ emission centred around 600–800 nm [5,84–86]. Studying the emission spectral properties associated with the Soret band (the $S_2 \rightarrow S_0$) presents a few problems of which are discussed in this reference [87].

When a comparative method is used, a comparison between the integral of the emission spectra of the sample and a known standard is made at the same experimental conditions. Therefore, Φ_F can be described by Equation (1.1):

$$\Phi_F = \Phi_{F\,(Std)} \frac{F.A_{Std}.\eta^2}{F_{Std}.A.\eta^2_{Std}} \qquad (1.1)$$

where F and F_{Std} are the areas under the fluorescence curves of the sample and standard, respectively. A and A_{Std} represent the absorbances of the sample and standard at the excitation wavelength, respectively. n and n_{Std} are the refractive indices of the solvent used for the sample and standard, respectively. Examples of well-known standards include fluorescein [88,89], Rhodamine 6G [89], tetraphenylporphyrin [90] and zinc phthalocyanine [86,90]. In this study, zinc tetraphenylporphyrin (ZnTPP in DMF, Φ_F= 0.033) was the standard most frequently used [91].

By definition, the fluorescence lifetime (τ_F) is the average time a fluorophore takes to return to the groundstate after being excited. Owing to the facile modification of the porphyrin periphery and the diverse coordination chemistry that is possible, it is difficult to provide a 'one-size fits all' description of fluorescence lifetimes. However, one can say that the fluorescence lifetime for the tetrapyrrolic compounds is long-lived, with values ranging from 0.1–20 ns [87].

Experiments to determine the τ_F value are mainly time-domain (e.g. TCSPC) based. After a short excitation pulse, the sample is monitored by measuring the emission intensity against time [92,93]. This generates a decay curve that, upon fitting, results in a lifetime measurement.

1.7.3 Singlet oxygen quantum yields

One of the principal goals in designing photosensitisers for phototherapeutic techniques is the efficient production of singlet oxygen ($^1O_2$) [13]. The interaction of an electronically excited photosensitiser in the triplet state with molecular oxygen ($^3O_2$) results in the formation of the short-lived singlet oxygen species, which initiate a cascade of biochemical reactions that ultimately lead to tissue destruction and cell death [94–96].

The routine method for the determination of singlet oxygen is to employ chemical traps that react with singlet oxygen produced by the oxygenated photosensitiser solution upon photoirradiation. The depletion of $^1O_2$ is then monitored spectroscopically at predetermined time intervals, thus providing a quantitative evaluation of singlet oxygen, namely the singlet oxygen quantum yield ($\mathbf{\Phi}_\Delta$). Singlet oxygen traps such as 1,3-diphenylisobenzofuran (DPBF) or 9,10-dimethylanthracene (DMA) are commonly used for the quantification of singlet oxygen in organic solvents. In this study, the singlet oxygen photogeneration rates were followed by DPBF consumption (λ_{Abs}=415 nm in DMF). The values of $\mathbf{\Phi}_\Delta$ were calculated using Equation (1.2):

$$\Phi_\Delta = \Phi_\Delta^{Std} \frac{R.I_{Abs}^{Std}}{R^{Std}.I_{Abs}} \qquad (1.2)$$

where S_S^{SSS} is the singlet oxygen quantum yield for the standard (ZnTPP, Φ_Δ=0.53 in DMF) [97]. *R* and R^{Std} are the photodegradation rates of DPBF in the presence of the sample and ZnTPP, respectively. $S_{SSS}S$and S_{SSS}^{SSS} are the rates of light absorption by the sample and standard, respectively. The concentration of DPBF in both the sample and ZnTPP reference was kept constant.

In addition to the above mentioned, the singlet oxygen was quantified using a Picoquant FluoTime 300 photon counter equipped with an NIR photomultiplier tube (PMT). This allows for the detection of the steady-state singlet oxygen phosphorescence signal at *ca.* 1270 nm upon excitation at 420 nm. From the area under the curve of the phosphorescence spectra, the Φ_Δ of the unknown sample can then be described by Equation (1.3):

$$\Phi_\Delta^S = \Phi_\Delta^{Std} \frac{I^S.A_{420}^{Std}}{I^{Std}.A_{420}^S} \quad (1.3)$$

where I^S and I^{Std} represent the area under the curve in the phosphorescence of singlet oxygen in the sample and the standard, respectively. A_{Std} and A_S represent the absorbances at the excitation wavelength (420 nm) of the standard and sample, respectively. Φ_Δ^{Std} (ZnTPP, 0.53 in DMF) [97] is the singlet oxygen quantum yield of the standard compound. For a detailed description of this comparative method, readers should consider the separate work done by the corresponding authors Shimizu and Denz [98,99].

1.7.4 Triplet Lifetimes (τ_T)

Due to the importance of the triplet excited state in both the Type I and II pathways responsible for the generation of reactive oxygen species (ROS), by extension, it can be rationalised that the lifetime of the photogenerated lowest excited triplet state (T_1)

can serve as a predictor of the efficiency of a photosensitiser to produce singlet oxygen. This is because longer triplet lifetimes increase the probability of collisions between groundstate oxygen with photosensitiser dyes in the excited triplet state and, consequently, a greater singlet oxygen production [100].

The τ_T values of porphyrinoids can be anywhere from microseconds to a few milliseconds, and this value is reported to decrease drastically in the presence of heavy metal ions [101,102]. This is largely attributed to the strong spin-orbit coupling interaction between the heavy central atom and the macrocycle that promotes spin-forbidden processes such as ISC and phosphorescence.

1.8 Photodynamic therapy (PDT) and antimicrobial PDT (PACT)

Photodynamic therapy, better known as PDT, is a minimally invasive treatment modality for cancer and other non-malignant conditions. The previously mentioned treatment makes use of a pro-drug (a photosensitiser), which is activated upon interaction with light of a specific wavelength [103]. Following the photoactivation of the photosensitiser, it can interact with the surroundings according to the reactions illustrated in **Figure 1.7** - Type I and Type II reactions. In a Type I reaction, the photosensitiser in the triplet excited state abstracts an electron from biological substrates such as lipids, proteins and nucleic acids to form a pair of free radical species of the photosensitiser ($Ps^{-}\cdot$) and corresponding biomolecule ($biomolecule^{+}\cdot$). In an oxygen-rich environment, a direct electron transfer from the $Ps^{-}\cdot$ to molecular oxygen ($^3O_2$) produces superoxide anion radicals capable of inducing stress on the tumour cells through a cascade of reactions with biologically relevant radicals such as nitric oxide [13,31,103–106].

In contrast, a type II reaction is characterised by the triplet excited photosensitiser transferring its energy to molecular oxygen, which exists in its most stable triplet state ($^3O_2$). Due to this direct energy transfer, one of the electrons is not only excited to a higher-energy orbital, but it also flips its spin and pairs up with the other to create singlet oxygen ($^1O_2$). Although it has been shown that both Type I and II reactions can both occur at the same time depending on various factors, singlet oxygen is considered the primary cytotoxic agent in PDT [103,107,108].

The FDA approval of Photofrin® for the treatment of oesophagal cancer in 1995 [109] led to the widespread development of improved photosensitisers, of which some have or are under the process of being clinically approved. To date, various types of cancer, including head, neck, pancreatic and prostate, have been treated through PDT [110–113]. The beauty of PDT lies in the fact that it is minimally invasive and can therefore be an outpatient therapy. In addition, recently developed photosensitisers display selectivity towards tumour cells and thus can be selectively destroyed through targeted or interstitial application of laser light. Compared to surgical resection of carcinomas, where post-operative mortality and morbidity is always a risk, PDT has been reported to offer high success rates for carcinoma with no serious adverse effects linked to it [109,114,115].

1.8.1 Porphyrinoid based photosensitisers in PDT

As previously mentioned, Photofrin® was one of the first photosensitisers to be clinically approved by the U.S. Food and Drug Administration (FDA). The active pharmaceutical ingredient (API) exists as a complex mixture of monomeric to oligomeric porphyrins derived from hematoporphyrin derivative (HpD). Extensive research and widespread clinical applications for Photofrin® have been reported with promising results during the treatment of aggressive primary glioblastomas

[116]. HpD shows an optimum absorption centred around 630 nm and thus can reach a penetration depth of *ca.* 0.5–1.0 cm depending on the tissue vasculature.

The drawbacks associated with HpD are that although the singlet oxygen quantum yield of the monomeric form of HpD is reported to be 64%, this value decreases significantly to 11% for the HpD dimer owing to aggregation in aqueous media [117]. Secondly, Photofrin® is reported to have relatively poor selectivity and slow clearance from the body at the prescribed 2 $mg.kg^{-1}$, leaving the skin photosensitised for prolonged periods [95]. Moreover, the photoactivation wavelength of this first generation (630 nm) prevents the treatment of deeper-seated tumours.

To overcome the limitations of Photofrin®, significant efforts have gone into the rational design of photosensitisers for PDT. Today it is well understood that the optical properties of biological tissue influence the penetration of light and hence the effect of PDT [118]. In this context, interest in porphyrin analogues such as chlorins, texaphyrins and phthalocyanines has grown to the point that some of them have been clinically approved or at least under clinical trials. Table 1.1 lists clinically approved (or under clinical trials) formulations that contain porphyrins and their analogues as the biologically active component.

Table 1.1 Selected tetrapyrrolic-based photosensitisers approved for clinical use.

Tradename	Active drug	λ (nm)	Details	Indications	Refs
Photofrin®	HpD	630	1st generation photosensitiser that at absorbs at ca. 630 nm - limited tissue penetration.	Barrett's oesophagus	[114,115]
Levulan®	ALA	630	Converted to protoporphyrin IX within the cells. ALA is not highly active - hence long periods of treatment needed.	Lung cancer	
Foscan®	m-THPC	652	Highly active. However, it is associated with pain and even out of sun photosensitivity.	Actinic Keratosis	[2,96,115,119]
Radachlorin®	Ce6	662	Composition of three chlorins. Excreted by 48 h and good tolerability by patients.	Basal cell lesions	
Photosens®	AlPc	670	Phthalocyanine based platform. Degree of peripheral sulfonation affects intracellular localisation and excretion rate.	Oral cavity leukoplakia	[120,121]
Purlytin®	Purpurin	660	Chlorin based PS. Efficient for short therapy. However, it shows poor stability in aqueous solutions.	Basal cell lesions	

1.8.2 Photodynamic antimicrobial chemotherapy (PACT)

Ironically, the advent of PDT came about through the inactivation of microorganisms [125,126]. The mechanism behind the photosensitisation is essentially identical to that of anticancer PDT. In that regard, it should be noted that the criteria for photosensitisers for PACT are different from that of anti-cancer PDT. For one, most infections addressed by PACT are more superficial rather than systemic and hence there is no need for excitation at long-wavelengths [126].

Phenotypically, bacteria can be classified as either Gram-(+) or Gram-(-). Gram-(+) bacterial strains possess a thick peptidoglycan layer and no lipid layer, whilst in Gram-(-) bacteria, the peptidoglycan layer is thin and has a lipid layer. It is this difference in the cell wall structure that largely determines the susceptibility of the bacteria towards photosensitisers. The absence of a lipopolysaccharide layer (LPS) in Gram-(+) bacteria makes them susceptible towards neutral, anionic and cationic photosensitiser dyes. On the other hand, the outer membrane Gram-(-) strains consisting primarily of LPS reportedly make them resistant towards inactivation by neutral and anionic photosensitiser dyes [127].

Due to the limited application of porphyrin derivatives such as chlorins and N-confused porphyrins as PACT photosensitisers, we will explore how they photoinactivate *S. aureus* and *E. coli* bacterial cultures.

1.9 Thesis outline

This dissertation explores the synthesis and spectroscopic characterisation of porphyrins and their low symmetry derivatives. The INI group at Rhodes University has demonstrated that incorporating Sn(IV) at the central cavity of porphyrins leads

to interesting optoelectronic and biological properties, so tin(IV) complexes of the derivatives were also explored.

Tin(IV) complexes of 4-methylthiophenyl functionalised porphyrin and the corresponding corrole, chlorin and N-confused porphyrin derivatives were synthesised to shift the satellite Q bands at longer wavelengths well into the phototherapeutic window for efficient PDT activity. From this standpoint, the photophysical properties of the photosensitisers were assayed.

The photophysical properties of the porphyrin derivatives prompted the study on their *in vitro* activity against the MCF-7 breast cancer cell line. Additionally, the *in vitro* PACT of the chlorin and N-confused porphyrin entities were studied on *S. aureus* and *E. coli*. Finally, the reduced symmetry of the porphyrin derivatives provided interesting optical properties, which were further investigated through theoretical calculations.

Chapter 2

Experimental

This chapter details the materials, instrumentation, synthetic methodology and characterisation methods for all the compounds used in this work.

2.1 Materials

All chemicals used in this study were purchased from commercial sources and were used as received unless otherwise stated. Reagent grade propionic acid, pyrrole, *p*-chloranil, 2,3-dichloro-5,6-dicyano-*p*-benzoquinone (DDQ), 4-(methylthio)benzaldehyde, 1,3-diphenylisobenzofuran (DPBF), triethylamine (TEA), magnesium sulfate anhydrous and 5,10,15,20-tetraphenyl-21H,23H-porphine zinc (ZnTPP) were purchased from Sigma Aldrich. Similarly, deuterated chloroform ($CDCl_3$) and dimethyl sulfoxide (DMSO-d_6) were also purchased from Sigma Aldrich. Ethylacetate, chloroform, dichloromethane, dimethylformamide (DMF), hexanes and methanol were procured from Merck. $SnCl_2{\cdot}2H_2O$ and aqueous ammonia were purchased from Fluka and Minema chemicals, respectively. Ultra-pure Type II water was obtained from an Elga Purelab Chorus 2 (RO/DI) system.

Cultures of MCF-7 cells were obtained from Cellonex®, heat-inactivated fetal calf serum (FCS) and tissue culture grade penicillin-streptomycin-amphotericin B mix, 100 units.mL^{-1} penicillin, and 100 μg.mL^{-1} streptomycin-amphotericin B were purchased from Biowest®. Dulbecco's phosphate-buffered saline (DPBS), and Dulbecco's modified Eagle's medium (DMEM) were obtained from Lonza®. The MTT assay kit was procured from Sigma Aldrich.

2.2 Equipment

- **Groundstate absorption spectra** were collected on a Shimadzu UV-2550 spectrophotometer and Evolution™ 350-UV-Vis spectrophotometer from Thermo Fischer Scientific™.

- **Fluorescence emission spectra** were recorded on a Varian Eclipse spectrofluorometer.
- **Fluorescence lifetimes** were measured using the time-correlated single photon counting (TCSPC) setup (FluoTime 30, Picoquant Gmbh). For this study, a diode laser excitation source (LDH-P-C-420, 20 MHz repetition rate) was used. The fluorescence signal was detected with a thermoelectric cooled MCP-PMT module. The instrument response function (IRF) was measured with the scatter sample, Ludox® from DuPont. The data were analyzed with the in-built FluoFit software (Picoquant Gmbh), and the error in the decay times was estimated using support plane analysis.
- **^{1}H Nuclear Magnetic Resonance (^{1}H-NMR) spectra** were recorded using a Bruker Avance II™ 600 MHz and AMX 400 MHz spectrometers.
- **Mass spectral data** were collected on a Bruker AutoFLEX III Smartbeam TOF/TOF mass spectrometer driven in the positive ion mode with a 354 nm nitrogen laser as the ionising source. The MALDI matrix was α-cyano-4-hydroxycinnamic acid.
- **Magnetic circular dichroism spectra** were measured using a Chirascan plus spectrodichrometer equipped with a 1.0 T permanent magnet by using both the parallel and antiparallel fields. The conventions described by Piepho and Schatz are used to describe the sign of the MCD signal and Faraday terms [128].
- **The $^1O_2$ quantum yields** were quantified using two comparative methods with DMF as the solvent of choice. Firstly, the Spectra-Physics® Primoscan OPO series (GWU Lasertechnik Vertriebsges, mbH) pumped with a Spectra-Physics Quanta-Ray Lab Nd:YAG laser. The irradiation wavelength was the crossover between the absorbance of the standard (ZnTPP) and the sample. The second comparative method was a single photon counting method which involved the detection of $^1O_2$ luminescence at *ca.* 1270 nm after excitation of

both the sample and ZnTPP at 420 nm with a diode laser source (LDH-P-C-420, 20 MHz repetition rate). The detection was achieved using a thermoelectric cooled NIR-PMT unit (H10330C, Hamamatsu).

- **The triplet state lifetimes and transient absorption spectra** were recorded in DMF at 480 or 500 nm using an Edinburgh Instruments LP980 spectrometer and an Ekspla NT-342B laser equipped with an OPO to provide an excitation wavelength (2.0 mJ excitation energy, 7 ns pulse duration and a 20 Hz repetition rate). The solutions were degassed with nitrogen for 20 min prior to measurement, and the absorbances were maintained at *ca.* 1.5 for the Soret band. Exponential curve fitting of the decay curve using OriginPro 8 software provided the triplet lifetimes.
- The Council for Scientific and Industrial Research's (CSIR) Centre for High Performance Computing (CHPC) in Cape Town was used as a platform to perform the theoretical calculations with the Gaussian software package [129]. **Geometry optimisations** were carried out at the B3LYP level of theory with SDD basis sets, while **TD-DFT calculations** used the Coulomb-attenuated B3LYP (CAM-B3LYP) functional with SDD basis sets. The simulated spectra were generated using Chemcraft software with a fixed bandwidth at 2000 cm^{-1}, and the molecular orbitals were visualised with Avogadro [130,131].
- **The MCF-7 cells** were cultured in Porvair 25 cm^2 flasks, and during their log phase, the cells were passaged to 75 cm^2 Porvair flasks kept in a humidified atmosphere incubator from Heal Force (37°C, 5% CO_2). A Zeiss AxioVert.A1 inverted microscope was used to examine the cells under contrast methods such as fluorescence and phase contrast illumination.
- **PDT studies** were conducted using a Modulight® Medical Laser system (ML, 7710-680) fitted with a Thorlabs LED. The MTT assay was used to determine the cell viability and proliferation with the help of a Synergy™ multi-mode microtiter plate reader from BioTek®.

- **An autoclave from China Medical Device (RAU-530D)** was used to sterilise the Luria broth, agar, PBS and all the equipment deemed necessary for bacterial culturing.
- **The optical density (OD) of the bacterial culture** was measured using Ledetect 96 microplate reader from Labxim products.
- **The bacterial suspensions were mixed** with a Lasec® analogue vortex mixer.
- **The bacterial pellet** was obtained from the suspension by using a Hemle Z233M-2 centrifuge from Lasec®.
- **The colony-forming units (CFU.mL^{-1})** were determined by Scan® 500 series automatic colony counter from Interscience.

2.3 Synthesis

2.3.1 5,10,15,20-*tetrakis*(4-(methylthio)phenyl)porphyrin (1), Scheme 3.1

Following the Adler-Longo method for porphyrin synthesis [24], 300 mL of propionic acid was added to a 1 L round bottom flask, followed by freshly distilled pyrrole (8 mmol). The reaction vessel was briefly warmed, and 4-(methylthio)benzaldehyde (8 mmol) was slowly added to the flask. The contents were refluxed for 4 h and subsequently cooled to room temperature to precipitate out the product. The product was vacuum filtered, and the filter cake was thoroughly washed with water, followed by cold methanol and then dried *in vacuo*. Chromatographic separation of the crude product (silica, $CHCl_3$) afforded **1**. Yield: 38%; ^{1}H NMR ($CDCl_3$, 400 MHz): δ_H 8.87 (s, 2H), 8.49 (d, J = 10.2 Hz 10H), 8.13 (d, J = 7.80 Hz, 2H), 7.83 (d, J = 7.90 Hz, 6H), 7.63 (d, J = 7.60 Hz, 4H), 2.80 (s, 6H), 2.76 (s, 6H). MS (MALDI-TOF): m/z for $[M+H]^+$ = 800.02 (calc. 798.20).

2.3.2 5,10,15,20-*tetrakis*(4-methylthiophenyl)porphyrinato tin(IV) (1-Sn), Scheme 3.1

1 (250 mg) was dissolved in dry pyridine, and two equivalents of $SnCl_2 \cdot 2H_2O$ was added. The contents were refluxed for 2 h, and the progress of the reaction was monitored by thin-layer chromatography (TLC) and ground state absorption spectroscopy. The reaction vessel was cooled to room temperature, and concentrated aqueous ammonia (12.5 mL) was slowly added to the flask and refluxed for an additional hour. Water was added to the cooled flask to induce precipitation, and the product was collected through filtration. After several washes with water, the product was digested with chloroform leaving behind tin salt. The solvent was evaporated from the filtrate. Column chromatography (Silica, $CH_3OH/CHCl_3$, 1:100) provided the pure product. Yield: 74%. ^{1}H NMR ($CDCl_3$, 600 MHz): δ_H 9.25 (s, 8H), 8.23 (d, J = 7.98 Hz, 8H), 7.69 (d, J = 7.92 Hz, 8H), 2.78 (s, 12H). MS (MALDI-TOF): m/z for $[M+H]^+$ = 952.05 (calc. 950.09), $[Sn{-}(OH)_2]^+$ = 917.05 (calc. 916.07).

2.3.3 5,10,15-*tris*(4-methylthiophenyl)corrole (2), Scheme 3.1

Following a well-documented procedure for synthesizing symmetric A_3 triarylcorroles [48], 4-(methylthio)benzaldehyde (10 mmol) and pyrrole (20 mmol) were dissolved in 400 mL of methanol, and 400 mL of water was added. Aqueous hydrochloric acid (36%, 8.5 mL) was then added, and the reaction was stirred at room temperature for 3 h. The mixture was extracted with chloroform and washed three times with water. The organic phase was dried with sodium sulphate and subsequently reduced to 400 mL on a rotary evaporator. The oxidant, *p*-chloranil (10 mmol) was added and the mixture was refluxed for 1 h. The solvent was evaporated, and chromatographic separation (Silica, $CHCl_3$/Hexanes, 2:3) was carried out to yield

the A_3 corrole target compound, which was dried *in vacuo*. Yield: 28%. MS (MALDI-TOF): *m*/*z* for $[M]^+$ = 664.79 (calc. 664.90).

2.3.4 5,10,15-*tris*(4-methylthiophenyl)corrolato tin(IV)-dichloride (2-Sn), Scheme 3.1

2 (200 mg, 0.30 mmol) and two equivalents of $SnCl_2 \cdot 2H_2O$ (592 mg, 3.12 mmol) were dissolved in 15 mL of dry DMF and refluxed for 90 min. The reaction mixture was cooled to room temperature and extracted from DMF using chloroform and water. Column chromatography (silica, CH_3OH/CH_2Cl_2, 1:100) was used to collect a pink coloured band. The solution was subsequently evaporated to dryness. TLC analysis, ground state absorption spectroscopy of the free base corrole and characterisation of the product of this reaction confirmed the formation of **2-Sn**. Yield: 79%. ^{1}H NMR (DMSO-d_6, 600 MHz): δ_H 9.33 (s, 4H), 8.75 (m, 4H), 8.22 (m, 6H), 7.78 (m, 6H), 2.78 (s, 3H), 2.74 (s, 6H). MS (MALDI-TOF): m/z for $[M]^+$ = 816.56 (calc. 816.03), $[Sn{-}Cl]^+$ = 781.57 (calc. 780.59).

2.3.5 5,10,15,20-*tetrakis*(4-methylthiophenyl)chlorin (3), Scheme 3.2

A solution of **1** (0.05 mmol) and potassium carbonate (2 mmol) dissolved in dry pyridine (15 mL) was refluxed under a nitrogen atmosphere, and *p*-toluenesulfonyl hydrazide (2 mmol) was added at 3 h intervals for a total of 12 h. The reaction mixture was cooled to room temperature, poured into ethyl acetate/water (2:1) and heated to reflux for an additional 1 h. Upon cooling, the organic phase was separated and washed three times with 2 M HCl followed by water (150 mL × 3). The organic phase was then washed with a sodium carbonate solution (150 mL × 2) followed by drying over anhydrous sodium sulphate, and finally filtered and concentrated *in*

vacuo. Column chromatography (silica, $CHCl_3$) afforded **3** as purple crystals. Yield: 32%. ^1H NMR ($CDCl_3$, 600 MHz) δ_H ppm ^1H NMR ($CDCl_3$, 600 MHz) δ_H, ppm 8.61 (d, *J* = 4.6 Hz, 2H), 8.46 (s, 2H), 8.23 (d, *J* = 4.7 Hz, 2H), 8.04 (d, *J* = 7.4 Hz, 4H), 7.80 (d, *J* = 7.6 Hz, 4H), 7.61−7.57 (m, 8H), 4.18 (s, 4H), 2.74 (s, 6H), 2.72 (s, 6H). MS (MALDI-TOF): *m*/*z* 800.47 (calc. for $[M + H]^+$ 798.20).

2.3.6 Dichloro-[5,10,15,20-*tetrakis*(4-methylthiophenyl)chlorinato tin(IV)] (3-Sn), Scheme 3.2

Free base chlorin **3** (50 mg, 0.061 mmol) was dissolved in 5 mL chloroform and placed in a 25 mL round bottom flask. The metal salt and $SnCl_2{\cdot}2H_2O$ (231 mg) dissolved in 5 mL methanol were added to the round bottom flask and heated to reflux for 16 h. The consumption of the starting material was monitored by TLC. Upon completion, the reaction was dried *in vacuo*. The residue was chromatographed on silica (MeOH/$CHCl_3$, 1:100) to afford green crystals of **3-Sn**. Yield: 78%. ^1H NMR ($CDCl_3$, 600 MHz) δ_H ppm 8.60 (d, *J* = 4.8 Hz, 2H), 8.49 (s, 2H), 8.12 (dd, *J* = 6.5, 3.5 Hz, 3H), 8.02 (s, 2H), 7.93 (d, *J* = 8.2 Hz, 3H), 7.69 (d, *J* = 8.2 Hz, 2H), 7.64 (d, *J* = 8.2 Hz, 2H), 7.61−7.51 (m, 6H), 4.25 (s, 4H), 2.96 (s, 6H), 2.88 (s, 6H). MS (MALDI-TOF): *m*/*z* 953.33 (calc. for $[M^+\text{-Cl}]$ 953.27).

2.3.7 5,10,15,20-*tetrakis*(4-methylthiophenyl)-2-aza-21-carbaporphyrin (4), Scheme 3.3

The free base N-confused porphyrin (**4**) was prepared by the reported method [71]. Yield: 37%. ^1H NMR ($CDCl_3$, 600 MHz) δ_H ppm 8.96 (d, *J* = 4.6 Hz, 1H), 8.91 (d, *J* = 4.8 Hz, 1H), 8.71 (s, 1H), 8.60 (d, *J* = 4,9 Hz, 2H), 8.56 (d, *J* = 4.7 Hz, 2H), 8.30 (d, *J* = 8.2 Hz, 2H), 8.25 (d, *J* = 8.2 Hz, 2H), 8.07 (t, *J* = 8.2 Hz, 4H), 7.72 (d, *J* = 8.3 Hz, 4H), 7.63

(dd, *J* = 8.3 Hz, 4H), 2.75 (d, *J* = 2.6 Hz, 8H), 2.72 (s, 4H). MS (MALDI-TOF): *m*/*z* 799.34 (calc. for $[M+H]^+$ 798.20).

2.3.8 Dichloro-[5,10,15,20-*tetrakis*(4-methylthiophenyl)-2-aza-21-carbaporphyrinato tin(IV)] (4-Sn), Scheme 3.3

In dry pyridine, **4** (50 mg, 0.63 mmol) and tin(II) chloride (12.6 mmol) were heated to reflux under a nitrogen atmosphere for 5 min and the reaction mixture was instantly poured into cold hexane to induce precipitation. The crude product was washed with cyclohexane (50 mL × 3), digested with CH_2Cl_2 and dried under reduced pressure. The residue was dissolved in minimum amount of CH_2Cl_2 and chromatographed (silica, MeOH/CH_2Cl_2, 1:25) to afford **4-Sn**. Yield: 31%. ^{1}H NMR ($CDCl_3$, 600 MHz) δ_H, ppm 10.68 (br, 1H), 8.70 (s, 1H), 8.51 (d, *J* = 4.6 Hz, 1H), 8.42 (d, *J* = 4.8 Hz, 1H), 8.28 (s, 2H), 8.17 (d, *J* = 4.3 Hz, 2H), 7.92 (d, *J* = 8.0 Hz, 4H), 7.83 (d, *J* = 7.8 Hz, 2H), 7.73 (d, *J* = 6.4 Hz, 2H), 7.53 (m, 6H), 7.41 (d, *J* = 6,1 Hz, 2H), 2.69 (d, *J* = 2.4 Hz, 8H) 2.68 (s, 4H). MS (MALDI-TOF): *m*/*z* 951.29 (calc. for $[M-Cl]^+$ 951.25).

2.4 Photostability experiments

The photoinduced transformation of a photosensitiser in solution is known to alter its spectral properties such that the photodynamic activity might be affected. Therefore, this is an important parameter for sensitisers in light-based applications [133, 134]. The photostability test was carried out in a quartz cuvette (1 × 1 cm), and the solutions were irradiated for 30 minutes with a 625 (240 mW.cm^{-2}) or 660 nm (280 mW.cm^{-2}) Thorlabs LED lamp mounted on top of a make-shift housing unit to prevent unnecessary ambient light from reaching the sample. To control the amount

of current running through the LED, a LEDD1B T-cube LED driver (Thorlabs) was connected. Typically, the solutions are prepared in the dark by dissolving 1 mg / 6 mL of sample in 1% DMSO/H_2O and transferred to a tightly sealed quartz cuvette. The bleaching of the dyes at the absorption peak was monitored as a function of time. The amount of dye (as a percentage) remaining after 30 min of irradiation is shown in **Table 5.2.**

2.5 Time-dependent cellular uptake

In 96-well plates, MCF-7 cells were seeded at a density of approximately 10^4 cells.cm^{-2} and allowed to grow for 24 h. The cells were treated with 10 μM of freshly prepared Sn(IV) complexes in PBS over different time intervals (12, 24 and 48 h) at 37 °C. After the incubation, the cells were washed twice with PBS to remove any extracellular compounds and then lysed in 100 mL of 30% Triton X-100 in DMSO. The Sn(IV) complexes accumulated inside the cell were then analyzed by fluorescence by using a microplate reader (λ_{ex} 430 nm, λ_{em} 630 nm). Measurements were made in triplicate, so a standard deviation could be calculated.

2.6 Cell culture and *in vitro* studies on MCF-7 cancer cells

2.6.1 *In vitro* dark toxicity

In vitro dark toxicity studies were performed on Michigan Cancer Foundation (MCF-7) human epithelial breast cancer cells before carrying out *in vitro* PDT studies. The cells were cultured using Dulbecco's modified Eagle's medium (DMEM) modified with 4.5 $g.L^{-1}$ glucose, L-glutamine and phenol red. The DMEM was supplemented with 10% heat-inactivated FCS, moreover a penicillin-streptomycin-amphotericin B

mix, 100 units.mL^{-1} penicillin, and 100 μg.mL^{-1} streptomycin-amphotericin B was added. The cells were grown in 75 cm^2 Porvair® flasks with vented caps and were incubated at 37 °C in a humidified atmosphere containing 5% CO_2. Regular subculturing *via* trypsinisation was performed, and the detached cells were treated with trypan blue (0.4%) and examined for viability with a hemocytometer. At a density of 10000 cells per well, the cells were seeded in DMEM modified with phenol red in 96 well tissue culture plates (Porvair) and kept in a 5% CO_2 incubator maintained at 37 °C for 24 h. The adherent cells were washed twice with 100 μL of DPBS. Subsequently, 100 μL of DMEM solution containing the compounds under study at varying concentrations was added, and the solutions were incubated for 24 h in the dark. Vehicle control cells were incubated with the supplemented DMEM only. After 24 h had elapsed, the wells were rinsed twice with 100 μL of DPBS followed by the addition of supplemented DMEM containing phenol red and the cells were incubated for a further 24 h.

The cytotoxicity of all the compounds was assessed by the standard MTT assay [134]. The tetrazolium ring of MTT is cleaved by mitochondrial reductase in viable cells to form formazan crystals which are solubilised in DMSO, so that cell death can be estimated by measuring its absorbance at 540 nm using a Synergy™ multi-mode microtiter plate reader from BioTek®. The quantity of formazan formed hence provides a measure of the number of viable cells. The percentage cell viability is given by Eq. (2.1):

$$\%\ cell\ viability = \frac{Absorbance\ of\ sample\ at\ 540\ nm}{Absorbance\ of\ control\ at\ 540\ nm} \times 100 \qquad (2.1)$$

where absorbance of the sample is the absorbance value for the cells that were treated with the photosensitisers and the absorbance of the cells treated with supplemented DMEM with phenol red only. Both absorbance values were taken at 540 nm.

2.6.2 *In vitro* PDT

The cells were incubated by following the same procedure as explained in the previous section, and the compounds were added with varying concentrations of the photosensitisers (0.78–50 μM) dissolved in 1% DMSO. The cells treated with only media served as the vehicle control. After 24 h of treatment, the media was replaced with PBS, and the MCF-7 cells in the plates were treated with compounds **1**, **1-Sn**, **2**, **2-Sn, 3**, **3-Sn**, **4** and **4-Sn**. After this, the plates treated with **1**, **1-Sn**, **2** and **2-Sn** were photoirradiated with a Thorlabs M625L3 625 nm LED for 30 min (432 $J.cm^{-2}$). For **3**, **3-Sn**, **4**, and **4-Sn**, this was achieved by photoirradiation of the plates for 30 min with a Thorlabs M660L4 660 nm LED (280 $mW.cm^{-2}$). In both sets, the LED was mounted into the housing of a Modulight 7710–680 medical laser system. After irradiation, PBS was replaced with 10% freshly prepared DMEM and incubated for 24 h. After this period, cell viability was assayed using the MTT protocol method and equation provided in section **2.6.1**.

An important parameter in assessing the efficacy of photosensitisers during *in vitro* PDT is the IC_{50} value. In the context of PDT, it is the concentration of the photosensitiser that promotes a 50% cell kill after incubation followed by light treatment. Nonlinear regression analysis with GraphPad Prism 5 was used to determine the IC_{50} values of the compounds.

2.7 Bacterial inactivation studies

Staphylococcus aureus (ATCC® 25923™) and *Escherichia coli* (ATCC®, 25922™) were used for the PACT studies. Both bacteria were grown on agar plates according to the manufacturer guidelines to obtain the respective bacterial colonies. The respective

single colonies were inoculated into freshly prepared Luria nutrient broth; the resulting cultures were swirled and placed in a shaking incubator (37 °C, 200 rpm) for 18 h and 6 days for *S. Aureus* and *E. coli*, respectively. An aliquot of the culture was transferred into freshly prepared broth (4 mL) and further incubated at 37 °C. The optical density (OD 600 nm ~ 0.6–0.7) of the bacterial culture was taken regularly to ensure mid-logarithmic growth, and broth culture was removed by centrifugation at 3000 rpm for 15 minutes. The independent bacterial pellets of *S. aureus* and *E. coli* were washed thrice with PBS to remove residual nutrient broth. After resuspension in 4 mL PBS, they were diluted to 1:1000 (v/v) with PBS to afford the working stock solutions.

The PACT studies were carried out using the previously reported viable count method [135]. The compounds under study: **3**, **3-Sn**, **4** and **4-Sn** are insoluble in water, and hence the antimicrobial studies were performed in 2% DMSO in PBS. With regards to the experimental procedure, 20 μL of the compounds were mixed with 1.98 mL of the individual bacterial suspensions of *S. aureus* and *E. coli* in PBS to a final concentration of 2.5 and 10 μM, respectively. The mixtures were placed in a shaking incubator set at 37 °C for 30 min. Half (1 mL) of the mixture was irradiated at 660 nm in a 24 well plate at predefined time-intervals (t_n, where n =0, 15, 30, 45, 60 and 75 min) while the other 1 mL of the mixture was placed in 24 well plates and kept in the dark for the same time-intervals, t_n. After treatment, 100 μL of the sample exposed either to light or dark conditions was inoculated onto agar plates while maintaining an aseptic environment. The plates were then placed in an incubator at 37 °C for 24 h before colony count determination. The colony-forming units (CFU/mL) of bacteria were counted using a Scan® 500 automatic colony counter.

Chapter 3

Synthesis and structural characterisation

This chapter describes the synthesis and characterisation of the photosensitisers.

3.1 Synthesis and characterisation of the porphyrinoids

3.1.1 Synthesis

Scheme 3.1 shows the synthetic pathway of free base porphyrinoids **1** and **2** and Sn(IV) complexes **1-Sn** and **2-Sn**. **1** is a *meso*-4-methylthiophenylporphyrin, while **2** is its corrole analogue. The porphyrin has been reported previously and was synthesised by following the well-established Adler-Longo method [24,136]. This involves a one-pot acid-catalyzed condensation of pyrrole and the appropriate aldehyde. The target compound was isolated in *ca.* 38% yield from the crude mixture by column chromatography on silica gel.

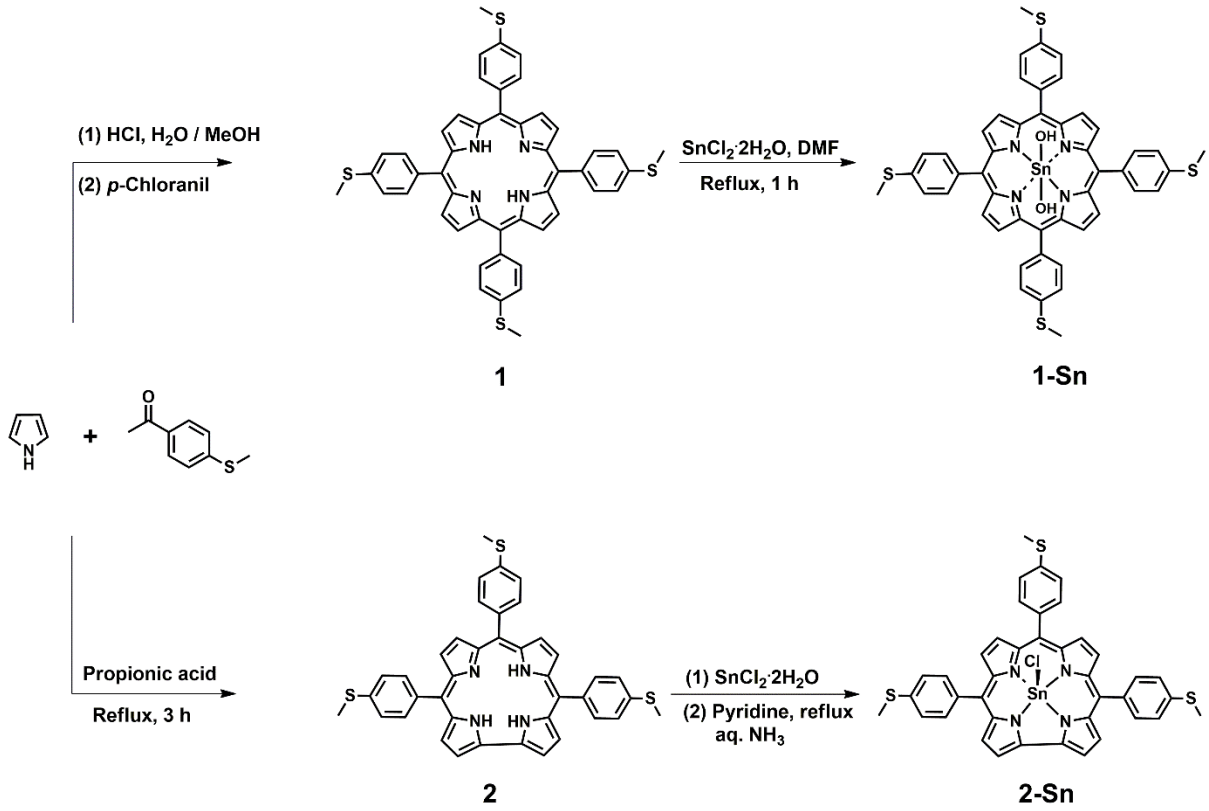

Scheme 3.1. The synthetic routes for the free base compounds **1** and **2** and Sn(IV) complexes **1-Sn** and **2-Sn**.

1-Sn was prepared by refluxing of **1** in pyridine with excess $SnCl_2 \cdot 2H_2O$. The treatment of the reaction vessel with 37% aqueous ammonia afforded the crude Sn(IV) porphyrin with two hydroxy axial ligands. Subsequent purification led to **1-Sn** in relatively high yields. Free base corrole **2** was synthesised using the optimised conditions reported by Gryko's group [48] and was purified through column chromatography. The refluxing of **2** in DMF with an excess of $SnCl_2 \cdot 2H_2O$ led to the insertion of the Sn(IV) ion into the central cavity of **2**. Upon work-up of the crude and column chromatographic separation, the Sn(IV) complex **2-Sn** was obtained as green crystals.

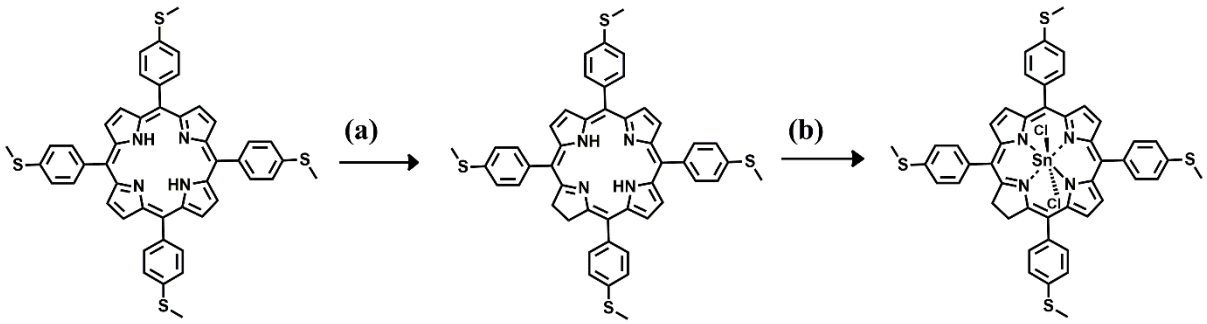

1 **3** **3-Sn**

Scheme 3.2. Synthesis of chlorin **3** and **3-Sn**. Reagents and reaction conditions: (a) i. *p*-toluenesulfonyl hydrazide, K_2CO_3, pyridine, reflux, 12 h; ii. DDQ, ethyl acetate/water, reflux, 1 h. (b) $SnCl_2 \cdot 2H_2O$, MeOH/$CHCl_3$ (1:1), reflux, 16 h.

Free base chlorin **3** was synthesised using Whitlock's diimide reduction [56] of the porphyrin starting material, **1**. This is achieved by using *p*-toluenesulfonylhydrazine with pyridine and potassium carbonate as the solvent/base system (**Scheme 3.2**). The crude product was purified through column chromatography to afford purple crystals of **3**. Refluxing **3** with excess $SnCl_2 \cdot 2H_2O$ in $CHCl_3$ and MeOH (1:1) for 16 h and subsequent purification provided **3-Sn** in relatively high yield.

N-confused porphyrin **4** was prepared *via* Lindsey's method [71] (**Scheme 3.3)** and purified by column chromatography. The corresponding Sn(IV) complex was

prepared through a 5 min reflux of **4** in pyridine with excess $SnCl_2 \cdot 2H_2O$ under a nitrogen atmosphere. The crude product was precipitated from pyridine using cyclohexane and washed with the same solvent. Subsequent workup with aqueous HCl afforded green crystals of **4-Sn**.

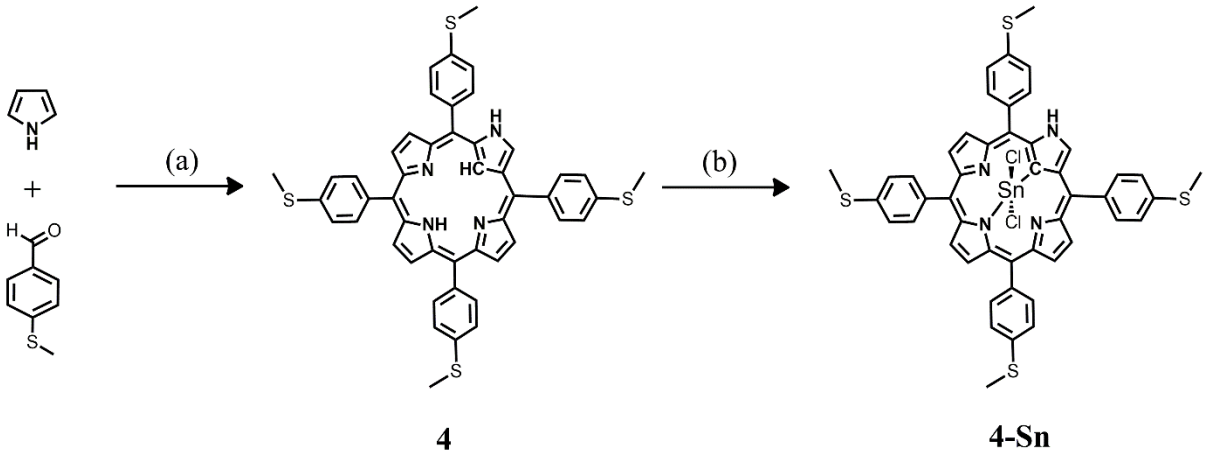

Scheme 3.3. Synthesis of N-confused porphyrin **4** and **4-Sn**. Reagents and reaction conditions: (a) i. Methanesulfonic acid, DCM, rt, 30 min; ii. DDQ, TEA, 1 min. (b) i. $SnCl_2 \cdot 2H_2O$, pyridine, reflux, 5 min; ii. aq. HCl.

3.1.2 Characterisation

The structural characterization of the compounds described in this dissertation was carried out through proton nuclear magnetic resonance spectroscopy (^{1}H NMR) and matrix-assisted laser desorption/ionization time-of-flight mass spectrometry (MALDI-TOF MS).

1 and 1-Sn. The mass of the free base porphyrin **1** was calculated to be 798.20 amu which corresponds to the experimental value of 800.02 amu based on a $[M+H]^+$ species. Similarly, the calculated mass of **1-Sn** was 950.09 amu, which is consistent with the experimental mass of 952.05 amu. The mass-to-charge (m/z) ratio of 917.05 corresponds to the loss of a Cl^- axial ligand. The ^{1}H NMR spectra of both **1** and **1-Sn**

(**Figure 3.2** (a) and (b), respectively) contains 24 protons in the aromatic region (7.5–9.5 ppm). This corresponds to the 16 protons from the phenyl rings and 8 from the β-pyrrolic positions. At lower frequency, the presence of peak(s) that integrate to 12 protons is consistent with the methyl groups.

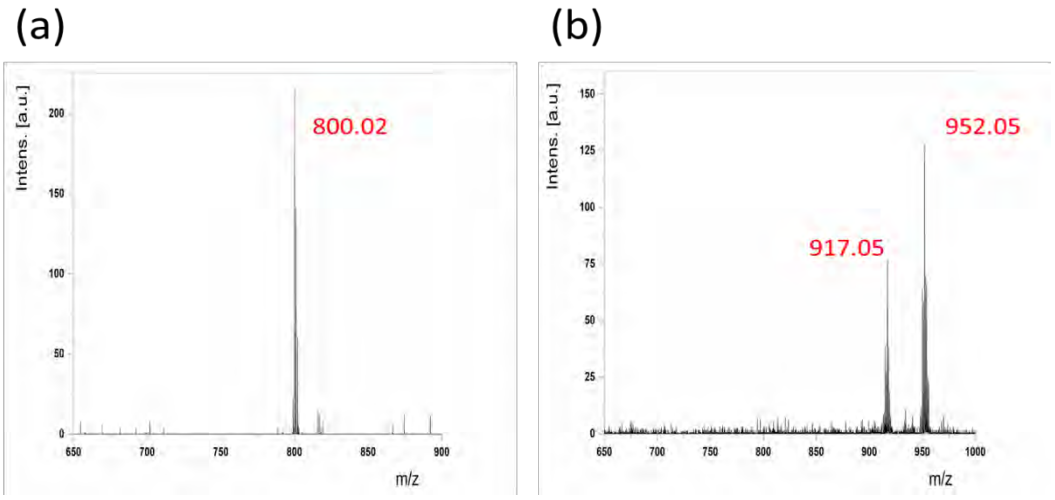

Figure 3.1. MALDI-TOF MS data for (a) **1** and (2) **1-Sn**.

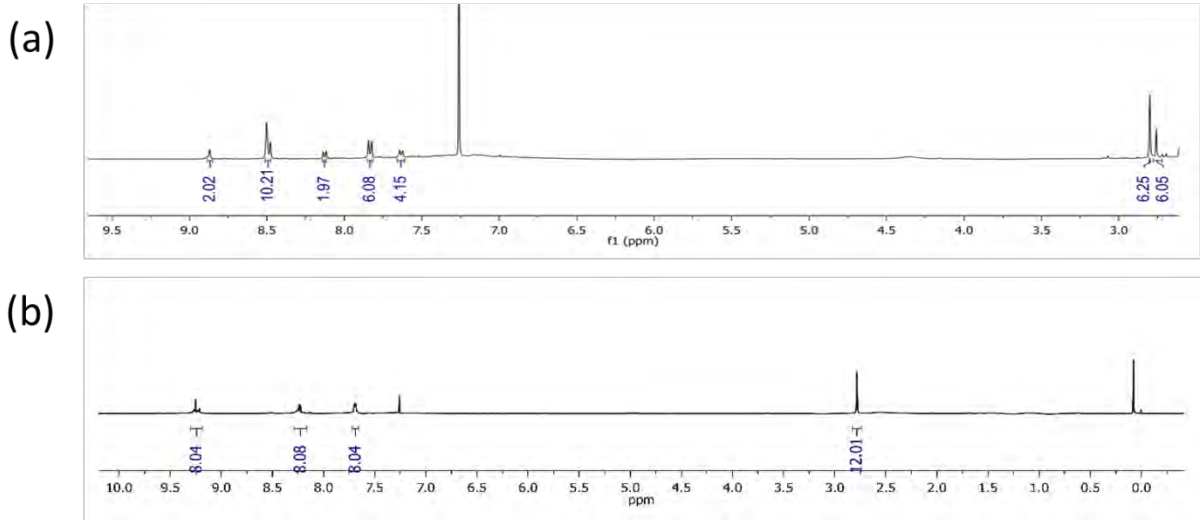

Figure 3.2. ^{1}H NMR spectra of (a) **1** and (b) **1-Sn** in $CDCl_3$.

2 and 2-Sn. As shown in **Figure 3.3**, the observed m/z ratios for both **2** and **2-Sn** are consistent with the calculated values of 664.90 and 780.59 amu. The assignment of the ^{1}H NMR spectrum of **2-Sn** (**Figure 3.4**) can be readily made based on the

presence of 8 protons corresponding to the β-pyrrolic positions of two sets of equivalent rings. In contrast with **1-Sn**, peaks integrating to only 12 protons lie in the aromatic region, since the corrole macrocycle has three *meso*-aryl rings.

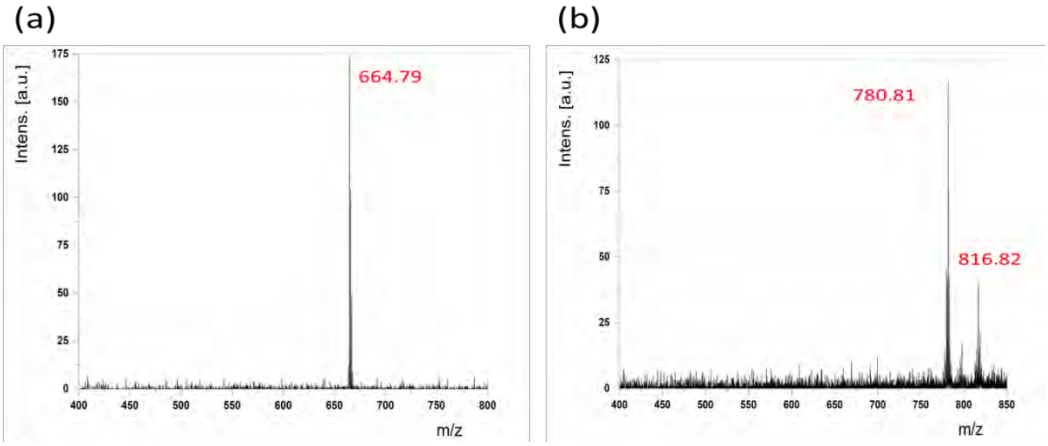

Figure 3.3. MALDI-TOF MS data for (a) **2** and (b) **2-Sn**.

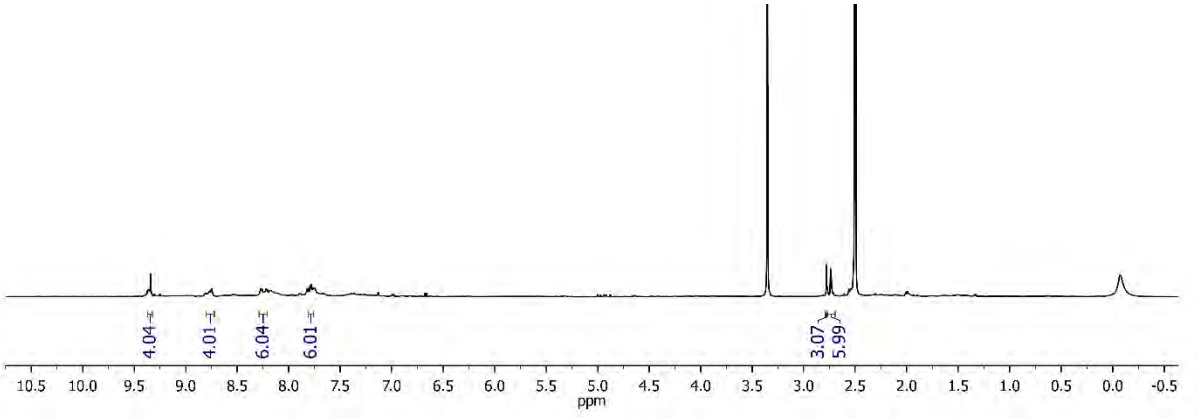

Figure 3.4. ^{1}H NMR spectrum of **2-Sn** in DMSO-d_6.

3 and 3-Sn. The ^{1}H NMR spectra of **3** and **3-Sn** can be readily assigned. In a similar manner to what is observed with **1** and **1-Sn**, the *meso*-phenyl ring peaks lie between 7.40–7.80 ppm, with the peaks integrating to a total of 16 protons. The spectra differ at the β-pyrrolic positions- due to the single reduced β- β′ double bond. A characteristic pyrroline singlet peak at *ca.* 4.2 ppm integrates to 4 protons in the spectra of both **3** and **3-Sn**. This is in close agreement with what has been reported

previously in the literature for chlorin compounds [62,137,138]. With regards to the mass spectrometry data (**Figure 3.5**), the anticipated molecular ion peaks are observed. The molecular ion peak at 1142.42 amu corresponds to the axial coordination of α-cyano-4-hydroxycinnamic acid and a Cl^- ion to the central Sn(IV) ion.

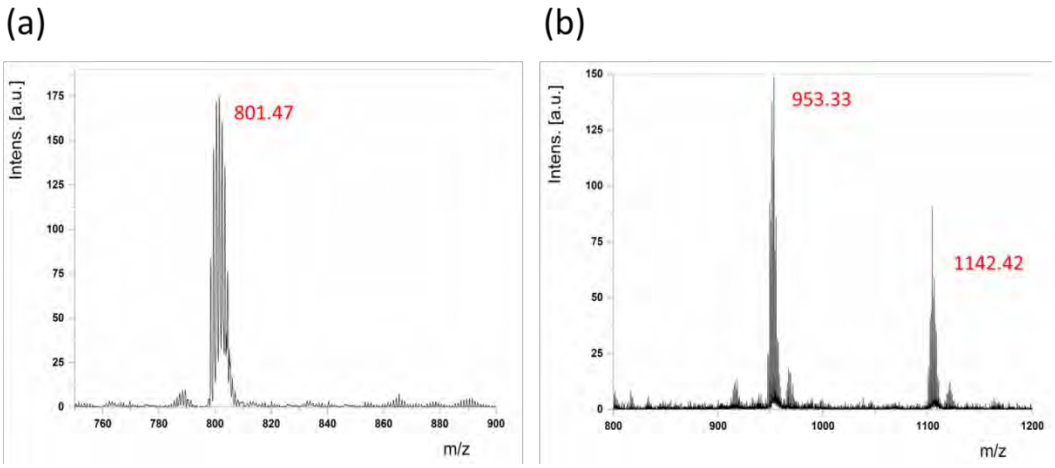

Figure 3.5. MALDI-TOF MS data for (a) **3** and (b) **3-Sn**.

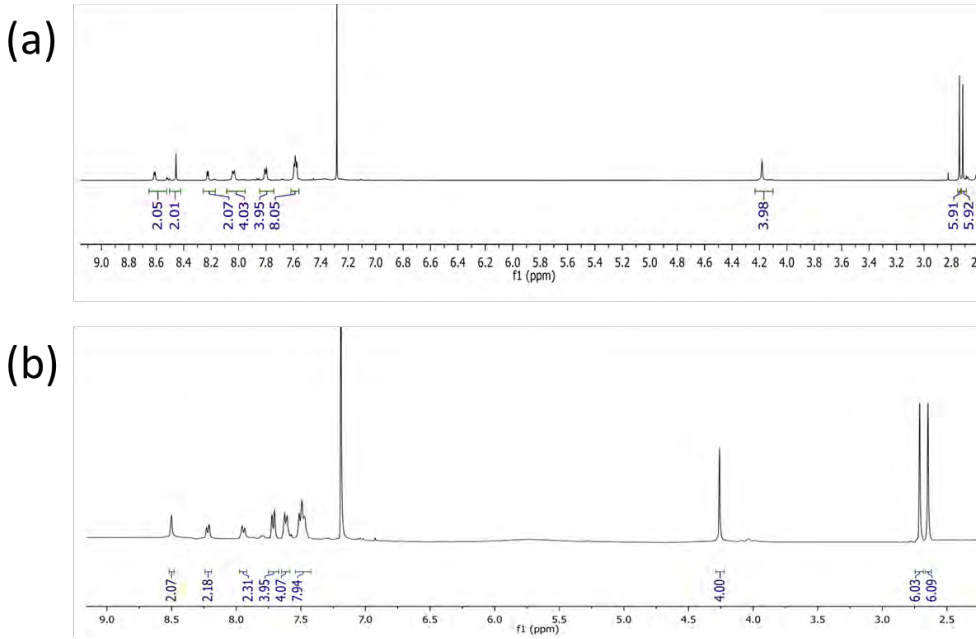

Figure 3.6. ^{1}H NMR spectra of (a) **3** and (b) **3-Sn** in $CDCl_3$.

4 and 4-Sn. The ^{1}H NMR spectrum of the N-confused porphyrin (**4-Sn**) in $CDCl_3$ is comparable to those reported previously in the literature [139,140], since the characteristic NCP peak that resonates at *ca.* 10.68 ppm is observed (**Figure 3.8**). Owing to the ring current generated by the π-macrocycle, the outer NH is deshielded to such an extent that it can lie far downfield. The peaks for the protons on the *meso*-aryl groups also lie at similar positions to previously characterised compounds. The parent peaks of m/z = 799.34 (calcd 798.20) for **4** and m/z = 951.29 (calcd 951.25) for **4-Sn** in the MALDI-TOF MS data are fully consistent with the target structures.

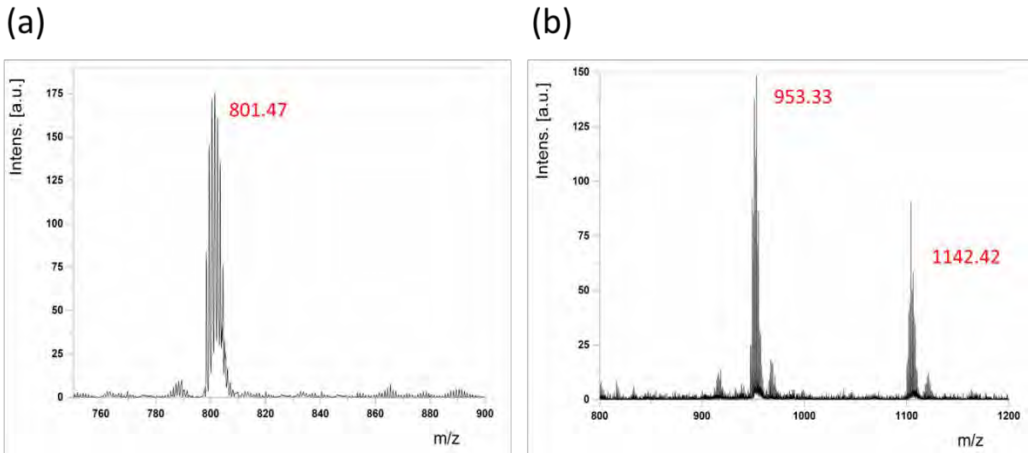

Figure 3.7. MALDI-TOF MS data for (a) **4** and (b) **4-Sn.**

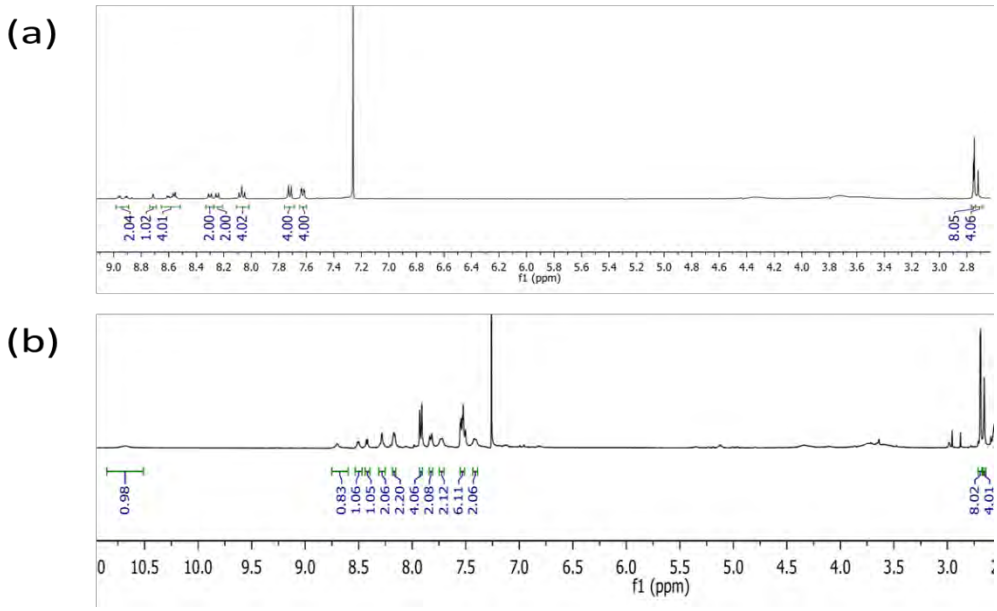

Figure 3.8. ^{1}H NMR spectra of (a) **4** and (b) **4-Sn** in $CDCl_3$.

3.2 Summary of the chapter

The syntheses of the free base porphyrin, corrole, chlorin and NCP dyes and their Sn(IV) complexes followed literature procedures. Characterizations were successfully carried out through an analysis of their ^{1}H NMR spectra and MALDI-TOF MS data.

Chapter 4

Optical spectroscopy

This chapter provides and discusses the probing of the electronic properties of the photosensitisers using optical spectroscopy.

4.1 Groundstate absorption spectroscopy

Porphyrins are recognised by their intense B (or Soret) band in the blue region of the spectrum (*ca.* 400 nm) and four relatively weak Q bands in the low energy region. Coordination of a metal to the central cavity of the porphyrin changes the molecular symmetry from D_{2h} to a full square-planar D_{4h} symmetry [78]. As a result, the four Q bands collapse into two. This holds true for **1-Sn**, as shown by the groundstate absorption spectra in **Figure 4.1**. Similarly, the corrole macrocycle displays a strong B band at *ca.* 400 nm, followed by Q bands in the visible region. As shown in **Figure 4.1**, the striking difference between corroles (**2-Sn**) and porphyrins (**1-Sn**) is the intensified absorption in the Q type band of the former. This is attributed to the lower symmetry of the corrole macrocycle.

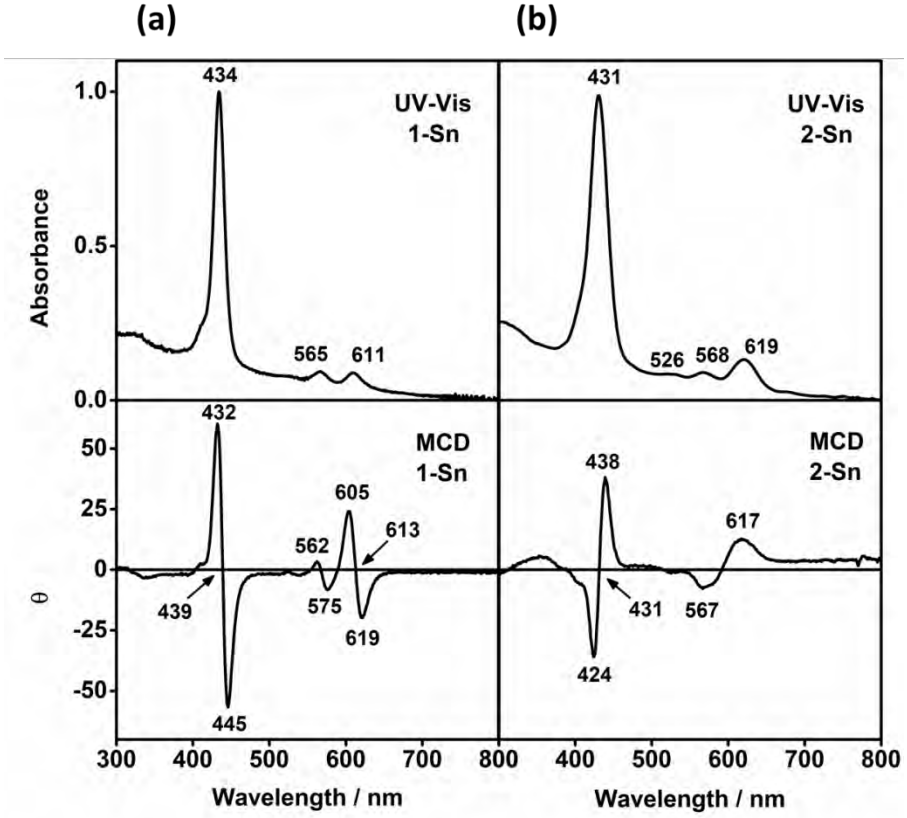

Figure 4.1. The groundstate absorption (top left) and MCD spectra (bottom left) of **(a) 1-Sn** and the groundstate absorption (top right) and MCD spectra (bottom right) of **(b) 2-Sn** in DMF.

The groundstate absorption spectrum of **3-Sn** is characteristic of Sn(IV) chlorin species such as the Sn(IV) chlorin e6 [141,142]. It can be seen (**Figure 4.2**) that due to the hydrogenation of one of the peripheral double bonds, chlorins have an intense absorption band at longer wavelengths which sets them apart from their porphyrin counterpart. In comparison to the parent isomer (a porphyrin), N-confused porphyrins possess strongly red-shifted bands with significant absorption of the Q band in the deep-red region (*ca.* 697 nm) of the spectrum.

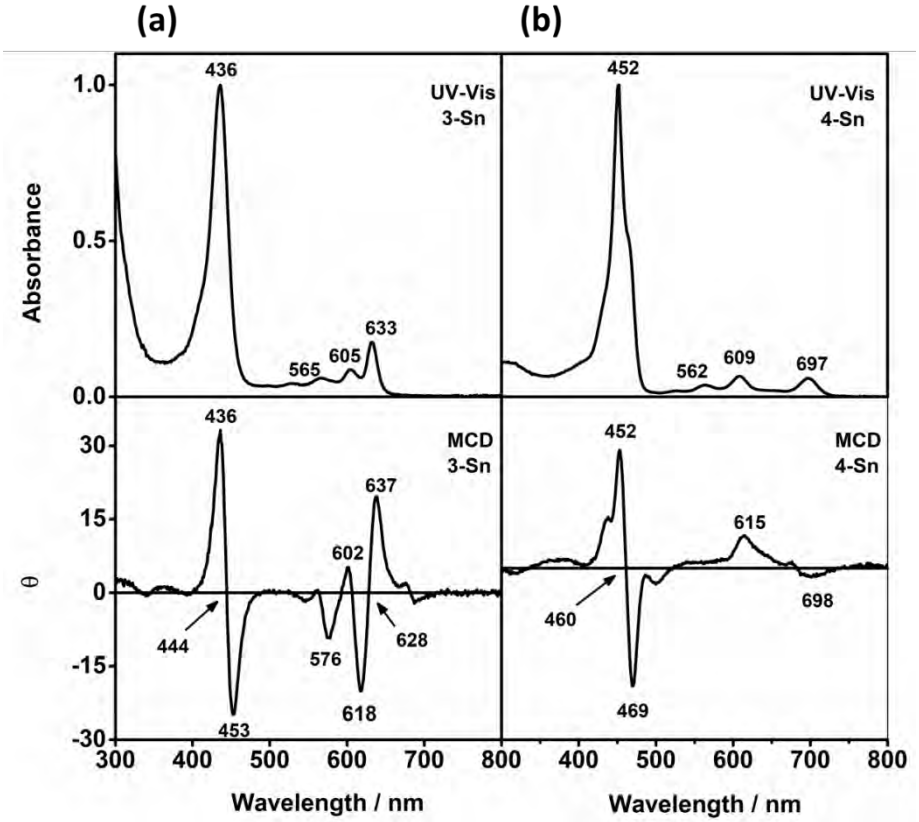

Figure 4.2. The groundstate absorption (top left) and MCD spectra (bottom left) of **(a) 3-Sn** and the groundstate absorption (top right) and MCD spectra (bottom right) of **(b) 4-Sn**.

A summary of the groundstate absorption properties of the above-mentioned compounds, together with their free base precursors, is provided in **Table 4.1** in the following subsection. The differences in the groundstate absorption spectra of these

compounds are highly noteworthy, so a theoretical calculations (Chapter 8) section detailing the role of symmetry in this context has also been provided.

Table 4.1. The optical absorption and emission data for all the compounds in DMF.

	λ_{max} (nm) (log ε)	λ_{em} (nm)
1	426 (4.60), 517 (3.70), 552 (3.59), 591 (3.45), 651 (3.36)	660, 726
1-Sn	434 (4.60), 565 (3.64), 611 (3.63)	624, 674
2	431 (4.72), 534 (3.78), 595 (3.72), 647 (4.13)	665, 724
2-Sn	431 (4.74), 526 (3.41), 568 (3.54), 619 (3.97)	638, 697
3	423 (5.40), 523 (4.25), 551 (4.21), 618 (4.23), 653 (4.51)	659, 722
3-Sn	436 (5.03), 565 (3.68), 605 (3.97), 633 (4.16)	656, 717
4	335 (4.41), 450 (5.01), 601 (3.75), 648 (3.86), 700 (3.91)	716, 770
4-Sn	452 (4.93), 562 (3.71), 609 (3.75), 697 (3.87), 781 (4.14)	711

4.2 Fluorescence spectroscopy

In general, porphyrinoid compounds such as porphyrins and corroles are inherently fluorescent. Following excitation at the Soret band maxima of **1-Sn** and **2-Sn** (or **1** and **2**), a two band emission profile is observed. The fluorescence emission maxima for the Sn(IV) complexes **1-Sn** and **2-Sn** lie at 624 and 638 nm, respectively. As shown in **Figures 4.3** and **4.4**, upon the introduction of the Sn(IV) ion into the central cavity of **1** and **2**, significant fluorescence quenching is observed. This is attributed to the heavy atom effect imparted by the Sn(IV) ion [2,13,143].

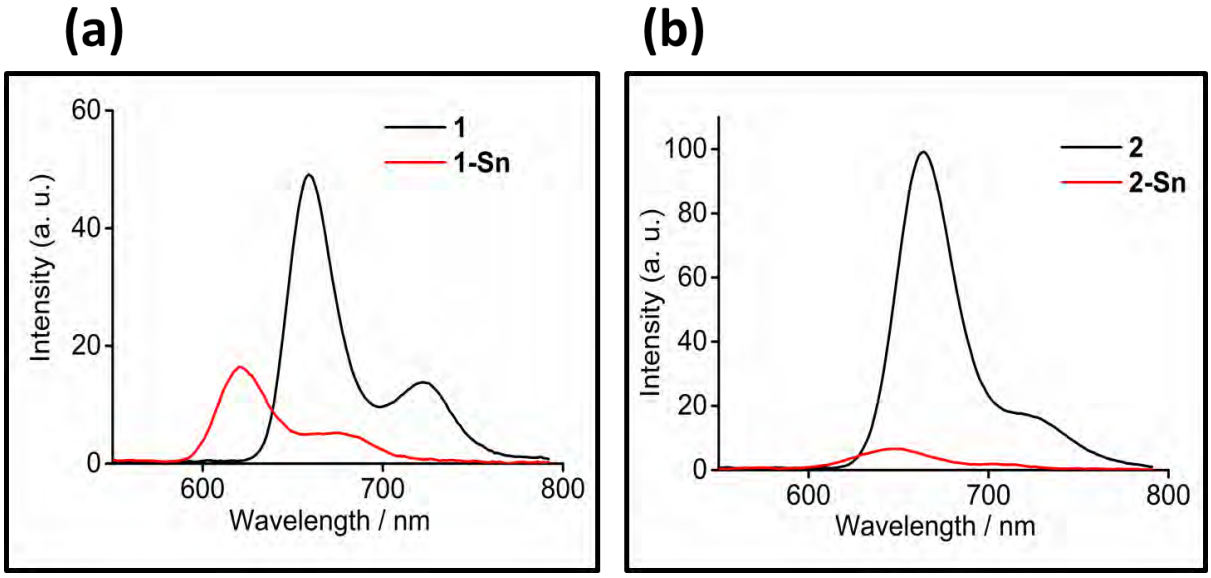

Figure 4.3. The fluorescence emission spectra of (a) **1** and **1-Sn** and (b) **2** and **2-Sn**.

In a similar manner, significant fluorescence quenching is observed in the Sn(IV) complexes of the chlorin and N-confused porphyrin. The striking characteristic of the N-confused porphyrin isomer (**4**) is the considerable decrease in fluorescence and red shift of the emission bands (*ca.* 711 nm) with respect to **1**.

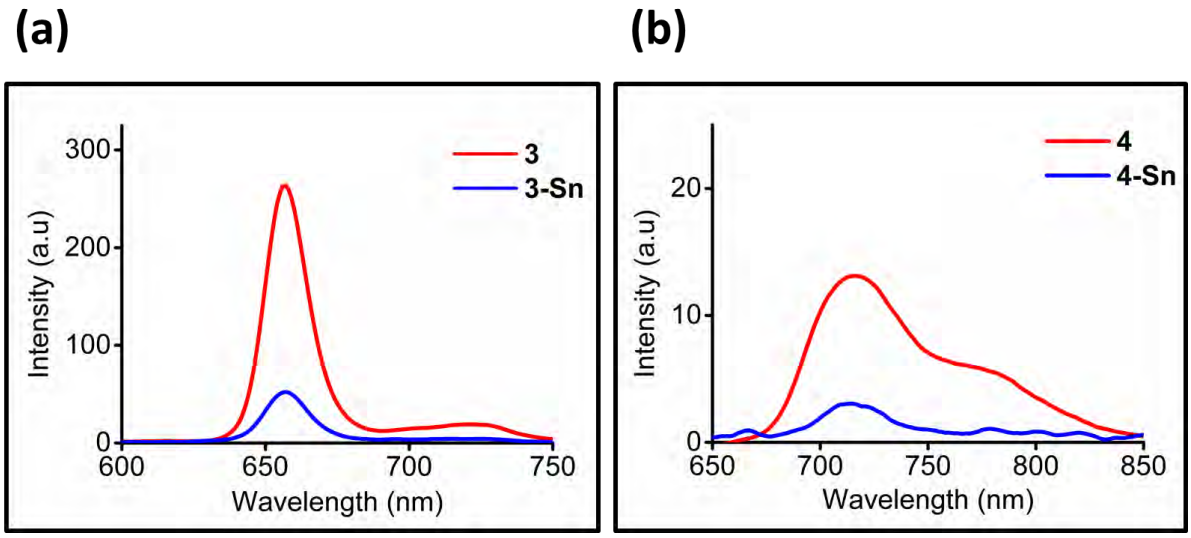

Figure 4.4. The fluorescence emission spectra of (a) **3** and **3-Sn** and (b) **4** and **4-Sn**.

4.3 Magnetic circular dichroism (MCD)

The MCD and groundstate absorption spectra of the Sn(IV) complexes (**1-Sn**, **2-Sn**, **3-Sn** and **4-Sn**) are provided in **Figures 4.1** and **4.2**. Magnetic circular dichroism (MCD) is a useful technique for probing perturbations in the π-system, revealing interesting electronic properties, particularly the excited and groundstate states of porphyrinoids in a way that cannot be achieved with groundstate absorption spectroscopy. In this regard, MCD spectroscopy is dominated by three band morphologies: the Faraday A_1 term, which arises from transitions into an orbitally degenerate excited state, the B_0 term for transitions into nondegenerate excited states and the temperature dependant C_0 term for transitions from an orbitally degenerate groundstate [144–146].

In the case of the metal porphyrin **1-Sn**, both the Q and B bands are positive Faraday A_1 terms with a sign pattern that changes from negative to positive in ascending energy (**Figure 4.1(a)**). This confirms that ΔHOMO > ΔLUMO, as would be expected since the porphyrin LUMO is a doubly degenerate e_g MO (**Figure 1.5**). In contrast with the spectrum of **1-Sn**, the MCD spectrum of **2-Sn** contains a pair of oppositely signed Faraday B_0 terms at 617 and 567 nm, **Figure 4.1(b)**. This is in agreement with the report by Kobayashi and co-workers [147] that in reduced symmetry porphyrinoid systems such as corroles, coupled pairs of oppositely signed Faraday B_0 terms replace the A_1 terms normally observed in the MCD spectra of high-symmetry metal porphyrins. Additionally, the MCD +ve/-ve sign sequence in increasing energy indicates that ΔHOMO < ΔLUMO for the metal corrole (**2-Sn**).

The **3-Sn** and **4-Sn** complexes shown in Figure 4.2 are expected to have no Faraday A_1 terms in their MCD spectra due to the lack of a three-fold or higher rotational symmetry. The Soret band region of **3-Sn** has a coupled pair of Faraday B_0 term

centred at 444 nm that form a derivative-shaped signal. The low energy Q band region of **3-Sn** is comprised of B_0 terms with positive and negative amplitudes at 637 and 618 nm, respectively. Again, the +ve/-ve sign sequence of the B_0 terms (in increasing energy) indicates that ΔHOMO < ΔLUMO for the metal chlorin complex [146]. The MCD spectrum of Sn(IV) N-confused porphyrin **4-Sn** shows that the sign pattern is typical of normal porphyrins where ΔHOMO > ΔLUMO. However, it should be emphasised that with regards to MCD spectra for NCPs, other structural changes are known to readily modify the sign sequences observed in the MCD spectra. This partly rests on whether the external NH is protonated or not. For example, it has been recently reported that Ni(II) N-confused porphyrin (NiNCP) and the corresponding methylated variant ($NiNCP^{Me}$) have a ΔHOMO < ΔLUMO relationship based on the MCD sign pattern [148,149]. However, the relationship could be reversed such that ΔHOMO > ΔLUMO by simple deprotonation of the external NH, while this could not be achieved with the N-methylated variant.

4.4 Summary of chapter

The optical properties of the photosensitisers were assessed using groundstate and fluorescence spectroscopy and magnetic circular dichroism. It was shown that significant changes in the four frontier orbitals arise through the lowering of the molecular symmetry. As a result, on moving from porphyrin to corrole and then to chlorin, a significant intensification bathochromic shift of the low energy Q type band was observed. Likewise, the confusion of one of the pyrrole moieties of a porphyrin affords N-confused porphyrin with markedly red-shifted Q and B bands. With the aid of MCD spectroscopy, the excited state properties of the photosensitisers were probed, revealing an interesting relationship between structure and the relative energies of the four frontier π-MOs.

Chapter 5

Photophysical and photochemical properties

The photophysical and photochemical properties of the photosensitiser dyes are investigated in-depth to analyse their suitability for singlet oxygen applications.

5.1 Fluorescence quantum yields and lifetimes

Porphyrinoid compounds such as corroles and porphyrins are fluorescent. Since these compounds are not soluble in water, the photophysical studies were carried out in a polar solvent DMF in which they are completely soluble.

The fluorescence quantum yield (Φ_F) values of the Sn(IV) complexes and their free base precursors were determined in DMF using a comparative method with ZnTPP as the standard (Φ_F = 0.033)[150, 151]. **Equation 1.1** was used to calculate the Φ_F values (**Table 5.1**). As expected, the Φ_F values of the Sn(IV) complexes are lower than that of free base compounds. This is due to the heavy atom associated with the central Sn(IV) ion [139]. To acquire time-resolved fluorescence data, time-correlated single photon counting (TCSPC) was used. The fitting of the fluorescence decay curves of the free bases gave τ_F values ranging from 2.77–8.50 ns. In contrast, the τ_F values of the Sn(IV) complexes lie in the 0.18-0.99 ns range. A typical decay curve for **3** is provided in **Figure 5.1** as an example.

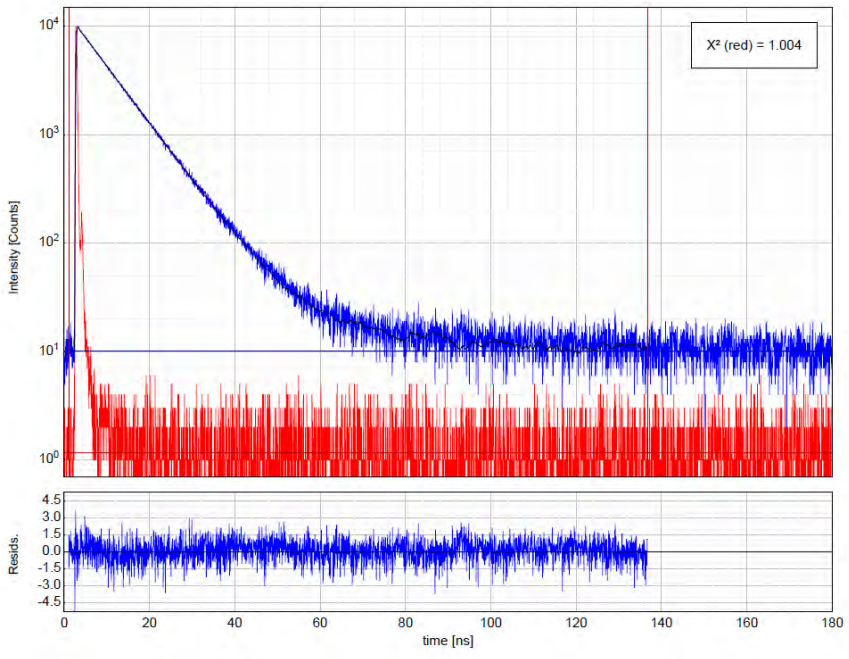

Figure 5.1. T The fluorescence decay curve (blue), reduced X^2 fitting (black), residuals (lower panel, blue) and IRF (red) for **3** in DMF.

Table 5.1. Fluorescence quantum yield and lifetime values of the Sn(IV) complexes and their free base precursors in DMF.

	Φ_F (± 0.01)	τ_F (ns)	
1	0.04	5.70	(81%)
		8.15	(13%)
1-Sn	0.02	0.47	(100%)
2	0.10	2.77	(100%)
2-Sn	< 0.01	0.18	(100%)
3	0.05	8.49	(100%)
3-Sn	0.02	0.38	(99%)
4	0.02	8.50	(85%)
		4.99	(15%)
4-Sn	< 0.01	0.27	(94%)
		0.99	(6%)

5.2 Transient absorption and triplet lifetimes

Transient absorption spectroscopy is a useful technique to probe the excited state dynamics of photosensitisers. Transient absorption spectra and triplet state decay curves were measured for the compounds studied in DMF in laser flash photolysis experiments with 7 ns laser pulses. The transient absorption spectrum of **3-Sn** is shown in **Figure 5.2** as an example, with the inset providing the corresponding triplet decay curve. In general, a broad band is observed in the 480−550 nm region of Sn(IV) complex spectra, which can be attributed to triplet-triplet absorption ($T_1 \rightarrow T_n$). A strong bleaching is observed in the B band region in comparison to the weak bleaching in the Q band region [152,153].

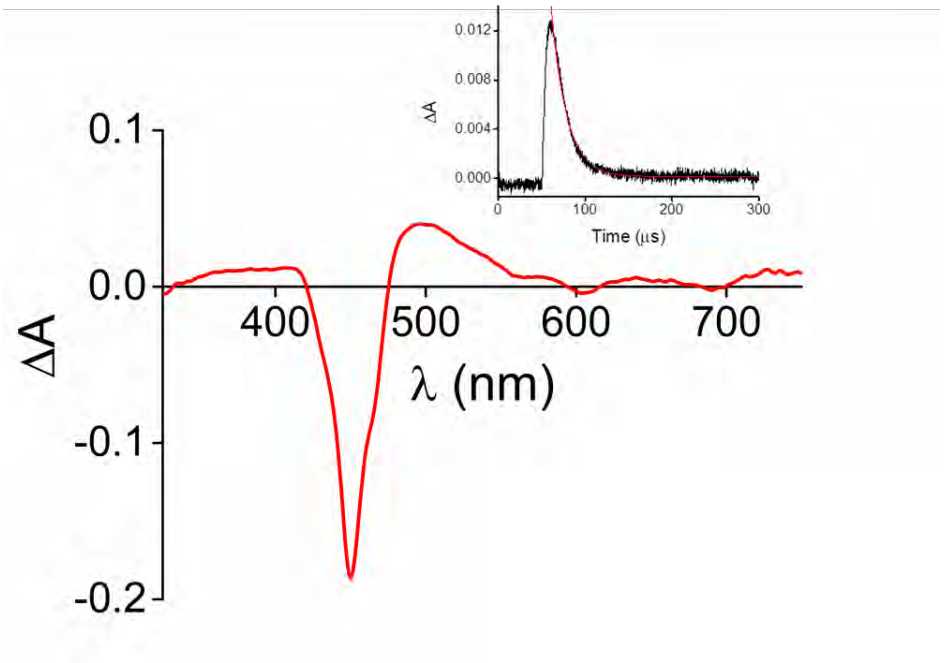

Figure 5.2. The transient absorption spectrum of **3-Sn** in DMF after excitation with a 436 nm laser source with a pulse duration of 7 ns. The inset provides the corresponding transient decay curve.

The triplet state lifetime of **2** could not be experimentally determined, which was anticipated due to the intense fluorescence that is observed for **2** [154]. Among the Sn(IV) complexes, the longest transient with a lifetime of 231 μs was obtained for corrole **2-Sn**. In general, all of the compounds have relatively long triplet state lifetimes (**Table 5.2**). This enhances their suitability for singlet oxygen applications such as PDT and PACT. The introduction of the Sn(IV) ion causes a marked increase in the τ_T values since this enhances the rigidity of the structures.

5.3 Photostability and singlet oxygen quantum yields

The photostability and singlet oxygen generation capabilities of the compounds were assessed. In this thesis, the Φ_Δ values were determined in DMF using two comparative methods. The first method relies on the integration of the area under the singlet oxygen luminescence bands (*ca.* 1270 nm) of a sample and a reference

compound (ZnTPP in DMF; Φ_Δ = 0.53) with the same optical density at the excitation wavelength [97, 99]. The Φ_Δ values of **1, 2, 1-Sn** and **2-Sn** were obtained by using this technique (**Table 2**). The other method used was a comparative method that relies on the use of singlet oxygen scavengers such as DPBF to spectroscopically determine the Φ_Δ value of an unknown compound relative to a standard which in this case was ZnTPP in DMF [97]. The Φ_Δ values of compounds **3**, **4**, **3-Sn**, and **4-Sn** were determined in this manner. The photodegradation of DPBF in the presence of **4-Sn** is shown in **Figure 5.3**, and the Φ_Δ values of the compounds are provided in **Table 5.2**.

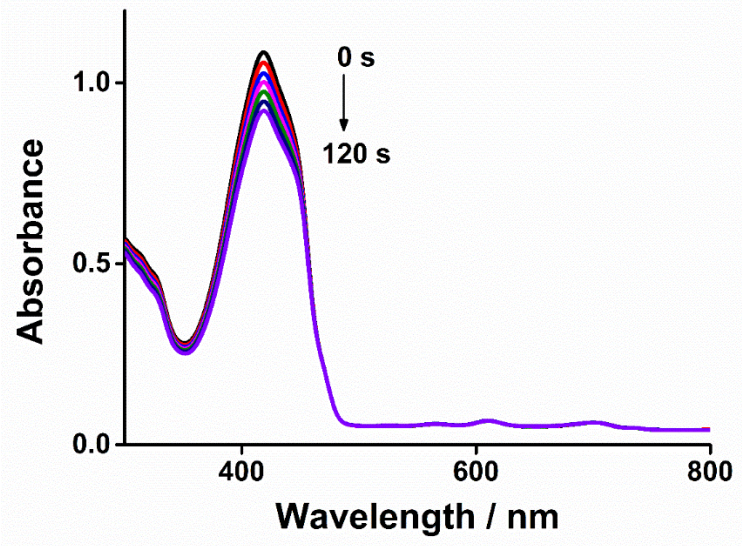

Figure 5.3. The photodegradation of DPBF in the presence of complex **4-Sn** in DMF at 20 s intervals upon excitation with monochromatic laser light.

Table 5.2. The singlet oxygen quantum yields, triplet state lifetimes and photostability of the compounds in DMF.

	Φ_Δ	τ_T (μs)	Photostability (%) [a]
1	0.51	14	83
1-Sn	0.59	214	92
2	0.14	---	84
2-Sn	0.60	231	66
3	0.40	9.0	83
3-Sn	0.48	18	78
4	0.28	13	97
4-Sn	0.88	27	93

[a] Change in absorbance at the B band maximum after photoirradiation for 30 min.

When a comparison is made of the Φ_Δ values, it becomes clear that there is a marked increase in the Φ_Δ values of the Sn(IV) complexes in comparison to the free base compounds (**Table 5.2**). The heavy Sn(IV) central ion causes a large perturbation in the spin-orbit coupling that translates to an increased rate of intersystem crossing (ISC) due to the heavy atom effect. Relative to the other compounds in the study, the N-confused complex (**4-Sn**) had a significantly higher Φ_Δ value. In contrast, the free base corrole **2** and 3-C substituted NCP had relatively low Φ_Δ values of 0.14. The low value for **2** is not surprising due to the high fluorescence quantum yield (**Table 5.1**) [152].

Photosensitiser dyes are prone to degradation by singlet oxygen formed upon photoexcitation, so it is important to assess the degree of photodegradation that occurs under the conditions used for PDT and PACT activity experiments. Photoirradiation of **1, 1-Sn, 2** and **2-Sn** with a Thorlabs 625 nm LED (432 J cm^{-2}) mounted in the housing of a Modulight medical laser for 30 min (in 15 min intervals) demonstrated that **1, 1-Sn** and **2** are moderately photostable. However, when absorbance at the B band maximum of the **2-Sn** corrole complex was monitored, the intensity decreased to 66% after 30 min. Although chlorins are known to be relatively unstable [50], only 17 and 22% photobleaching of the **3** and **3-**Sn B bands was observed during exposure in a similar manner to a 660 nm LED for 30 min (280 $mW.cm^{-2}$). In contrast, N-confused porphyrin **4** and **4-Sn** exhibit a high level of photostability in this context, with photobleaching of only 7% observed for **4-Sn**.

5.4 Summary of Chapter

The photophysicochemical properties of the series of photosensitiser dyes prepared in Chapter 3 were analysed, so that trends in the properties can be identified and the suitability of the dyes for singlet oxygen applications assessed. As

anticipated, superior singlet oxygen generation properties were obtained for the Sn(IV) complexes due to the heavy atom effect. All the compounds are moderately to highly photostable under conditions used for PDT activity studies with Φ_Δ values ranging from 0.48−0.60 for **1-Sn**, **2-Sn** and **3-Sn**. It is noteworthy that an unusually high Φ_Δ value of 0.88 was obtained for the N-confused porphyrin complex **4-Sn**. This complex was also found to be highly photostable under the conditions used for PDT activity experiments. On the basis of the favourable singlet oxygen generation and relative stability demonstrated by the dyes, *in vitro* PACT and PDT studies were undertaken.

Chapter 6

Antimicrobial photodynamic therapy

This chapter discusses the photoinactivation of *S. aureus* and *E. coli* by the Sn(IV) chlorin and N-confused porphyrin complexes.

6.1 PACT studies on *S. aureus* and *E. coli*

With the intention of treating infections that affect the skin and soft tissue layers, PACT studies were performed in the deep-red region of the spectrum (Thorlabs 660 nm LED) to afford enhanced penetration in the therapeutic window [155,156]. **3**, **4**, **3-Sn** and **4-Sn** were employed in the photoinactivation of the Gram-(+) bacteria *S. aureus.* Optimisation studies of the photosensitiser concentration were performed on *S. aureus* for 75 min irradiation time, as shown in **Figure 6.1**. The control (C) demonstrates that the presence of 1% DMSO in PBS has no effect on the bacterial cells. Due to the greater activity of **3-Sn** at low concentrations compared to **4-Sn**, which is most active from 2.5 μM, 2.5 μM was used as the optimal concentration for further studies on *Staphylococcus aureus*. Similarly, concentration dependant optimisation studies were performed using the same set of compounds on the Gram-(-) bacteria, *E. coli*. On this basis, a concentration of 10 μM was determined to be appropriate for further studies.

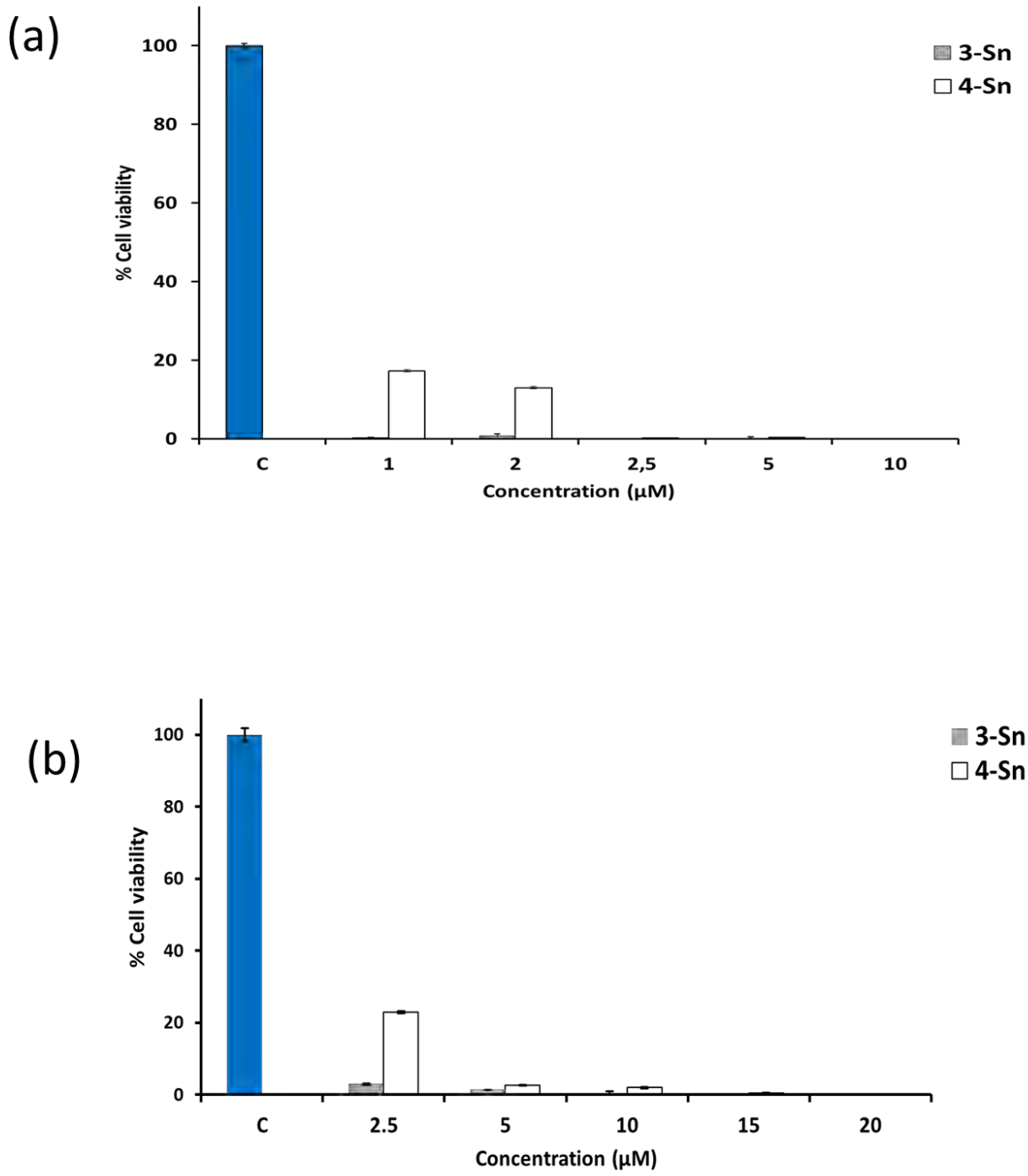

Figure 6.1. The effect of **3-Sn** and **4-Sn** in 1% DMSO/PBS on (a) *S. aureus* and (b) *E. coli* after 75 min of photoirradiation.

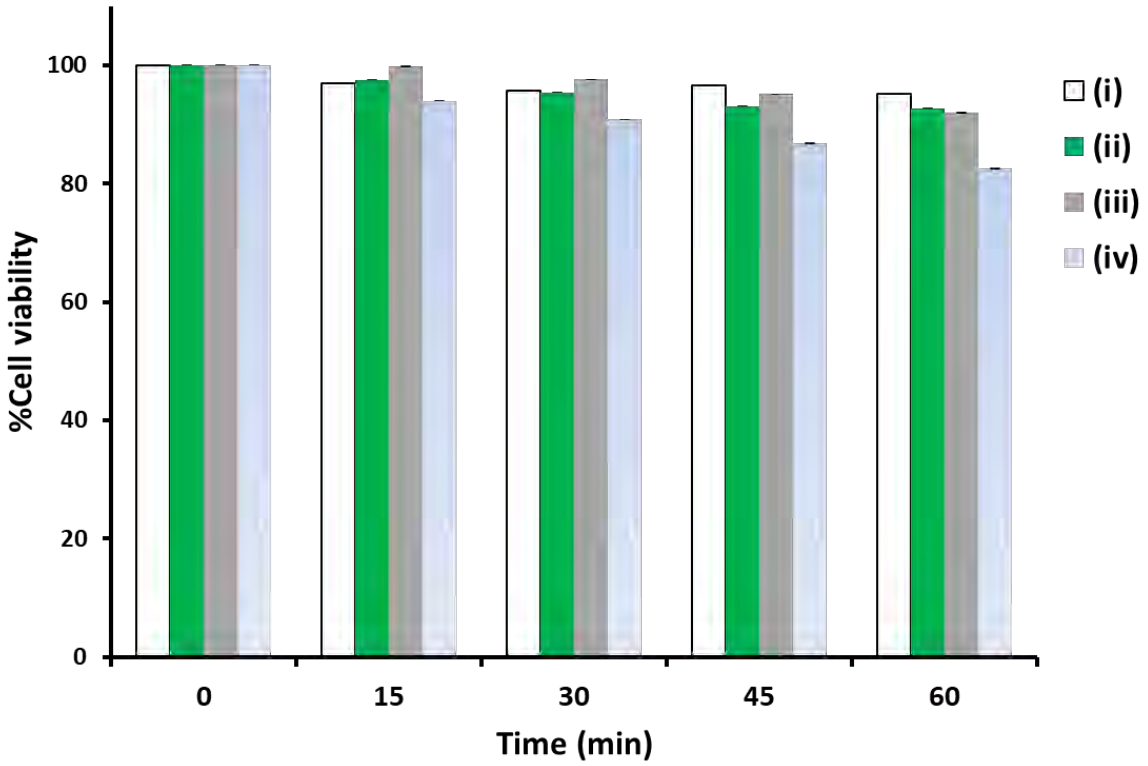

Figure 6.2. The bacterial viability after treatment of the cells with photosensitiser and being kept in the dark for 60 min. (i) and (iii) provide the data for *S. aureus* after treatment with **4-Sn** and **3-Sn**, respectively. (iii) and (iv) provide the data for *E. coli* cells after treatment with **4-Sn** and **3-Sn**, respectively.

A 3-$\log_{10}$ reduction in the CFU/mL value of the bacteria is defined as the optimal antimicrobial effect [157,158]. Dark cytotoxicity studies reveal that both **3-Sn** and **4-Sn** exhibit minor dark toxicity. **Figure 6.2** demonstrates that **3-Sn** is significantly more cytotoxic in the dark towards *E.* coli. The log reduction values for **3-Sn** and **4-Sn** in the dark towards *E. coli* were 0.082 and 0.042, respectively, after 60 min, while the equivalent values for *S. aureus* were 0.041 and 0.032. In contrast, in the presence of 660 nm light, there is a marked decrease in the viability of both *E. coli* and *S. aureus,* as shown in **Figure 6.3**.

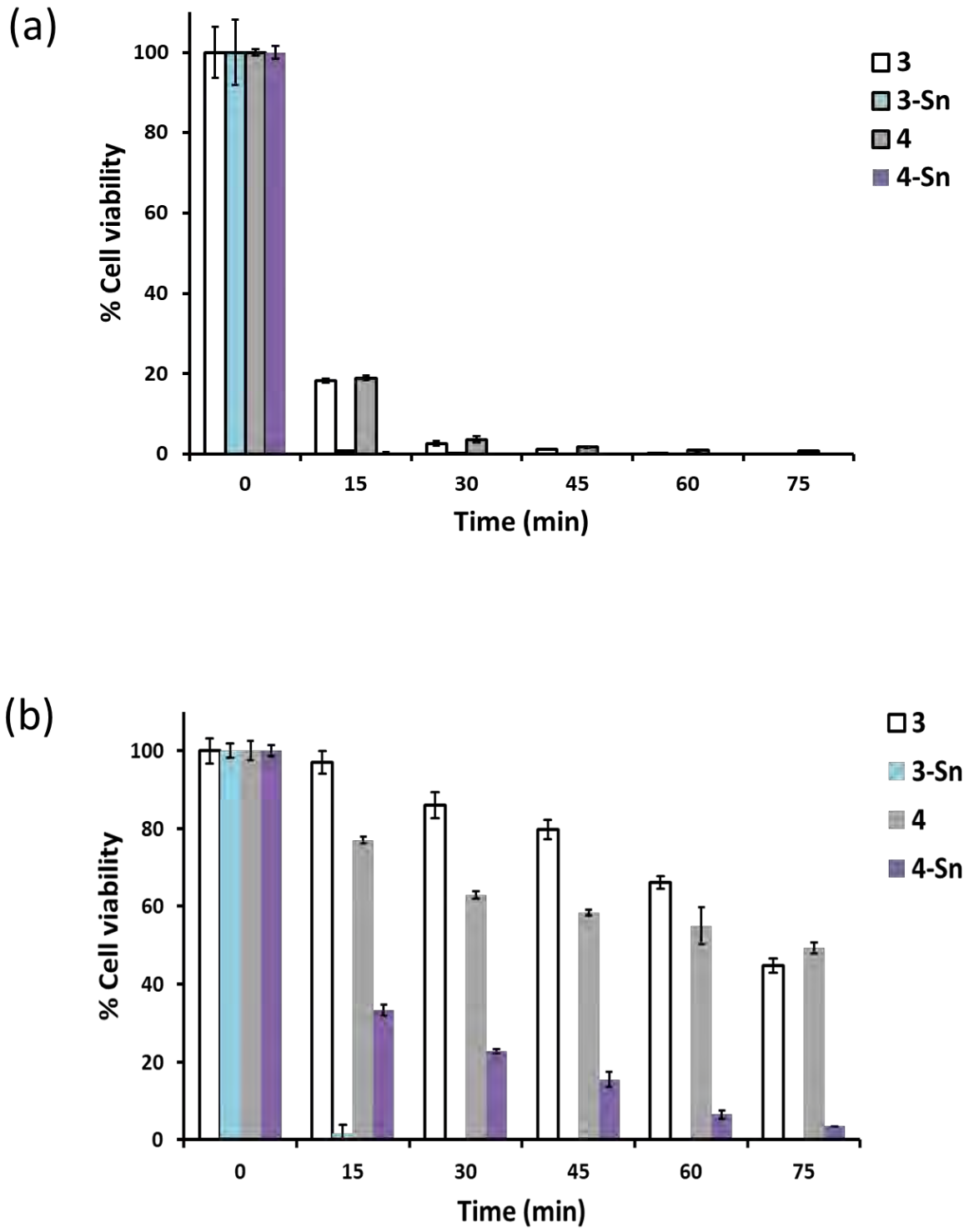

Figure 6.3. The effect of **3**, **3-Sn**, **4** and **4-Sn** on the growth of (a) *S. aureus* and (b) *E. coli* where the concentrations of compounds used were 2.5 and 10 μM, respectively. The cells before light irradiation were used as the control. All irradiations were performed under 660 nm Thorlabs LED irradiation for 75 min at 15 min intervals (280 mW.cm^{-2}).

Overall, according to the data sets provided in **Figure 6.3**, it can be concluded that **3-Sn** and **4-Sn** performed significantly better than their free base precursors after 75 min irradiation. Since singlet oxygen is usually the main cytotoxic agent in this context, the Sn(IV) complexes would be anticipated produce more singlet oxygen than their free base counterparts due to the heavy atom effect [159]. It has been reported that neutral photosensitisers are not as effective in inactivating Gram-(-) species, such as *E. coli,* than is the case with Gram-(+) bacteria such as *S. aureus* [160,161]. This is supported by the high log reduction values for the compounds in *S. aureus* compared to *E. coli* (**Table 6.1**). It is noteworthy that chlorin species such as **3-Sn** towards the inactivation of Gram-(-) species (8.74 log reductions) with an irradiance of 280 mW.cm^{-2} for 75 min. Park *et al.* examined chlorin e6 (**Ce6**) mediated PACT against *S. aureus*, *E. coli* and other bacterial strains. Notably, the authors described that **Ce6** was highly active towards *S. aureus,* but this was not the case with *E. coli* [162]. In contrast, another similar study at the INI (Rhodes University, South Africa) reported high $\log_{10}$ reductions in the CFU/mL values for *E. coli* after 60 min light irradiation [163]. This was attributed to the presence of thien-2-yl *meso*-rings. In connection with their findings, we report that **3-Sn** also exhibits unusually high photocytotoxicity towards *E. coli* in a similar manner.

Table 6.1. Log reduction values upon irradiation of *S. aureus* and *E. coli* with a 660 nm Thorlabs LED (280 mW.cm^{-2}) for 75 min. Photosensitiser concentrations of 2.5 and 10 μM were used for *S. aureus* and *E. coli*, respectively.

	Log reduction	
	E. coli	*S. aureus*
3	0.35	10.6
3-Sn	8.74	10.5
4	0.30	2.1
4-Sn	1.57	10.5

In contrast, the combination of the N-confused porphyrin **4-Sn** and a 660 nm LED (280 mW.cm^{-2}) for 75 min results in a log reduction of 1.57 in *E. coli*. The singlet oxygen quantum yield of **4-Sn** was determined to be 0.88 (**Table 5.2**) compared to a value of 0.48 for **3-Sn**. Although singlet oxygen is understood to be the main cytotoxic agent, it appears that factors such as localisation into target cellular structures are as important as singlet oxygen generation [126].

6.2 Summary of chapter

This chapter dealt with *in vitro* antimicrobial photodynamic therapy experiments mediated by the Sn(IV) complexes of a chlorin and N-confused porphyrin, **3-Sn** and **4-Sn**, respectively. The free base precursors were also assessed. Clinically, antimicrobial compounds require a 3 $\log_{10}$ reduction in CFU/mL to be considered favourable candidates for this application. With that in mind, in the context of PACT, the photosensitisers under study exhibited minimal dark cytotoxicity (< 1 $\log_{10}$ reduction) against both *S. aureus* and *E. coli* bacterial strains. In combination with a Thorlabs 660 nm LED, significant photocytotoxicity effects were observed against both bacterial strains. Gram-(+) bacterial strains are known to be more sensitive to neutral photosensitisers compared to Gram-(-) strains. The ability of **3-Sn** to decrease the CFU/mL value of *E. coli* by an 8.74-$\log_{10}$ reduction suggests that factors other than singlet oxygen may be responsible. This merits further in-depth investigation.

Chapter 7

Photodynamic therapy

This chapter described the *in vitro* dark toxicity and photocytotoxicity properties of the photosensitisers against MCF-7 adenocarcinoma cells.

7.1 PDT activity of Sn(IV) complexes 1-Sn and 2-Sn against MCF-7 cells

To assess the influence of the structural difference between Sn(IV) complexes of *meso* 4-methylthiophenyl functionalised porphyrin, corrole, chlorin and N-confused porphyrin macrocycles (**Scheme 3.1** and **Scheme 3.2**) on photodynamic activity, *in vitro* cytotoxicity studies on MCF-7 human adenocarcinoma cells were carried out.

Prior to the *in vitro* evaluation of the PDT activity of Sn(IV) porphyrin and corrole complexes **1-Sn** and **2-Sn** were examined for their cellular uptake into MCF-7 cells after 12, 24 and 48 h of incubation. **Figure 7.1** shows the enhanced fluorescence intensity of the cells treated with Sn(IV) complexes relative to untreated (control) cells. The cellular uptake increased for both complexes from 12 to 24 h and then decreased at 48 h. This shows that the uptake of **1-Sn** and **2-Sn** by the MCF-7 cells is at its maximum at *ca.* 24 h, so a pre-incubation period of 24 h was chosen for the cytotoxicity studies.

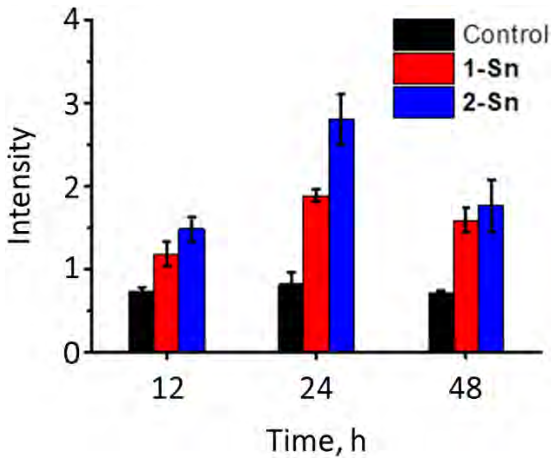

Figure 7.1. The time-dependent cellular uptake of **1-Sn** and **2-Sn** by MCF-7 cells measured by fluorescence intensity counts using excitation and emission wavelengths of 430 and 630 nm, respectively.

The cytotoxicity and photocytotoxicity of free bases **1** and **2** and the corresponding Sn(IV) complexes **1-Sn** and **2-Sn** were studied against MCF-7 cells over the

concentration range of 0.78–50 μM (**Figure 7.2**). The MCF-7 cells were incubated in the dark for 24 h with different concentrations of **1**, **2**, **1-Sn** and **2-Sn**. The cells were then irradiated with a 625 nm Thorlabs LED for 30 min (240 mW.cm^{-2}). The irradiated cells were post-incubated for a further 20 h in the dark. Similarly, non-irradiated cells treated with the compounds were studied in parallel to provide a control experiment. The cytotoxicity of the compounds was determined using the MTT assay [134]. **Figure 7.2a** shows that over the concentration range that was studied, **1-Sn** and **2-Sn** are non-toxic in the dark with IC_{50} values > 50 μM. Upon photoirradiation, **1-Sn** and **2-Sn** showed enhanced photocytotoxicity with IC_{50} values of 12.4 and 8.9 μM, respectively. The values are tabulated in **Table 7.1**.

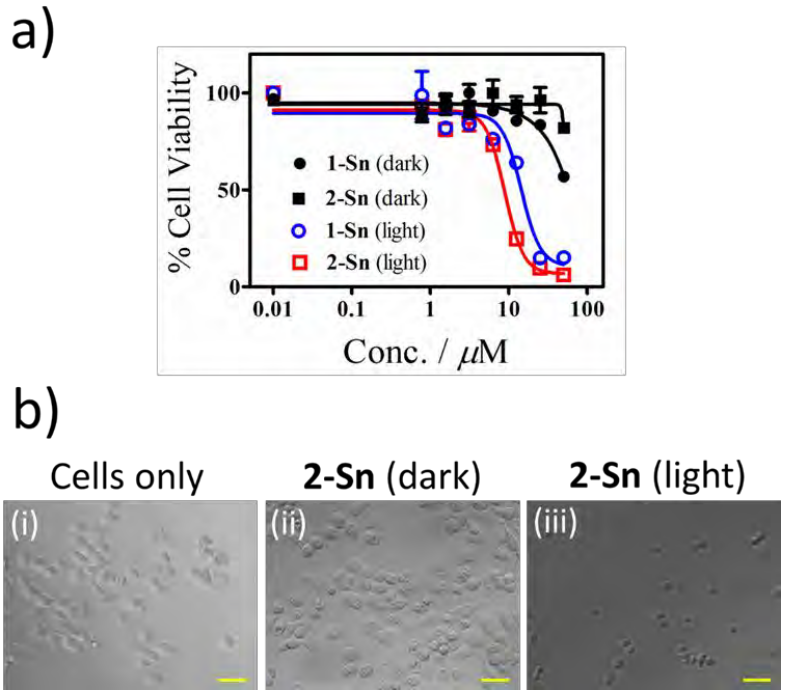

Figure 7.2. Cytotoxicity of **1-Sn** and **2-Sn** in MCF-7 cells after 24 h incubation in the dark (black bars), followed by photoirradiation with a Thorlabs 625 nm LED for 30 min (240 mW.cm^{-2}) (red and blue bars). (b) Morphological changes observed through phase-contrast microscopy of MCF-7 cells: (i) control cells, (ii) **2-Sn** (10 μM) treated cells in the dark, (iii) **2-Sn** (10 μM) treated cells after photoirradiation with a 625 nm LED for 30 min. [Scale bar: 200 μm].

To observe the effect of the photosensitiser on cell morphology, MCF-7 cells were treated with **2-Sn** (10 μM) and inverted microscopy images were taken after 30 min of photoirradiation. As shown in **Figure 7.2b**, the control cells and non-irradiated cells treated with **2-Sn** complexes remain healthy with well-defined cell morphology. However, in light-treated cells, cell shrinkage and an almost spherical shape with reduced cell density are observed. This provides a clear demonstration that Sn(IV) complex treated MCF-7 cells induce cytotoxicity upon irradiation with light [164, 165].

Since **1-Sn** and **2-Sn** have similar singlet oxygen quantum yields (**Table 5.2**), the enhanced photocytotoxicity of Sn(IV) corrole **2-Sn** is most likely due to the higher apparent cellular uptake (**Figure 7.1**) and greater molar absorptivity at *ca.* 625 nm (**Figure 4.1b** and **Table 4.1**).

7.2 PDT activity of the Sn(IV) complexes 3-Sn and 4-Sn against MCF-7 cells

The PDT activity properties of chlorin derivatives **3** and **3-Sn**, N-confused porphyrins **4** and **4-Sn** have been studied over the concentration range of 0.8–50 μM against the MCF-7 adenocarcinoma cell line in the presence and absence of light by using the MTT assay.

The cytotoxic studies revealed that all the compounds were effectively nontoxic in the absence of exposure to light with IC_{50} values > 50 μM. However, upon exposure to a 660 nm LED, high cytotoxicity was observed. Free base chlorin (**3**) and the corresponding Sn(IV) complex **3-Sn** had IC_{50} values of 7.8 and 3.9 μM, respectively. The heavy metal effect related to the Sn(IV) ion of **3-Sn** results in a two-fold decrease in the IC_{50} value compared to **3**. It is noteworthy that this photosensitiser performs

substantially better than its porphyrin (**1-Sn**) and corrole (**2-Sn**) analogues, **Table 7.1**.

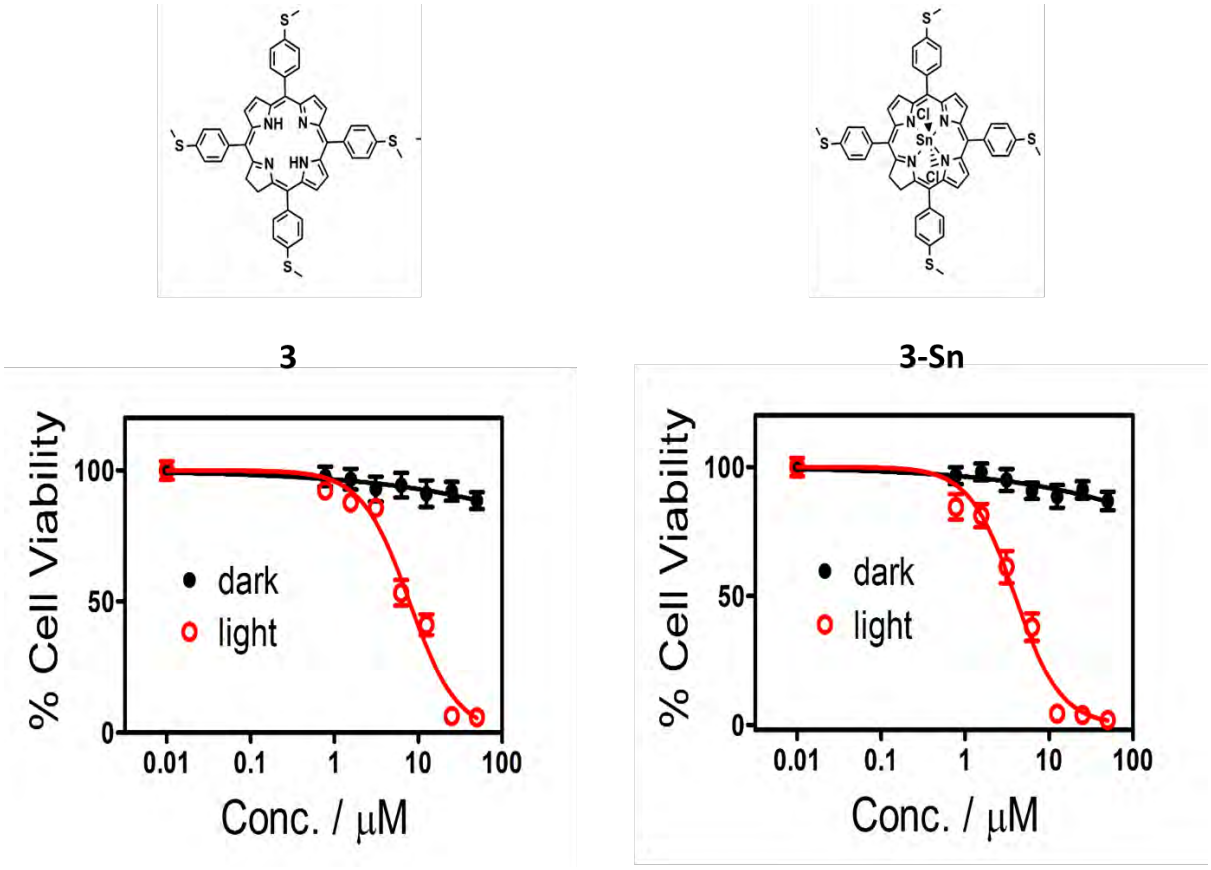

Figure 7.3. Cytotoxicity of **3** and **3-Sn** in MCF-7 cells after 24 h incubation in the dark (solid black circle), followed by photoirradiation with a Thorlabs 660 nm LED for 30 min (280 mW.cm^{-2}) (hollow red circle).

The free base N-confused porphyrin (**4**) had an IC_{50} value of 27.9 μM. This is comparable to the 12 μM for *meso*-tetrakis(*p*-sulfonatophenyl)N-Confused porphyrin tetrasodium salt reported by Thomas *et al.* [165], which had a two-fold lower IC_{50} value perhaps due to the sulfonation, which is known to improve membrane permeability [167, 168]. In a similar manner to chlorin compounds **3** and **3-Sn**, insertion of a Sn(IV) ion into the central cavity of **4** affords **4-Sn**, which results in a twenty-fold decrease in the IC_{50} value. This can also be attributed to the heavy atom effect.

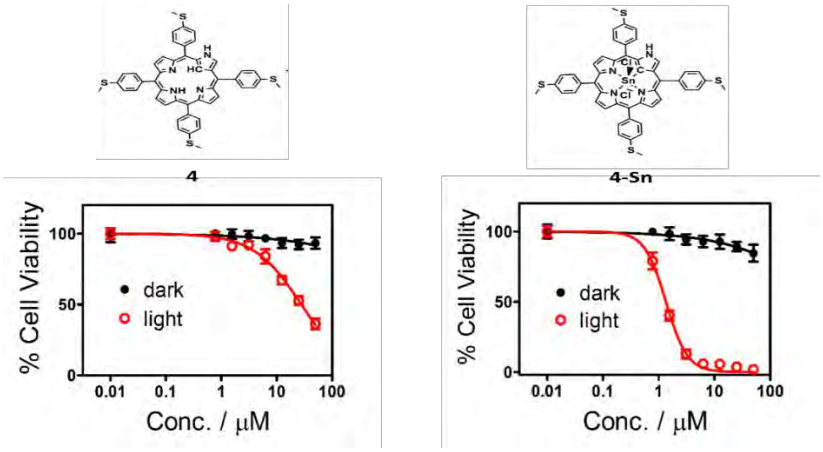

Figure 7.4. Cytotoxicity of **4** and **4-Sn** in MCF-7 cells after 24 h incubation in the dark (solid black circle), followed by photoirradiation with a Thorlabs 660 nm LED for 30 min (280 mW.cm^{-2}) (hollow red circle).

Table 7.1. The IC_{50} values of all the photosensitisers studied in this thesis (TOP) and related values from the literature (BOTTOM) against MCF-7 cells.

	IC_{50} (μM) Dark[a]	**IC_{50} (μM) Light[b]**
1	> 50	> 50
1-Sn	> 50	12.4 (± 1.2)
2-Sn	> 50	8.9 (± 0.6)
3-Sn	> 50	3.9 (± 0.9)
4-Sn	> 50	1.4 (± 0.8)
	IC_{50} (μM) Dark[a]	**IC_{50} (μM) Light**
(3-pyridyloxy)$_2$ Sn(IV) tetraphenylporphyrin	> 50	18.7 (± 1.1)[c]
(3-pyridyloxy)$_2$ Sn(IV) tetrathien-2-ylporphyrin	> 50	5.6 (± 1.1)[c]
Sn(IV) trithien-2-ylcorrole	> 50	3.2 (± 0.1)[d]
Sn(IV) triphenylcorrole	> 50	13.1 (± 0.2)[d]
Tetrathien-2-ylchlorin	> 25	3.5 (± 1.1)[e]
Tetra-5-bromothien-2-ylchlorin	> 25	2.7 (± 1.0)[e]
Tetraphenylchlorin	> 25	15.8 (± 1.2)[e]
Sn(IV) Tetrathien-2-ylchlorin	> 25	0.9 (± 0.1)[f]
Sn(IV) N-confused tetraphenylporphyrin	> 25	1.6 (± 0.2)[g]

[a] For 24 h incubation in the dark; [b] For 24 h incubation in the dark followed by exposure to a 625 or 660 nm Thorlabs M625L3 and M660L3 LEDs (240 mW.cm^{-2} or 280 mW.cm^{-2}) for 30 min; [c] 24 h incubation in the dark followed by exposure to a Thorlabs M625L3 LED (240 mW cm^{-2}) for 20 min [169]. [d] 24 h incubation in the dark followed by exposure to a Thorlabs M625L3 LED (240 mW cm^{-2}) for 30 min [170]. [e] 24 h incubation in the dark followed by exposure to a Thorlabs M660L3 LED (280 mW cm^{-2}) for 15 min [163]. [f] 24 h incubation in the dark followed by exposure to a Thorlabs M660L3 LED (280 mW cm^{-2}) for 30 min [172]. [g] 24 h incubation in the dark followed by exposure to a Thorlabs M660L3 LED (280 mW cm^{-2}) for 30 min [171].

Similar studies have been conducted at the Institute of Nanotechnology Innovation (Rhodes University, South Africa) on *meso*-thien-2-yl substituted dyes; Sn(IV) complexes of porphyrins, corroles, chlorins and N-confused porphyrins have also been studied in this context [163, 169–172]. In this regard, the photosensitisers had negligible dark cytotoxicities, and significant cell death was observed upon photoirradiation with IC_{50} values comparable to the photosensitisers studied in this thesis. This is summarised in **Table 7.1**.

7.3 Summary of chapter

From **Table 7.1**, it is apparent that **4-Sn** performed better than all the other Sn(IV) porphyrin derivatives. This is mostly due to its inherently high singlet oxygen quantum yield. Secondly, the compounds had minimal dark cytotoxicity, a favourable trait for photosensitisers in PDT applications. Upon exposure to light, with the notable exceptions of free bases **1, 2** and **4**, IC_{50} values < 15 μM were obtained against MCF-7 adenocarcinoma cells. It is noteworthy that 625 or 660 nm red region LED light sources can be used for Sn(IV) porphyrin derivatives with relatively straightforward syntheses that have appreciable absorbance in the red-region of the spectrum as a result of lowering the symmetry of the complexes in various ways. The *meso*-aryl rings of the dyes studied provide scope for conjugation to gold and silver nanoparticles to provide enhanced cellular uptake and retention. Further in-depth study is merited in this context.

Chapter 8

Theoretical calculations

This chapter provides a theoretical investigation into the excited state properties of the compounds reported in this thesis.

8.1 Geometry structures and TD-DFT

In accordance with Gouterman's molecular orbital theory (**Figure 1.5**), the degenerate excited singlet configurations $(a_{2u})^1(e_g)^1$ and $(a_{1u})^1(e_g)^1$ of normal porphyrins gives rise to the intense Soret band and relatively weak Q bands [173]. To establish the relationship between the structural modifications (as described in this thesis) to the porphyrin core with the bathochromic shift and intensification of the Q bands, time-dependant density functional theory (TD-DFT) calculations were carried out. The optimised geometric structures calculated by B3LYP/SDD for all the compounds are shown in **Figure 8.1**. Of interest was the observed out of plane phenyl rings owing to the steric interaction between β-pyrrole hydrogen and *meso*-phenyl groups.

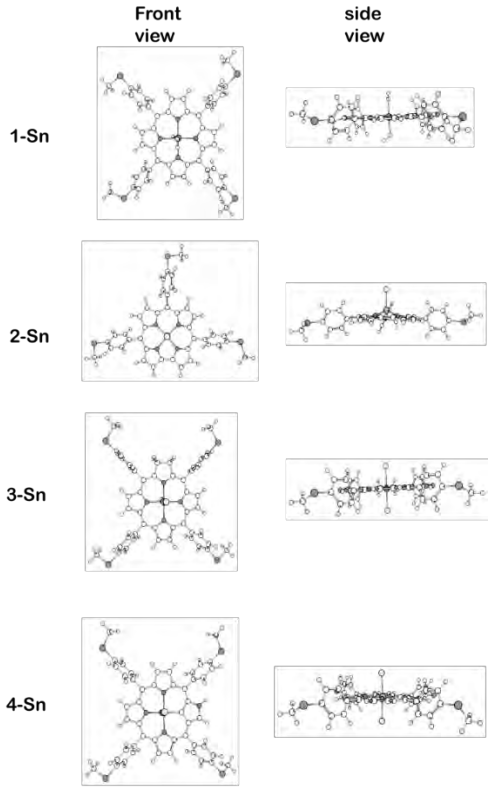

Figure 8.1. Groundstate optimised structures of Sn(IV) porphyrin derivatives at the B3LYP/SDD level of theory.

A time-dependent density functional theory (TD-DFT) treatment is provided of the optical properties of the Sn(IV) porphyrin derivatives. Calculations consisting of the 40 lowest singlet-singlet transitions at the CAM-B3LYP/SDD level were performed. The SDD basis sets account for the relativistic effects of heavy atoms such as tin and sulfur [174]. This treatment was carried out to gain insight into the effect of the structural modifications from the parent Sn(IV) porphyrin complex (**1-Sn**) to the lower symmetry analogues/isomer (**2-Sn**, **3-Sn** and **4-Sn**).

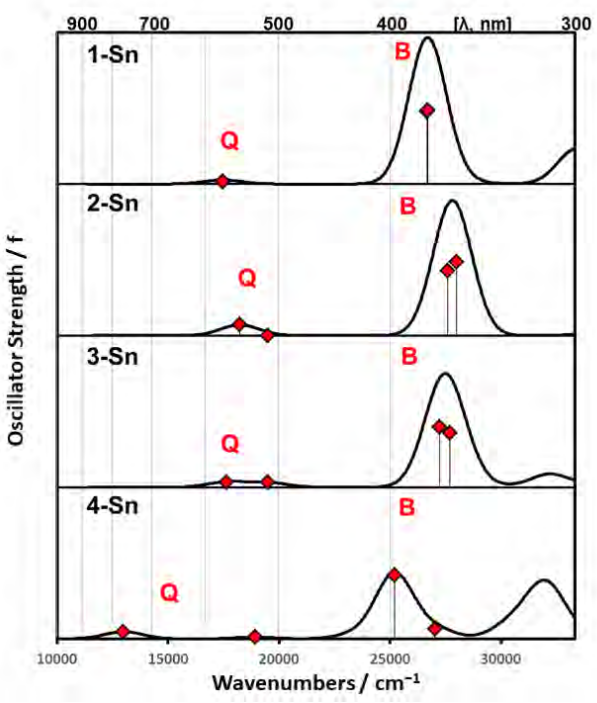

Figure 8.2. The calculated TD-DFT absorption spectra (*in vacuo*) of **1-Sn**, **2-Sn**, **3-Sn** and **4-Sn** at the CAM-B3LYP/SDD level of theory. The simulated spectra were generated using Chemcraft software with a fixed half-bandwidth taken as 2000 cm^{-1}. Only the oscillator strength values of the Q and B bands have been included for clarity.

Figure 8.2 shows the simulated TD-DFT spectra of the tin(IV) complexes (**1-Sn**, **2-Sn**, **3-Sn** and **4-Sn**). The major spectral bands in the UV-visible absorption spectra of porphyrinoids can be readily assigned by using Gouterman's four-orbital model

[77,78,101,175]. The model describes the M_L = 0, ±1, ±2, ±3, ±4, ±5, ±6, ±7, 8 angular nodal patterns in the MOs of the parent $C_{16}H_{16}^{2-}$ cyclic polyene. The parent structure becomes perturbed by the introduction of four pyrrole nitrogen atoms into the structure such that a four-fold symmetry is adopted. There is a degenerate $1e_g$ LUMO with M_L= ±5 angular nodal patterns while MOs derived from the HOMO of the parent hydrocarbon perimeter (a_{1u} and a_{2u}) have M_L = ±4 angular nodal properties. This gives rise to allowed B transitions (ΔM_L = ±1) and forbidden Q transitions (ΔM_L = ±9).

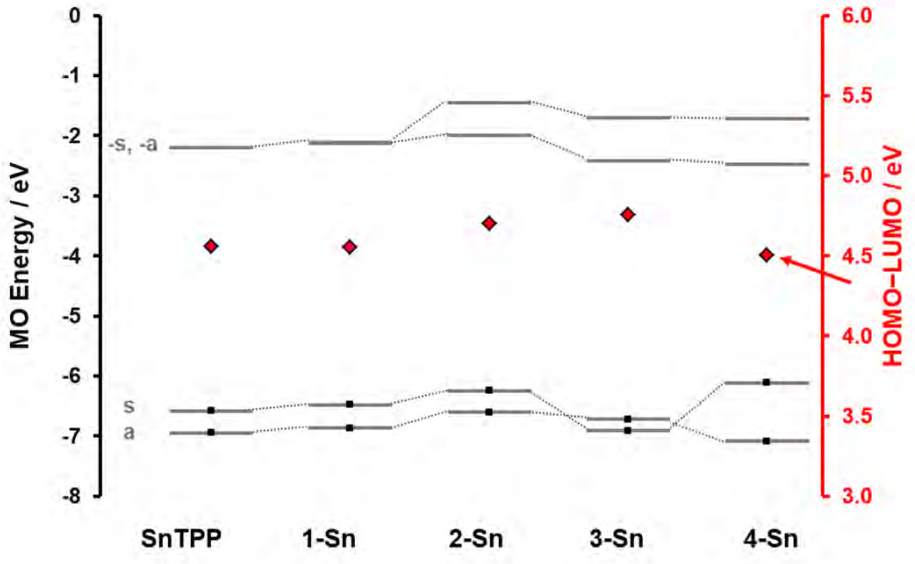

Figure 8.3. The relative energies of the four frontier molecular orbitals for the Sn(IV) complexes **1-Sn**, **2-Sn**, **3-Sn** and **4-Sn** together with the model tetraphenylporphyrin (TPP) complex with Sn(IV) at the core. Red diamonds represent HOMO-LUMO energy gap values against a secondary axis.

When a comparison of the experimental groundstate absorption spectra of the Sn(IV) complexes is made, key trends can be discerned. This includes the red-shift and intensification of the Q band when moving from the parent molecule **1-Sn** to the low-symmetry derivatives **2-Sn**, **3-Sn** and **4-Sn**. The lowering in their symmetry significantly lifts the degeneracy of **-s** and **–a** π-MOs (**Figure 8.3)**. The allowed and

forbidden properties of the B and Q transitions mix, and thus there is a marked intensification of the Q band.

In Michl's perimeter model [176–178], the four frontier π-MOs derived from the HOMO and LUMO of the parent hydrocarbon perimeter are referred to as the **a**, **s**, **−a** and **−s** MOs (**Figure 8.3**), respectively, depending on whether there is a nodal plane (**a** or **−a** MOs) or large MO coefficients (**s** or **−s** MOs) aligned with the *y*-axis. In this context, perturbations to the relative energies of the four frontier orbitals result in changes in the electronic absorption bands that can be readily rationalised across a series of porphyrinoids with different molecular symmetries.

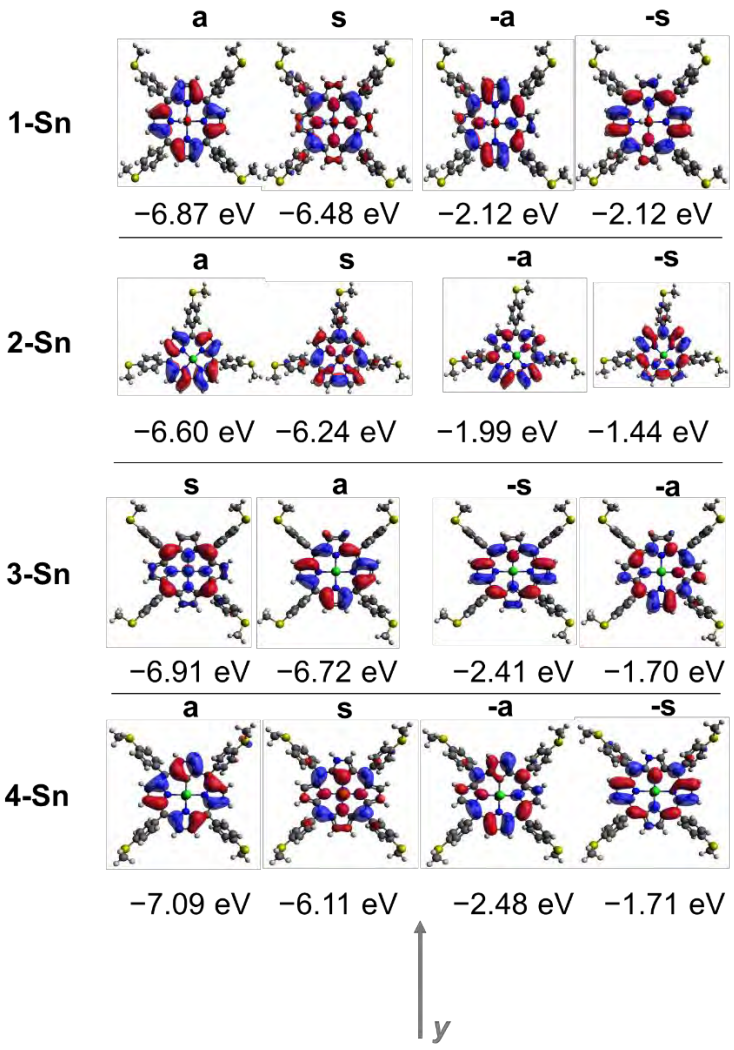

Figure 8.4. The nodal patterns of the **a**, **s**, **-a** and **–s** π-MOs of **1-Sn**, **2-Sn**, **3-Sn** and **4-Sn**.

Table 8.1. The TD-DFT spectra of B3LYP/SDD optimised structures of **SnTPP**, **1-Sn**, **2-Sn**, **3-Sn** and **4-Sn** calculated at the CAM-B3LYP/SDD level of theory.

SnTPP

Band[a]	#[b]	Exp[c]	Calc[d]	Wave Function[e]
	1		573 (0.03)	**63% s → -s; 36% a →-a;** …
Q	2	611	573 (0.03)	**63% s → -a; 37% s → -a;** …
	3		375 (1.23)	**61% a → -a; 32% s →-s;** …
B	4	434	375 (1.23)	**61% a → -s; 32% s → -a;** …

1-Sn

Band[a]	#[b]	Exp[c]	Calc[d]	Wave Function[e]
	1		573 (0.04)	**36% s → -a; 27% s →-s; 20% a → -s; 16% a → -a;** …
Q	2	611	572 (0.04)	**36% s → -s; 27% s → -a; 20% a → -a; 15% a→ -s;** …
	3		375 (1.43)	**46% a → -a; 26% s →-s; 15% a → -s; 8% s → -a;** …
B	4	434	374 (1.46)	**47% a → -s; 26% s → -a; 15% a → -a; 8% s → -s;** …

2-Sn

Band[a]	#[b]	Exp[c]	Calc[d]	Wave Function[e]
Q_x	1	619	549 (0.21)	**75% s → -a; 24% a → -s;** …
Q_y	2	526	513 (0.00)	**59% a → -a; 39% s → -s;** …
	3		362 (1.29)	**60% s → -s; 38% a →-a;** …
B	4	431	357 (1.45)	**73% a → -a; 23% s → -a;** …

3-Sn

Band[a]	#[b]	Exp[c]	Calc[d]	Wave Function[e]
Q_x	1	633	588 (0.06)	**68% a → -s; 32% s → -a;** …
Q_y	2	565	504 (0.08)	**67% s → -s; 31% a → -a;** …
	3		360 (1.38)	**63% s → -a; 31% a →-s;** …
B	4	436	355 (1.73)	**66% a → -a; 29% s → -s;** …

4-Sn

Band[a]	#[b]	Exp[c]	Calc[d]	Wave Function[e]
Q_x	1	697	771 (0.14)	**92% s → -a; 5% a → -s;** …
Q_y	2	562	527 (0.03)	**67% s → -s; 31% a → -s;** …
	6		397 (1.29)	**59% a → -s; 27% s →-a;** 10% H−6 → -s; …
B	8	452	370 (0.19)	**69% a → -s;** …

[a]Band assignment described in the text. [b]The number of the state assigned in terms of ascending energy within the TD-DFT calculation. [c]Experimental band wavelengths (nm). (f). [d]Theoretical energies in wavelengths (nm) and oscillator strengths in parentheses. [e]The wave functions based on the eigenvectors predicted by TD-DFT. One-electron transitions between the four frontier π-MOs of Gouterman's 4-orbital model are highlighted in bold face. H and L refer to the HOMO and LUMO, respectively. Only one-electron transition with a contribution > 10% are consistently shown.

TD-DFT calculations were also used to confirm the observed MCD sign pattern, which is the function of the arrangement of the four π-MOs. As shown in **Figure 8.3**, the energy difference between **s** and **a** (ΔHOMO) of **1-Sn** is greater than that of the degenerate LUMOs. This theoretical observation is in agreement with the negative-to-positive sign pattern in ascending energy (**Figure 4.1a**). The same observation has been made for the N-confused porphyrin **4-Sn** (**Figure 4.2b** and **Figure 8.3**). The MCD spectra of **2-Sn** and **3-Sn** (**Figures 4.1b** and **4.2a**, respectively) showed a positive-to-negative sign pattern with ascending energy. This points towards ΔHOMO being less than ΔLUMO, and indeed this was confirmed by the MO energies of the said compounds at the CAM-B3LYP/SDD level of theory (**Figure 8.3**).

8.2 Summary of the chapter

The goal of this chapter was to test the validity of the analyses of the arrangements of the π-MOs that were proposed based on magnetic circular dichroism in Chapter 4 through time-dependent density functional theory calculations. A secondary goal was to provide a theoretical explanation of the observed groundstate absorption spectra in accordance with conceptual frameworks such as Gouterman's four orbital model and Michl's perimeter model [77,78,175,176]. From a theoretical standpoint, the changes in the relative energies of the four frontier π-MOs account for why the Q bands absorbed in the therapeutic window. The TD-DFT calculations revealed that the complexes **1-Sn** and **4-Sn** had ΔHOMO > ΔLUMO while for **2-Sn** and **3-Sn** ΔHOMO < ΔLUMO. This is in agreement with observations made in Chapter 4.

Chapter 9

Conclusions and future outlook

This chapter outlines conclusive remarks based on the studies conducted. Recommendations for further studies are provided.

9.1 Conclusions

This research aimed to identify effective Sn(IV) porphyrin derivatives for biomedical applications, specifically and photodynamic therapy (PDT) and, to a lesser extent, photodynamic antimicrobial chemotherapy (PACT). In this regard, this first studied ring-contracted porphyrin derivatives- corroles. With the aim of addressing the inherently weak absorbance of porphyrins in the deep-red region of the UV-Visible spectrum, low symmetry porphyrin derivatives were explored. This included ring-contracted corroles, partially hydrogenated chlorins, and N-confused porphyrins, which possess a single inverted pyrrole ring. To enable direct comparison across the series of compounds studied, the study focussed on *meso*-4-methylthiophenyl compounds.

The Sn(IV) ion was the central atom of choice. The rationale behind this was that heavy atoms promote intersystem crossing to the triplet state and hence increase the efficiency of singlet oxygen generation. The singlet oxygen quantum yields (Φ_Δ) of the Sn(IV) complexes are enhanced with respect to their free base counterparts. Among the Sn(IV) complexes, **4-Sn** generates singlet oxygen most efficiently (Φ_Δ = 0.88 in DMF). This was followed by **2-Sn**, **1-Sn** and **3-Sn** with singlet oxygen quantum yields of 0.60, 0.59 and 0.48, respectively. As is necessary for photosensitisers for PDT applications, all of the compounds reported have relatively long-lived triplet state lifetimes. Furthermore, the presence of a Sn(IV) central ion resulted in the Sn(IV) complexes having longer triplet state lifetimes over their free-base counterparts. Exposure of the photosensitisers to the same light conditions used during *in vitro* PDT demonstrated that they are photostable. The photostability was measured as a change in absorbance of the B band as a function of light irradiation. With the exception of **2-Sn**, a value of 75% or greater was observed.

PACT studies were carried out for **3**, **4** and corresponding Sn(IV) complexes (**3-Sn** and **4-Sn**). Considerable cytotoxicity was observed upon light exposure. With the notable exception **4**, an average 10.5 $\log_{10}$ reduction in the CFU/mL of *S. aureus* was obtained after photoirradiation for 75 min. The light treatment of *E. coli* in the presence of **3**, **4** or **4-Sn** gave a $\log_{10}$ reduction less than 3 in the CFU/mL of the gram-(-) bacterial strain. The impressive photocytotoxicity of **3-Sn** ($\log_{10}$ =8.74) towards *E. coli* after 75 min of light treatment is particularly noteworthy, since neutral and anionic photosensitisers are normally only weakly effective against gram-(-) strains, such as *E. coli*, due to the structure of the cellular wall. The principal mechanism responsible for the unusual activity of **3-Sn** against *E. coli* warrants further in-depth investigation.

Negligible dark cytotoxicity was observed (IC_{50} > 50 μM) during the *in vitro* cytotoxicity studies of the compounds. Upon exposure to light, a therapeutic effect was obtained. In general, the Sn(IV) complexes performed better than the free base precursors. The best results were obtained for **4-Sn** with a half-maximal inhibitory concentration of 1.4 μM towards MCF-7 adenocarcinoma cells. This was followed by **3-Sn** (3.9 μM), **2-Sn** and **1-Sn** with IC_{50} values of 8.9 and 12.4 μM, respectively.

9.2 Future outlook

This body of work examined the use of tetrapyrrolic pigments such as porphyrins as photosensitisers in PDT. In particular, low symmetry derivatives of porphyrins. Their significant absorbance in the red or deep-red region of the spectrum led to the speculation that they might possess superior optoelectronic and tissue transmission properties relevant to the aforementioned biomedical application. *In vitro* studies

confirmed that these low symmetry porphyrin derivatives warrant further *in vivo* studies to determine their efficiency.

The future direction of this research should be pointed towards improving the photophysicochemical properties of the N-confused porphyrins. Although singlet oxygen is the primary cytotoxic agent, various other factors need to be explored to afford a strong candidate for clinical trials. The solubility of a drug plays a role in the therapeutic effect of the photosensitiser. Hence, solubilisation strategies such as micellar encapsulation and perhaps functionalisation with quaternary ammonium moieties should be explored. Additionally, conjugation of the drug with a moiety that can ensure affinity for specific tumour cells, whether actively or passively, may prove to be important.

One way of achieving this is the use of nanoparticular agents such as upconversion nanoparticles. The upconversion nanoparticles will accumulate in tumour cells and ensure deep tissue penetration is achieved as they are activated with NIR light. Then, the N-confused porphyrin will be sensitised through energy transfer processes and will produce reactive oxygen species to kill the cells.

References

1. Biel MA. *Laryngoscope* 1998; **108**: 1259-1268.
2. Allison RR, Downie GH, Cuenca R, Hu XH, Childs CJH and Sibata CH. *Photodiagnosis Photodyn. Ther.* 2004; **1**: 27-42.
3. Macdonald IJ and Dougherty TJ. *J. Porphyrins Phthalocyanines* 2008: 1-18.
4. Dabrowski JM, Arnaut LG, Pereira MM, Urbańska K, Simões S, Stochel G and Cortes L. *Free Radic. Biol. Med.* 2012; **52**: 1188-1200.
5. Zhu W, Gao YH, Liao PY, Chen DY, Sun NN, Nguyen Thi PA, Yan YJ, Wu XF and Chen ZL. *Eur. J. Med. Chem.* 2018; **160**: 146-156.
6. Krishna JVS, Mrinalini M, Prasanthkumar S and Giribabu L. *Recent Advances on Porphyrin Dyes for Dye-Sensitized Solar Cells.* Soroush M and Lau KKS (Eds.). *Dye-sensitized Solar Cells: Mathematical Modelling, and Material Design and Optimization*. Philadelphia: Elsevier Inc.; 2019. 231-284
7. Xie Y, Joshi P, Ropp M, Galipeau D, You Y and Qiao Q. A core-modified porphyrin as a sensitizer for dye-sensitized solar cells. *2008 33rd IEEE Photovoltaic Specialists Conference*, San Diego, California: IEEE; 2008
8. Griffith MJ, Sunahara K, Wagner P, Wagner K, Wallace GG, Officer DL, Furube A, Katoh R, Mori S and Mozer AJ. *Chem. Commun.* 2012; **48**: 4145-4162.
9. Brothers PJ. *J. Porphyrins Phthalocyanines* 2002; **6**: 259-267.
10. Baral ER, Kim D, Lee S, Park MH and Kim JG. *Catalysts*. 2019; **9**: 311.
11. Wang D and Groves JT. *Proc. Natl. Acad. Sci. U. S. A.* 2013; **110**: 15579-15584.
12. Arruebo M, Vilaboa N, Sáez-Gutierrez B and Lambea J, Tres A, Valladares M, Gonzáles-Fernández, A. *Cancers*. 2011 3: 3279-3330.
13. Imran M, Ramzan M, Qureshi AK, Azhar Khan M and Tariq M. *Biosensors* 2018; **8**: 1-17.
14. Huang H, Song W, Rieffel J and Lovell JF. *Front. Phys.* 2015; **3**: 1-15.

15. Choi YM, Adelzadeh L and Wu JJ. *J. Dermatolog. Treat.* 2015; **26**: 202-207.

16. Scherer H. *Ann. der Chemie und Pharm.* 1841; **40**: 1-64.

17. Thudichum JL. On Cruentine. 7, 227 (1867).

18. Fischer H and Orth H. *Die Chemie des Pyrrols*, Vol. II part 1, Akademische Verlagsgesellschaft, Leipzig, 1937.

19. Fischer H and Orth H. *Die Chemie des Pyrrols,* Vol. II part 2, Akademische Verlagsgesellschaft, Leipzig, 1940.

20. Merritt JE and Loening KL. *Pure Appl. Chem.* 1979; **51**: 2251-2304.

21. Rothemund P. *J. Am. Chem. Soc.* 1935; **57**: 2010-2011.

22. Rothemund P. *J. Am. Chem. Soc.* 1936; **58**: 625-627.

23. Rothemund P and Menotti AR. *J. Am. Chem. Soc.* 1941; **63**: 267-270.

24. Adler AD, Sklar L, Longo FR, Finarelli JD and Finarelli MG. *J. Heterocycl. Chem.* 1968; **5**: 669-678.

25. Fagadar-Cosma E, Cseh L, Badea V, Fagadar-Cosma G and Vlascici D. *Comb. Chem. High Throughput Screen.* 2007; **10**: 466-472.

26. Songca SP, Oluwafemi OS and Bamidele AT. *Free Radic. Biol. Med.* 2016; **100**: S194.

27. Boëns B, Faugeras PA, Vergnaud J, Lucas R, Teste K and Zerrouki R. *Tetrahedron* 2010; **66**: 1994-1996.

28. Calvete MJF, Dias LD, Henriques CA, Pinto SMA, Carrilho RMB and Pereira MM. *Molecules* 2017; **22**: 1-11.

29. Lindsey JS. *The synthesis of meso-substituted porphyrins.* Montanari F and Casella L (Eds.). *Metalloporphyrins Catalyzed Oxidations.* Kluwer Academic Publishers; 1994. 49-86.

30. Smith KM. *New J. Chem.* 2016; **40**: 5644-5649.

31. Zhang J, Jiang C, Figueiró Longo JP, Azevedo RB, Zhang H and Muehlmann LA. *Acta Pharm. Sin. B* 2018; **8**: 137-146.

32. Fischer H and Zeile K. *Justus Liebigs Ann. Chem.* 1929; **468**: 98-116.

33. Kooriyaden FR, Sujatha S, Varghese B and Arunkumar C. *J. Fluor. Chem.* 2015; **170**: 10-16.

34. Littler BJ, Ciringh Y and Lindsey JS. *J. Org. Chem.* 1999; **64**: 2864-2872.
35. Arsenault GP, Bullock E and MacDonald SF. *J. Am. Chem. Soc.* 1960; **82**: 4384-4389.
36. Lash TD. *J. Porphyrins Phthalocyanines* 2016; **20**: 855-888.
37. Johnson AW and Kay IT. *Proc. Chem. Soc. London* 1964: 73-100.
38. Gross Z, Galili N and Saltsman I. *Angew. Chem. Int. Ed.* 1999; **38**: 1427-1429.
39. Lu J, Liu HY, Shi L, Wang XL, Ying X, Zhang L, Ji LN, Zang LQ and Chang CK. *Chin. Chem. Lett.* 2011; **22**: 101-104.
40. Teo RD, Hwang JY, Termini J, Gross Z and Gray HB. *Chem. Rev.* 2017; **117**: 2711-2729.
41. Choy JH, Kwak SY, Jeong YJ and Park JS. *Angew. Chem. Int. Ed.* 2000; **39**: 4045-4047.
42. Liu HY, Mahmood MHR, Qiu SX and Chang CK. *Coord. Chem. Rev.* 2013; **257**: 1306-1333.
43. König M, Faschinger F, Reith LM and Schöfberger W. *J. Porphyrins Phthalocyanines* 2016; **20**: 96-107.
44. Palmer JH. *Struct. Bond.* 2012; **142**: 49-90.
45. Paolesse R, Licoccia S, Bandoli G, Dolmella A and Boschi T. *Inorg. Chem.* 1994; **33**: 1171-1176.
46. Guilard R, Gryko DT, Canard G, Barbe JM, Koszarna B, Brandès S and Tasior M. *Org. Lett.* 2002; **4**: 4491-4494.
47. Gryko DT and Koszarna B. *Org. Biomol. Chem.* 2003: 1:350-357.
48. Koszarna B and Gryko DT. *J. Org. Chem.* 2006; **71**: 3707-3717.
49. Král V, Vašek P and Dolenský B*ollect. Czechoslov. Chem. Commun.* 2004; **69**: 1126-1136.
50. Taniguchi M and Lindsey JS. *Chem. Rev.* 2017; **117**: 344-535.
51. Pandey RK, Isaac M, MacDonald I, Medforth CJ, Senge MO, Dougherty TJ and Smith KM. *J. Org. Chem.* 1997; **62**: 1463-1472.

52. Chang CK and Sotiriou C. *J. Org. Chem.* 1985; **50**: 4989-4991.
53. Aronoff S and Calvin M. *J. Org. Chem.* 1943; **8**: 205-223.
54. Calvin M, Ball RH and Aronoff S. *J. Am. Chem. Soc.* 1943; **65**: 2259-2259.
55. Dorough GD and Huennekens FM. *J. Am. Chem. Soc.* 1952; **74**: 3974-3976.
56. Whitlock HW, Hanauer R, Oester MY and Bower BK. *J. Am. Chem. Soc.* 1969; **91**: 7485-7489.
57. Berenbaum MC, Akande SL, Bonnett R, Kaur H, Ioannou S, White RD and Winfield UJ. *Br. J. Cancer* 1986; **54**: 717-725.
58. Aravindu K, Kim HJ, Taniguchi M, Dilbeck PL, Diers JR, Bocian DF, Holten D and Lindsey JS. *Photochem. Photobiol. Sci.* 2013; **12**: 2089-2109.
59. Cerqueira A, Moura N, Serra V, Faustino M, Tomé A, Cavaleiro J and Neves M. *Molecules* 2017; **22**: 1269.
60. McCarthy JR, Bhaumik J, Merbouh N and Weissleder R. *Org. Biomol. Chem.* 2009; **7**: 3430-3436.
61. Pereira MM, Abreu AR, Goncalves NPF, Calvete MJF, Simões AVC, Monteiro CJP, Arnaut LG, Eusébio ME and Canotilho J. *Green Chem.* 2012; **14**: 1666-1672.
62. Nascimento BFO, Rocha Gonsalves R M.d'A and Pineiro M. *Inorg. Chem. Commun.* 2010; **13**: 395-398.
63. Ferreira J, Menezes PFC, Kurachi C, Sibata C, Allison RR and Bagnato VS. *Laser Phys. Lett.* 2008; **5**: 156-161.
64. Galezowski M and Gryko D. *Curr. Org. Chem.* 2007; **11**: 1310-1338.
65. Inhoffen HH. *Pure Appl. Chem.* 1968; **17**:443-460.
66. Nolte W and Infoffen HH. *Liebigs Ann. Chem.* 1969; **725**: 167-176
67. Andersson LA, Sotiriou C, Chang CK and Loehr TM. *J. Am. Chem. Soc.* 1987; **109**: 258-264.
68. Brückner C, Rettig SJ and Dolphin D. *J. Org. Chem.* 1998; **63**: 2094-2098.
69. Furuta H, Asano T and Ogawa T. *J. Am. Chem. Soc.* 1994; **116**: 767-768.
70. Chmielewski PJ, Latos-Grażyński L, Rachlewicz K and Glowiak T. *Angew.*

Chem. Int. Ed. 1994; **33**: 779-781.

71. Geier GR, Haynes DM and Lindsey JS. *Org. Lett.* 1999; **1**: 1455-1458.
72. Lee C, Lee DH and Hong JI. *Tetrahedron Lett.* 2001; **42**: 8665-8668.
73. Sessler JL and Seidel D. *Angew. Chem. Int. Ed.* 2003; **42**: 5134-5175.
74. Maeda H, Osuka A, Ishikawa Y, Aritome I, Hisaeda Y and Furuta H. *Org. Lett.* 2003; **5**: 1293-1296.
75. Maeda H and Furuta H. *Pure Appl. Chem.* 2006; **78**: 29-44.
76. Furuta H, Maeda H and Osuka A. *J. Am. Chem. Soc.* 2000; **122**: 803-807.
77. Gouterman M. *J. Mol. Spectrosc.* 1961; **6**: 138-163.
78. Gouterman M, Wagnière GH and Snyder LC. *J. Mol. Spectrosc.* 1963; **11**: 108-127.
79. Binstead RA, Crossley MJ and Hush NS. *Inorg. Chem.* 1991; **30**: 1259-1264.
80. Wouterlood FG and Boekel AJ. *Encycl. Neurosci.* 2009: 253-260.
81. Hien NK, Nhan DT, Kim WY, Van Bay M, Nam PC, Van DU, Lim IT, Kim JS and Quang DT. *Dyes Pigments* 2018; **152**: 118-126.
82. Del Valle JC and Catalán J. *Phys. Chem. Chem. Phys.* 2019; **21**: 10061-10069.
83. Michael K. *Discuss. Faraday Soc.* 1950; **9**: 14-19.
84. Wang LL, Peng SH, Wang H, Ji LN and Liu HY. *Phys. Chem. Chem. Phys.* 2018; **20**: 20141-20148.
85. Harriman A. *J. Chem. Soc.* 1980; **77**: 1281-1291.
86. Seybold PG and Gouterman M. *J. Mol. Spectrosc.* 1969; **31**: 1-13.
87. Karolczak J, Kowalska D, Lukaszewicz A, Maciejewski A and Steer RP. *J. Phys. Chem. A* 2004; **108**: 4570-4575.
88. Brannon JH and Magde D. *J. Phys. Chem.* 1978; **82**: 705-709.
89. Magde D, Wong R and Seybold PG. *Photochem. Photobiol.* 2002; **75**: 327.
90. Gradyushko AT, Sevchenko AN, Solovyov KN and Tsvirko MP. *Photochem. Photobiol.* 1970; **11**: 387-400.
91. Strachan JP, Gentemann S, Seth J, Kalsbeck WA, Lindsey JS, Holten D and

Bocian DF. *J. Am. Chem. Soc.* 1997; **119**: 11191-11201.

92. Berezin MY and Achilefu S. *Chem. Rev.* 2010; **110**: 2641-2684.
93. Becker W. *The bh TCSPC Handbook*. 8th Ed. Becker & Hickl Gmbh, Berlin, 2019.
94. Dabrowski JM, Krzykawska M, Arnaut LG, Pereira MM, Monteiro CJP, Simões S, Urbańska K and Stochel G. *ChemMedChem* 2011; **6**: 1715-1726.
95. Zhang J, Jiang C, Figueiró Longo JP, Azevedo RB, Zhang H and Muehlmann LA. *Acta Pharm. Sin. B* 2018; **8**: 137-146.
96. Baskaran R, Lee J and Yang S-G. *Biomater. Res.* 2018; **22**: 1-8.
97. Hackbarth S, Ro B, Spiller W, Kliesch H and Worle D. *J. Porphyrins Phthalocyanines*. 1998; **2**: 145-158.
98. Shimizu O, Watanabe J, Imakubo K and Naito S. *J. Phys. Soc. Jpn* 1998; **67**: 3664-3667.
99. Barroso Á, Grüner M, Forbes T, Denz C and Strassert CA. *ACS Appl. Mater. Interfaces* 2016; **8**: 15046-15057.
100. Mang TS, Allison R, Hewson G, Snider W and Moskowitz R. *Cancer J. Sci. Am.* 1998; **4**: 378-384.
101. Antipas A, Buchler JW, Gouterman M and Smith PD. *J. Am. Chem. Soc.* 1978. **100**: 3015-3024.
102. Drzewiecka-Matuszek A, Kania A, Karocki A, Stochel G and Fiedor L. *J. Biol. Inorg. Chem.* 2005; **10**: 453-462.
103. Benov L. *Med. Princ. Pract.* 2015; **24**: 14-28.
104. Plaetzer K, Krammer B, Berlanda J, Berr F and Kiesslich T. *Lasers Med. Sci.* 2009; **24**: 259-268.
105. Foote CS. *Science* 1968; **162**: 963-970.
106. Ackroyd R, Kelty C, Brown N and Reed M. *Photochem. Photobiol.* 2001; **74**: 656.
107. Aldred E, *Pharmacology: A Handbook for Complementary Healthcare Professionals*. London: Elsevier, 2009.
108. Hrycay EG and Bandiera SM. *Adv. Pharmacol.* 2015; **74**: 35-84.

109. Reynolds T. *J. Natl. Cancer Inst.* 1997; **89**: 112-114.

110. Nelke KH, Pawlak W, Leszczyszyn J and Gerber H. *Postepy Hig. Med. Dosw.* 2014; **68**: 119-128.

111. Story W, Sultan AA, Bottini G, Vaz F, Lee G and Hopper C. *Lasers Surg. Med.* 2013; **45**: 370-376.

112. Patel H, Mick R, Finlay J, Zhu TC, Rickter E, Keith A, Malkowicz SB, Hahn SM and Busch TM. *Clin. Cancer Res.* 2008; **14**: 4869-4876.

113. Huggett MT, Jermyn M, Gillams A, Illing R, Mosse S, Novelli M, Kent E, Bown SG, Hasan T, Pogue BW and Pereira SP. *Br. J. Cancer* 2014; **110**: 1698-1704.

114. Qumseya BJ, David W and Wolfsen HC. *Clin. Endosc.* 2013; **46**: 30-37.

115. Fayter D, Corbett M, Heirs M, Fox D and Eastwood A. *Health Technol. Assess.* 2010; **14**: 3-129.

116. Kostron H, Obwegeser A and Jakober R. *J. Photochem. Photobiol. B* 1996; **36**: 157-168.

117. Tanielian C, Schweitzer C, Mechin R and Wolff C. *Free Radic. Biol. Med.* 2001; **30**: 208-212.

118. Sandell JL and Zhu TC. *J. Biophotonics* 2011; **4**: 773-787.

119. Dabrowski JM, Arnaut LG, Pereira MM, Monteiro CJP, Urbańska K, Simões S and Stochel G. *ChemMedChem* 2010; **5**: 1770-1780.

120. Kübler AC, Haase T, Staff C, Kahle B, Rheinwald M and Mühling J. *Lasers Surg. Med.* 1999; **25**: 60-68.

121. Dilkes MG, Benjamin E, Ovaisi S and Banerjee AS. *J. Laryngol. Otol.* 2003; **117**: 713-717.

122. Kochneva E V., Filonenko E V., Vakulovskaya EG, Scherbakova EG, Seliverstov O V., Markichev NA and Reshetnickov A V. *Photodiagnosis Photodyn. Ther.* 2010; **7**: 258-267.

123. Kwak SY, Lim DS, Bae SM, Kim YW, Lee JM, Namkoong SE, Han SJ, Kim JK, Lee CH, Chun HJ and Ahn WS. *J. Porphyrins Phthalocyanines* 2005; **9**: 835-840. {

124. Brilkina AA, Dubasova L V., Sergeeva EA, Pospelov AJ, Shilyagina NY, Shakhova NM and Balalaeva I V. *J. Photochem. Photobiol. B* 2019; **191**: 128-134.

125. Huang L, Zhiyentayev T, Xuan Y, Azhibek D, Kharkwal GB and Hamblin MR. *Lasers Surg. Med.* 2011; **43**: 313-323.

126. Hu X, Huang YY, Wang Y, Wang X and Hamblin MR. *Front. Microbiol.* 2018; **9**: 1-24.

127. George S, Hamblin MR and Kishen A. *Photochem. Photobiol. Sci.* 2009; **8**: 788-795.

128. Piepho SB and Schatz PN. *Group Theory in Spectroscopy with Applications to Magnetic Circular Dichroism*. New York: Wiley-VCH Verlag GmbH; 1983.

129. Frisch MJ, Trucks GW, Schlegel HB, Scuseria GE, Robb MA, Cheeseman JR, Scalmani G, Barone V, Petersson G a., Nakatsuji H, Li X, Caricato M, Marenich AV, Bloino J, Janesko BG, Gomperts R, Mennucci B, Hratchian HP, Ortiz JV, Izmaylov AF, Sonnenberg JL, Williams, Ding F, Lipparini F, Egidi F, Goings J, Peng B, Petrone A, Henderson T, Ranasinghe D, Zakrzewski VG, Gao J, Rega N, Zheng G, Liang W, Hada M, Ehara M, Toyota K, Fukuda R, Hasegawa J, Ishida M, Nakajima T, Honda Y, Kitao O, Nakai H, Vreven T, Throssell K, Montgomery Jr. JA, Peralta JE, Ogliaro F, Bearpark MJ, Heyd JJ, Brothers EN, Kudin KN, Staroverov VN, Keith TA, Kobayashi R, Normand J, Raghavachari K, Rendell a. P, Burant JC, Iyengar SS, Tomasi J, Cossi M, Millam JM, Klene M, Adamo C, Cammi R, Ochterski JW, Martin RL, Morokuma K, Farkas O, Foresman JB and Fox DJ. 2016: Gaussian 09, Revision E.01, Gaussian, Inc., Wallingford CT

130. Andrieko GA. Available from: https://www.chemcraftprog.com.

131. Hanwell MD, Curtis DE, Lonie DC, Vandermeersch T, Zurek E and Hutchison GR. *J. Cheminform.* 2012; **4**: 17.

132. Georgakoudi I, Nichols MG and Foster TH. *Photochem. Photobiol.* 1997; **65**: 135-144.

133. Ferreira J, Kurachi C, Moriyama LT, Menezes PFC, Perussi JR, Sibata C, Zucoloto S, Castro e Silva J and Bagnato VS. *Laser Phys. Lett.* 2006; **3**: 91-95.
134. Mosmann T. *J. Immunol. Methods* 1983; **65**: 55-63.
135. Sindelo A, Kobayashi N, Kimura M and Nyokong T. *J. Photochem. Photobiol. A* 2019; **374**: 58-67.
136. Datta-Gupta N, Malakar D, Jenkins C and Strange C. *Bull. Chem. Soc. Jpn* 1988; **61**: 2274-2276.
137. Cai S, Shokhireva TK, Lichtenberger DL and Walker FA. *Inorg. Chem.* 2006; **45**: 3519-3531.
138. Nascimento BFO, António M, Gonsalves AR and Pineiro M. *Synthesis (Stuttg).* 2001; **60**: 5-9.
139. Basu A, Kitamura M, Mori S, Ishida M, Xie Y and Furuta H. *J. Porphyrins Phthalocyanines* 2015; **19**: 361-371.
140. Xie Y, Morimoto T and Furuta H. *Angew. Chem. Int. Ed.* 2006; **45**: 6907-6910.
141. Kawamoto Y, Kinoshita Y and Tamiaki H. *Tetrahedron* 2020; **76**: 130948.
142. Embleton ML, Nair SP, Cookson BD and Wilson M. *J. Antimicrob. Chemother.* 2002; **50**: 857-864.
143. Josefsen LB and Boyle RW. *Met. Based. Drugs* 2008; **2008**.
144. Mack J, Asano Y, Kobayashi N and Stillman M. *J. Am. Chem. Soc.* 2005; **127**: 17697-17711.
145. Mack J, Stillman MJ and Kobayashi N. *Coord. Chem. Rev.* 2007; **251**: 429-453.
146. Zhang A, Kwan L and Stillman MJ. *Org. Biomol. Chem.* 2017; **15**: 9081-9094.
147. Liang X, Mack J, Zheng LM, Shen Z and Kobayashi N. *Inorg. Chem.* 2014; **53**: 2797-2802.
148. Doble S, Osinski AJ, Holland SM, Fisher JM, Geier GR, Belosludov R V., Ziegler CJ and Nemykin VN. *J. Phys. Chem. A* 2017; **121**: 3689-3698.
149. Sripothongnak S, Ziegler CJ, Dahlby MR and Nemykin VN. *Inorg. Chem.* 2011; **50**: 6902-6909.

150. Brookfield RL, Ellul H and Harriman A. *J. Photochem.* 1985; **31**: 97-103.

151 Rhys Williams AT, Winfield SA, Miller JN. *Analyst.* 1983; **108**: 1067-1071.

152. Berera R, van Grondelle R and Kennis JTM. *Photosynth. Res.* 2009; **101**: 105-118.

153. Keane PM and Kelly JM. *Photochem. Photobiol. Sci.* 2011; **10**: 1578-1586.

154. Ghosh A. *Chem. Rev.* 2017; **117**: 3798-3881.

155. Dryden MS. *J. Antimicrob. Chemother.* 2010; **65**: 35-44.

156. Lin J-T. *Med. Devices Diagn. Eng.* 2016; **1**: 36-41.

157. Jenkins SG and Schuetz AN. *Mayo Clin. Proc.* 2012; **87**: 290-308.

158. Balouiri M, Sadiki M and Ibnsouda SK. *J. Pharm. Anal.* 2016; **6**: 71-79.

159. Songca SP, Oluwafemi OS and Bamidele AT. *Free Radic. Biol. Med.* 2016; **100**: S194.

160. Wikene KO, Bruzell E and Tønnesen HH. *J. Photochem. Photobiol. B* 2015; **148**: 188-196.

161. Malik Z, Hanania J and Nitzan Y. *J. Photochem. Photobiol. B* 1990; **5**: 281-293.

162. Park JH, Moon YH, Bang IS, Kim YC, Kim SA, Ahn SG and Yoon JH. *Lasers Med. Sci.* 2010; **25**: 705-710.

163. Babu B, Sindelo A, Mack J and Nyokong T. *Dyes Pigments* 2021; **185**: 108886.

164. Lash LH, Hueni SE and Putt DA. *Toxicol. Appl. Pharmacol.* 2001; **177**: 1-16.

165. Vantieghem A, Xu Y, Assefa Z, Piette J, Vandenheede JR, Merlevede W, De Witte PAM and Agostinis P. *J. Biol. Chem.* 2002; **277**: 37718-37731.

166. Thomas AP, Saneesh Babu PS, Asha Nair S, Ramakrishnan S, Ramaiah D, Chandrashekar TK, Srinivasan A and Radhakrishna Pillai M. *J. Med. Chem.* 2012; **55**: 5110-5120.

167. Grebeňová D, Cajthamlová H, Holada K, Marinov J, Jirsa M and Hrkala Z. *J. Photochem. Photobiol. B* 1997; **39**: 269-278.

168. Stilts CE, Nelen MI, Hilmey DG, Davies SR, Gollnick SO, Oseroff AR, Gibson SL, Hilf R and Detty MR. *J. Med. Chem.* 2000; **43**: 2403-2410.

169. Babu B, Amuhaya E, Oluwole D, Prinsloo E, Mack J and Nyokong T. *Med.*

Chem. Commun. 2018; **10**: 41-48.

170. Babu B, Prinsloo E, Mack J and Nyokong T. *New J. Chem.* 2019; **43**:18805-18812.
171. Babu B, Mack J and Nyokong T. *Dalton Trans.* 2020; **49**:15180-15183.
172. Babu B, Mack J and Nyokong T. *Dalton Trans.* 2021; **50**: 2177-2182.
173. Spellane PJ, Gouterman M, Antipas A, Kim S and Liu YC. *Inorg. Chem.* 1980; **19**: 386-391
174. Li L, Hu J, Shi X, Ruan W, Luo J and Wei X. *Int. J. Mol. Sci.* 2016; **17**: 927.
175. Mack J and Stillman MJ. *Coord. Chem. Rev.* 2001; **219-221**: 993-1032.
176. Michl J. *J. Am. Chem. Soc.* 1978; **100**: 6812-6818.
177. Michl J. *J. Am. Chem. Soc.* 1978; **100**: 6801-6811.
178. Mack J. *Chem. Rev.* 2017; **117**: 3444-3478.